Fluid Mechanics

Experimental Investigation of Passive and Active Friction Drag Reduction

Wenfeng Li

Experimental Investigation of Passive and Active Friction Drag Reduction

Experimentelle Untersuchung aktiver und passiver Maßnahmen zur Reibungswiderstandsreduktion

Von der Fakultät für Maschinenwesen
der Rheinisch-Westfälischen Technischen Hochschule Aachen
vorgelegte Dissertation zur Erlangung des akademischen Grades
eines Doktors der Ingenieurwissenschaften
genehmigte Dissertation

vorgelegt von

Wenfeng Li

Berichter: Universitätsprofessor Dr.-Ing. Wolfgang Schröder

Universitätsprofessor Dr.-Ing. Herbert Olivier

Tag der mündlichen Prüfung: 25. Aug. 2017

Diese Dissertation ist auf den Internetseiten der Universitätsbibliothek online verfügbar

Acknowledgements

This dissertation is based on my work as a research scientist at the Institute of Aerodynamics (AIA) of the RWTH Aachen University from November 2012 until today. The study is part of the research unit FOR1779 ‘Active Drag Reduction by Transversal Surface Waves’ which has been funded by the German Research Foundation.

Firstly, my special thanks go to the head of the Institute of Aerodynamics, Univ-Prof. Dr.-ing. Wolfgang Schröder, for supporting the research and giving me the opportunity to finish this dissertation. I am especially grateful for his guidance, encouragement, and motivation throughout my research work. I also want to thank Univ-Prof. Dr.-ing. Herbert Olivier for reviewing my work. My thanks also go to Univ-Prof. Dr.-ing. Eike Stumpf, who took over the chair of my doctoral examination.

I would like to thank all my colleagues at the Institute of Aerodynamics for a variety of contributions and inspiring discussions, particularly to Dr.-ing. Dorothee Roggenkamp, Dr.-ing. Wilhelm Jessen, Dr.-ing. Michael Klaas, Alexander Rubbert, Dr. -ing. Pascal Meysonnat, Yiou Liu, Philipp Dörner, Pascal Marquardt, Antje Feldhusen-Hoffmann, Marco Braun, Dr.-ing. Andreas Henze. This work would never have been completed without the supports from all the other members of the Institute of Aerodynamics. Therefore, I would like to thank all the members of the workshop and the electronics labs and my students for their support and help. I also would like to express my appreciations to all my research partners in the research unit FOR1779 who provided the necessary equipment and materials. Furthermore, I would like to extend my very grateful thanks to my former colleagues Dr.-ing. Bernardo Nottebrock, Dr.-ing. Daniel-Christian Karhoff, Dr.-ing. Franka Schröder, Dr.-ing Timo van Overbrüggen and Dr.-ing. Kai Piehop.

I am very grateful for my friends with whom I shared the past years in Germany.

I would like to express my appreciation to the China Scholarship Council for supporting my research.

I am thoroughly grateful to my parents for their endless love and support throughout my life. To them, I dedicate this dissertation.

Aachen, September 2017

Wenfeng Li

Abstract

The objective of this thesis is to contribute to the development of passive and active flow control methods for friction drag reduction. On the one hand, the study focuses on the drag reduction effect of passive riblets, i.e., surface structures that consist of tiny grooves aligned in the streamwise direction, in fully developed turbulent boundary layers (TBLs). On the other hand, the conjunction of passive and active friction drag reduction means is investigated by imposing spanwise traveling transversal surface waves on a riblet-structured surface. Experimental investigations are conducted above a flat plate with an aluminum insert whose upper surface is either smooth or riblet-structured. The insert is equipped with an electromagnetic actuator system to generate spanwise traveling transversal surface wave motions. Particle-image velocimetry (PIV) and micro-particle-tracking velocimetry (μ-PTV) are applied to investigate the influence on the TBL flows and the friction drag by riblets and the wave motions. In order to determine the impact of flow conditions and wave parameters, measurements are conducted at different Reynolds numbers, pressure gradients, unsteady inflow conditions, and wave configurations.

The drag reduction of the semi-circular riblets is found to be 4.7% in a zero-pressure gradient TBL with riblet spacing of 24 wall units whereas it is increased to 6 - 7% in realistic conditions, i.e., adverse-pressure gradient and unsteady flows with smaller riblet spacings. The streamwise and wall-normal velocity fluctuations, as well as the Reynolds shear stress, are decreased compared with that of the smooth surface configurations in the near-wall region. This suggests that the turbulence production and the viscous dissipation are altered by riblets. The active spanwise traveling transversal surface wave with wall deformation is imposed on the riblets surface by the actuator system. The results show that the passive and the active means, i.e., the riblet surface and the transversal surface wave motion, complement each other with respect to drag reduction in the zero-pressure gradient TBL. The spanwise transversal wave motion on the riblet surface achieves a significantly larger drag reduction of 9.4% in comparison with the non-actuated riblet surface. This high drag reduction is due to the wall-normal momentum that is inserted into the flow such that the turbulent mixing region is shifted further off the wall than in the non-actuated case. Under adverse-pressure gradient conditions, the induced wall-normal momentum is not enough to influence the upper turbulence structure so that the drag reduction effect of riblets is not enhanced by the waves. It is found that a spanwise secondary flow is induced by the surface wave motion. The secondary flow shields the vortical structure from the wave trough preventing the downwash of high-monument fluid to the wall. The analysis of the low-speed streaks shows that the induced secondary flow rearranges the near-wall turbulence structures above the actuated riblet surface.

Zusammenfassung

Diese Dissertation soll dazu beitragen, die Entwicklung von passiven und aktiven Möglichkeiten der Strömungsbeeinflussung zur Reduktion der Reibungswiderstände voranzutreiben. Einerseits wird im Rahmen dieser Arbeit der Einsatz von passiven Riblets in vollausgebildeten turbulenten Grenzschichten (TGS) untersucht, d.h. Oberflächenstrukturen, die feine Rillen in Strömungsrichtung aufweisen. Andererseits wird die Kombination passiver Riblets und aktiver Methoden untersucht. Hierbei werden den Ribletoberflächen transversale, in Spannweitenrichtung wandernde Oberflächenwellen aufgezwungen. Die experimentellen Untersuchungen werden an einer Aluminiumplatte durchgeführt, deren Oberfläche entweder glatt, oder mit Riblet-Strukturen versehen ist. Die wandernden, transversalen Wellenbewegungen werden durch ein elektromagnetisches Aktuatorsystem unterhalb der Platte erzeugt. Zur Untersuchung der Einflüsse der Wellenbewegung und der Riblets auf die turbulenten Grenzschicht und den Reibungswiderstand werden PIV (particle-image velocimetry) und μ-PTV (micro-particle tracking velocimetry) durchgeführt. Um den Einfluss variierender Strömungsbedingungen und Wellenparameter auf den Reibungswiderstand zu bestimmen, werden unterschiedliche Reynoldszahlen, Druckgradienten, instationäre Anströmbedingungen und Wellenkonfigurationen untersucht.

In einer TGS ohne Druckgradienten beläuft sich die Widerstandsreduktion durch die halbrunden Riblets auf 4,7% bei einem Riblet Abstand von 24 viskosen Einheiten. Bei realistischen Bedingungen hingegen, d.h. einem positiven Druckgradienten und einer instationären Anströmung wird mit kleineren Riblet-Abständen sogar eine Widerstandsreduktion von 6 - 7% erzielt. Die Geschwindigkeitsschwankungen in Strömungsrichtung und normal zur Wand, sowie die Reynolds'schen Schubspannungen verringern sich im Vergleich zu den Konfigurationen mit glatter Oberfläche. Durch den Einsatz von Riblet-Strukturen werden die Turbulenzproduktion und die viskose Dissipation beeinflusst. Die aktive, in Spannweitenrichtung wandernde, transversale Oberflächenwelle wird durch das Aktuator-System induziert, so dass sich die Ribletoberfläche in wandnormale Richtung verformt. Die Ergebnisse zeigen, dass die aktiven und passiven Methoden, d.h. die bewegte Oberfläche und die Riblet-Strukturen, sich hinsichtlich einer Widerstandsverminderung in einer TGS ohne Druckgradienten ergänzen. Die transversale Wellenbewegung in Spann-weitenrichtung der Riblet-Oberflächen verringert den Strömungswiderstand um 9,4%. Dieser große Rückgang lässt sich auf den durch die Welle induzierten wandnormalen Impuls zurückführen, der auf die Strömung wirkt und die turbulente Mischung im Vergleich zur glatten, nicht-aktuierten Oberfläche von der Wand weg verschiebt. Im Falle eines positiven Druckgradienten ist der wandnormale Impuls zu schwach um die sich in höheren Strömungsschichten befindlichen turbulenten Strukturen zu beeinflussen, sodass der Effekt der Widerstandsreduktion von Riblet-Strukturen durch die Wellenbewegung nicht verbessert wird. Es wird gezeigt, dass durch die in Spannweitenrichtung wandernde Transversalwellen-bewegung der Oberfläche eine Sekundärströmung induziert wird. Das sekundäre Strömungsfeld schirmt die Wirbelstrukturen über dem Wellental ab, sodass verhindert wird, dass Fluid mit hoher Geschwindigkeit in Wandnähe induziert wird. Dadurch wird die Wirbelstruktur der Welle durch den Abwind des schnellen Fluids in wandnahe Regionen geschützt. Die Analyse der Low-Speed Streaks zeigt, dass die induzierte Sekundärströmung zu einer Neuandordnung der wandnahen turbulenten Strukturen über der aktuierten Ribletoberfläche führt. Die wandnahen turbulenten Strukturen, die gegenläufige Wirbel mit kleineren Abständen enthalten, werden von der Wand über den Wellenberg geschoben.

Table of Contents

Nomenclature

Abbreviations

APG	adverse-pressure gradient
CCD	charged-coupled device
CMOS	complementary metal-oxide-semiconductor
DBD	dielectric-barrier-discharge
DEHS	di-ethyl-hexyl-sebacate
DNS	direct numerical simulation
DR	drag reduction ratio
FOV	field of view
IBF	Institut für Bildsame Formgebung (Institute of Metal Forming)
LES	large eddy simulation
μ-PTV	micro-particle-tracking velocimetry
PDF	probability density function
PIV	particle-image velocimetry
PTV	particle-tracking velocimetry
QSV	quasi-streamwise vortex
RMS	root-mean-square
SE	standard error
TBL	turbulent boundary layer

ZEL	Zentralinstitut für Elektronik (Central Institute for Electronics)
ZPG	zero-pressure gradient

Greek Symbols

α	degree
β	degree
β	Clauser parameter
δ	boundary layer thickness
δ^*	displacement thickness
ρ	density
λ	wavelength
η	dynamic viscosity
v	kinematic viscosity
σ	standard deviation
τ	shear stress
θ	momentum thickness
ω	vorticity

Latin Symbols

A	amplitude
c_f	friction coefficient
c_p	pressure gradient
d	diameter
f	frequency
l	length
N	number of samples
p	pressure
P	probability

Q	quadrant
R_{ij}	correlation function between signals i and j
R	radius
Re	Reynolds number
Re_x	Reynolds number based on U_∞ and the streamwise position x
Re_θ	Reynolds number based on U_∞ and the momentum thickness θ
Re_τ	Reynolds number based on u_τ and the boundary layer thickness δ
s	spacing
T	period
t	time
u_τ	friction velocity
u	streamwise velocity component
v	wall-normal velocity component
w	spanwise velocity component
x	cartesian coordinate in the streamwise direction
y	cartesian coordinate in the wall-normal direction
z	cartesian coordinate in the spanwise direction

Subscripts

∞	freestream condition
ref	reference
w	wall condition
A.	actuated
N. A.	non-actuated
peak	maximum value
rms	root-mean-square
local	variables at local position

Superscripts

x'	fluctuation component of the fluid characteristics
x^+	scaled by u_τ and ν, in inner wall units
$\bar{x}$	temporal mean of variable

1 Introduction

More than 50% of the total drag on modern long-haul large commercial airplanes is due to the friction[1]. Reducing the friction drag due to the turbulent flow leads to a significant improvement of the aerodynamic performance of an aircraft. The benefits can be translated into a reduction of operating costs. More importantly, due to the strong link between drag and energy consumption, it goes without saying that there is a strong need to lower the overall drag of the next generation transportation systems to fulfill the environmental constraints. In other words, means to reduce friction drag by controlling the turbulent boundary layer (TBL), have to be developed. This idea is not new; it is as old as the scientific investigation of TBL flows. However, in recent years reducing energy consumption has become more and more urgent as awareness of environmental issues has increased greatly. Therefore, ideas on how to lower friction drag are extremely important.

Reducing the turbulent skin-fiction is a challenging theoretical and technological problem that has drawn much attention in the fluid mechanics research community. In the past decades, numerous flow control strategies have been developed to reduce friction drag, e.g., microstructured surfaces, hydrophobic materials, MEMS-based closed-loop feedback controls, and open-loop large-scale wall motions. Based on the energy expenditure and the control loop, a tentative scheme is proposed by Gad-El-Hak [2] for the classification of flow control methods. As shown in figure 1.1, the control methods can be divided into the passive ones which need no auxiliary power, and the active ones that require an energy input and control loop. The active controls are further divided into predetermined and reactive categories depending on the requirements of the control loop.

Riblets are one of the passive drag reduction devices which have been successfully applied to reduce friction of wall-bounded flows not only in laboratories but also in industrial applications attaining a drag reduction of up to 10% [3]. A riblet surface consists of microgrooves of the size of the viscous sublayer with either triangular or semicircular cross sections. Walsh et al. [4-6] are among the first researchers who experimentally tested riblets with different geometries including triangular, notched-peak, U-shaped, and sinusoidal shapes in wall-bounded flows. They observed that the drag reduction effect depended not only on the geometry but also on the riblet spacing. A maximum drag reduction of 7 - 8% was achieved with a riblet spacing in inner coordinates of approximately $s^+ = s\, u_\tau / \nu = 15$, where s was the riblet spacing, u_τ was the friction velocity and ν was the kinematic viscosity. In addition, an enlargement of the riblet spacing up to $s^+ > 30$ was observed to result in drag increase.

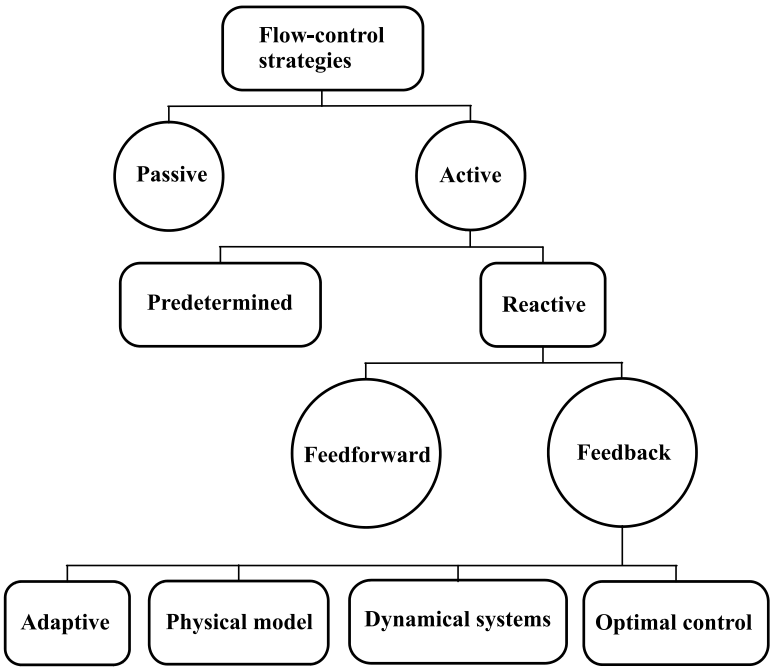

Figure 1.1: Classification of flow control strategies [2].

The passive flow control by riblets does not need energy input. However, the passive devices usually have a fixed geometry and thus are only effective in a limited parameter range. Beyond their working range, they can also exhibit the opposite of the desired effect by increasing the friction above flat surface levels. Additionally, the durability of the micro-structured riblet seems to be another barrier to their successful application in the airline industry. Riblets are usually formed on thin films that are affected by pollutions such as the leaking of fuels, the interference by paint, and dusts in the environment, and in the worst case, the riblets can be peeled off the surface. This requires extra cost and labor for the reinstallation and maintenance over the lifetime of an airplane [7]. So far, no significant success of riblets has been achieved by major airline companies. Recently, Hirt and Thome [8] showed that the riblets with a better wearing resistance can be formed on metallic sheets by a rolling process. Instead of installing riblet films on airplanes, the riblet-structured metallic sheets are used as the skin of aircrafts directly. This gives the possibility to build permanent riblet structures on airplanes. Thus, it is necessary to investigate the drag reduction capacity of the rolled riblet sheets.

Besides passive control methods, there are the active control concepts based on changing the near-wall turbulence by manipulating the near-wall flow. The adaptive active control methods have become increasingly important in the recent twenty years. Numerical simulations [3, 9-13] have shown that in internal and external flows drag reduction of up to 45% can be achieved with surface motion and forcing.

In active flow controls, various mechanisms, e.g., wall oscillation, body force actuation, and surface wave motions via wall deformation are applied for flow manipulation. Among them, spanwise wall oscillation is one of the most widely investigated methods since Jung *et al.* [13] firstly reported that turbulent friction drag can be reduced by high-frequency spanwise surface oscillation. By using direct numerical simulation (DNS), they investigated channel

flows undergoing surface oscillations with periods that ranged from 25 to 500 in dimensionless time units and the drag reduction ratio (DR) was found to range between 10% and 40%. Another example is the spanwise traveling forcing induced by electromagnetic tiles. It has been simulated by Du *et al.* [9, 14] via DNS in channel flows. They reported that the spanwise forcing led to an enhancement of the streamwise vortices that resulted in a damping effect of the streak intensity. The drag reduction ranged up to 30% at Re_τ = 150 and then higher drag reduction could be achieved with better overall energetic performance. Since there are vast amounts of literature on active flow control for friction drag reduction, only a few examples are listed above for the readers to gain a brief overview on the characteristics of the active friction control methods. In the next chapter, a detailed literature review will be shown in section 2.3.

The flow control concepts for drag reduction listed in the schematic in figure 1.1 have been investigated intensively. Most of the researchers, however, only focus on one flow control concept, either the passive or the active control. Considering the similarity in the mechanism leading to drag reduction for riblets and moving surfaces, i.e., the influence of the passive or active means on the near-wall velocity distribution and on the sweep and ejection events, it is more or less natural to link both concepts, i.e., to investigate the impact of riblet surfaces undergoing a spanwise transversal motion on the wall-shear stress distribution. This combination of the passive and the active controls is possible since it has been shown by Roggenkamp *et al.* [15] that an aluminum smooth surface can be excited by a transversal wave motion. It makes sense to perform such an analysis since the reduction effect of the wall-shear stress observed for the moving surface could be enhanced by the riblets and the susceptibility on the riblet geometry could be lowered by the wall movement.

In this work, passive and active, i.e., spanwise traveling transversal wave motion, drag reduction concepts are linked to investigate the impact of riblet surfaces undergoing a spanwise traveling transversal wave on the wall-shear stress distribution. First, the fundamentals of TBLs are summarized and the passive and active flow control methods are discussed to review the current state of the art and their working principles in chapter 2. Subsequently, chapter 3 describes the experimental facilities and setups, the particle-image velocimetry (PIV), micro-particle-tracking velocimetry (µ-PTV), and the uncertainty analysis of both measurement methods. The PIV and µ-PTV measurements are validated in chapter 4 by a near-wall hot-wire in a TBL flow and a systemic error correction for the µ-PTV results is proposed. In chapter 5, the drag reduction effect of the rolled riblet sheet in TBLs is investigated under various flow conditions, i.e., zero-pressure gradient (ZPG), adverse-pressure gradient (APG), and periodical unsteady inflow. In chapter 6, the riblet surface is excited by a spanwise traveling transversal wave motion. The combination of the passive and active flow controls is investigated regarding the influence on the drag reduction effect, the turbulence statistics, and the near-wall flow structure. Finally, the essential findings and conclusions are summarized in chapter 7.

2 Fundamentals and background

In this chapter, the fundamentals of turbulent wall-bounded flows and the passive and active control concepts are discussed. Section 2.1 focuses on fully developed TBL flows and the underlying flow phenomena. The main features of the flow that generate and sustain the near-wall turbulence are characterized. In section 2.2, the microgrooves aligned in the freestream direction, i.e., the riblets, are discussed. An introduction into the passive riblets reviews the drag reduction mechanisms and the technical applications. Section 2.3 summarizes the active flow control methods that manipulate the near-wall turbulence to reduce the friction drag.

2.1 Turbulent boundary layer

Most flows in nature or human activities, from the atmosphere and ocean circulations, the water in rivers, to the oil in pipes, the air around airplanes and cars, are turbulent. The term 'turbulent' denotes a flow motion in which an irregular fluctuation (mixing or eddying motion) is superimposed on the main flow [16]. This irregular fluctuation plays an important role in the wall-bounded flows as it causes a great drag of turbulent flow in pipes, turbulent friction drag on airplanes and cars, and losses in wind turbines and turbomachines. This thesis focuses on one of the simplest wall-bounded flows, the TBL on a flat plate, to investigate the friction drag reduction by means of passive and active flow control.

Once flow passes over an object, a boundary layer develops on its surface. The viscosity of the fluid ensures a smooth transition from the freestream velocity U_∞ in the main flow to zero at the bottom of the boundary layer to fulfill the no-slip condition. For a Newtonian fluid, equation 2.1 describes the relation between the wall-shear stress τ_w and the velocity distribution:

$$\tau_w = \eta \cdot \frac{\partial u}{\partial y}|_{y=0} \tag{2.1}$$

where η is the dynamic viscosity and y represents wall-normal distance.

In turbulent flows, the fluctuating motion is of fundamental importance since it causes additional shear stress. In other words, the fluctuating motion acts on the mean motion such that the viscosity appears to be increased. The fluctuating flow can be decomposed into the mean motion and a fluctuation motion, which is known as the Reynolds decomposition. If the time average of the velocity component u_i is denoted as $\bar{u}_i$, and the fluctuation velocity as u'_i, then the velocity components can be witten as:

$$u_i = \bar{u}_i + u'_i. \tag{2.2}$$

Accordingly, the root-mean-square (rms) is defined as

$$u'_{i,rms} = \sqrt{\frac{1}{n}\sum_{j=1}^{n}(u_i - \bar{u}_i)^2}\ . \tag{2.3}$$

In quasi-two-dimensional TBLs, the Reynolds decomposition is applied by a temporal averaging of the Navier-Stokes Equations. The additional shear stress caused by the fluctuating velocity is known as Reynolds shear stress and it can be expressed in the term of

$$\tau_{xy} = -\rho\overline{u'v'}. \tag{2.4}$$

The two-point correlation of a turbulent flow is a measure of the interaction and similarity of flow characteristics at two different points. The two-point correlation function for the fluctuating velocity at x_1 and x_2 are defined as:

$$R_{u_iu_j} = \frac{\overline{u'_i(x_1,t)u'_j(x_2,t)}}{\sqrt{u'^2_i(x_1,t)}\sqrt{u'^2_j(x_2,t)}}. \tag{2.5}$$

The index *i* and *j* indicate the directions of the velocity components.

The thickness of a boundary layer δ is a statistic means that defines the edge of the turbulent flow within the boundary layer. It refers to the distance from the wall where the mean velocity reaches 99% of the freestream velocity U_∞. Since δ is an arbitrary measure, it is usually poorly determined by experimental and numerical means. Thus, two well-defined measures in the integral form are used to describe the boundary layer thickness.

The thickness δ^* is a measure of the displacement action which reads,

$$\delta^* = \int_0^\infty (1 - \frac{u}{U_\infty})\, dy. \tag{2.6}$$

Moreover, the momentum thickness θ is defined by

$$\theta = \int_0^\infty \frac{U}{U_\infty}(1 - \frac{U}{U_\infty})\, dy. \tag{2.7}$$

The ratio of the former to the latter known as the shape factor, $H_{12} = \delta^*/\theta$, is introduced as an indicator for the shape of the velocity profile.

The Reynolds number $Re = \rho uL/\eta$ is the ratio of inertial forces to viscous forces with in a fluid, where ρ is the density, u is the velocity of the fluid, and L is the characteristic length. In TBLs, the Reynold number base on the momentum thickness $Re_\theta = \rho U\theta/\eta$ is often used to describe the scaling and dynamic similarity.

2.1.1 Law of the wall

In inner scales of the streamwise velocity profile, the wall-normal distance is defined as

$$y^+ = \frac{yu_\tau}{v}. \tag{2.8}$$

The mean streamwise velocity scaled by the friction velocity u_τ, reads $u^+ = u/u_\tau$, where

$$u_\tau = \sqrt{\frac{\tau_w}{\rho}}, \tag{2.9}$$

and v denotes the kinematic viscosity. It is applied to the near-wall region of TBLs so that the relation is independent of the boundary layer thickness and the freestream velocity.

The analytical analysis [16] shows that the streamwise velocity in TBLs follows a common distribution which is the so called the law of the wall. According to Pope [17], the streamwise velocity distribution can be subdivided into four parts, namely the viscous sublayer, the buffer layer, the logarithmic region, and the wake layer. In figure 2.1, the mean streamwise velocity is illustrated in inner scales to show the subdivision of the TBL.

The region between y^+ = 0 - 5 is called viscous sublayer. In this layer, the Reynolds shear-stress is negligible and the viscous force is predominant. The velocity profile is linear such that

$$u^+ = y^+ \tag{2.10}$$

is given, for instance, by Schlichting and Gersten [16] and Pope [17].

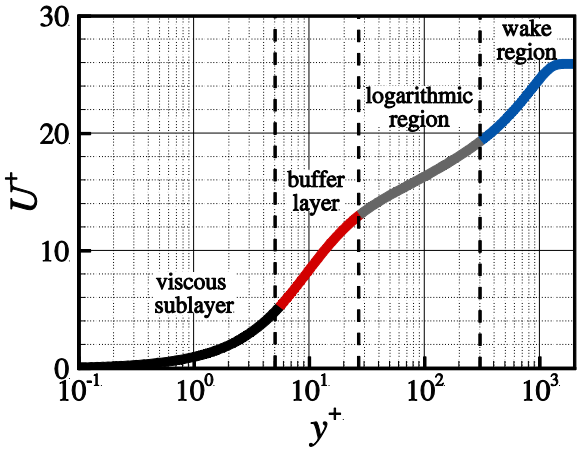

Figure 2.1: Mean velocity profile in fully developed turbulent boundary layer flow.

In the region between $y^+ > 30$ and $y / \delta < 0.1$, the velocity distribution follows a logarithmic distribution. It is a self-similar solution for the mean velocity parallel to the wall which is valid for flows at high Reynolds numbers with approximately constant shear stress and far enough from the wall for viscous effects to be negligible. There, the velocity profile follows

$$u^+ = \frac{1}{\kappa} ln y^+ + B, \tag{2.11}$$

which is called “log-law”. Classical boundary layer theory considers the parameters κ and B to be independent of Reynolds number in internal pipe and channel flows and external ZPG TBLs. Generally, they are regarded as κ = 0.41 and B = 5.0 with some minute variations depending on the publication.

2.1.2 Near-wall structures

Since the 1960s, a great fraction of the effort on wall-bounded flows has been directed at turbulent structures or coherent structures. On the one hand, many measurement techniques, e.g., flow visualization [18] [19] and particle-image velocimetry [20], and post-processing methods, e.g., conditional sampling [21] and other schooling methods have been used to identify the coherent structures and to investigate the underlying flow behaviors. On the other hand, since the 1980s, the direct numerical simulation (DNS) and the large-eddy simulation (LES) of the turbulent channel and boundary layer flows [22] [23] provided full spatial field properties and access to 3D flow structures. Those studies have yielded valuable results and gained new insights into the behavior of the near-wall turbulent flows.

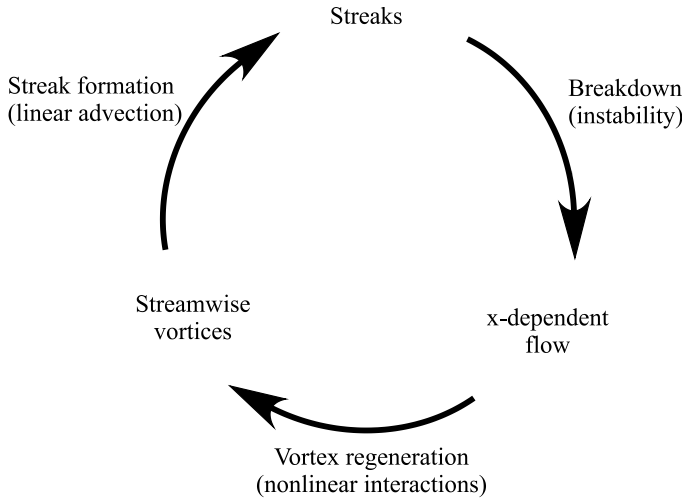

Figure 2.2: Regeneration cycle of the near-wall turbulence [24].

According to Robinson [25], the most common coherent structures in wall-bounded flows are classified as low or high-speed streaks in the near-wall region, ejection and sweeps events, vortical structures of various forms including horseshoe or hairpin vortices, and large-scale structures in the outer region. The common view on the coherent structures has been that the interaction of these flow phenomena plays an important role in the self-sustaining of turbulence. To be more precise, it is the interaction of the low- or high-speed streaks and the quasi-streamwise vortices (QSVs) that sustain the turbulence regeneration cycle in wall-bounded flows [20, 24, 26]. Figure 2.2 shows the regeneration cycle of the near-wall turbulence. It can be seen that the turbulence regeneration cycle consists of three sub-processes, namely, streak formation, streak breakdown and vortex regeneration. According to Hamilton *et al.* [24], the low- or high-speed streaks are formed by the simple advection of momentum of streamwise vortices. They start to breakdown due to their instability and lead to the vortex regeneration. Then, the vortices result in the formation of a new set of streaks and complete the turbulence regeneration cycle.

As shown in the DNS simulation by Schoppa and Hussain [27] (figure 2.3), the distribution of the streamwise velocity in the near-wall region is organized into alternating narrow streaks of low- and high-speed fluid that are persistent and relatively quiescent most of the time. The length of these streaks can exceed 1,000 wall units whereas the spacing between them is randomly distributed between about 80 to 120 wall units. These streaks have a characteristic

behavior that is known as bursting event. It can be further classified as ejection and sweep event by the interaction process of the low- or high-speed fluids. During the ejection event, the low-speed streak turns and moves away from the wall violently at some point due to instability. The streak exhibits a rapid oscillation followed by a breakdown into finer-scale motions after it is lifted. Since the near-wall fluid moves away from the wall during the ejection event, it requires a flow towards the wall in some other regions. Thus, the upper high-speed fluid moves downwards the wall. This downwards motion is called sweep event. The ejection event leads to a sweep event and the latter leads to another ejection event. This cycle is repeated to form the complete bursting cycle.

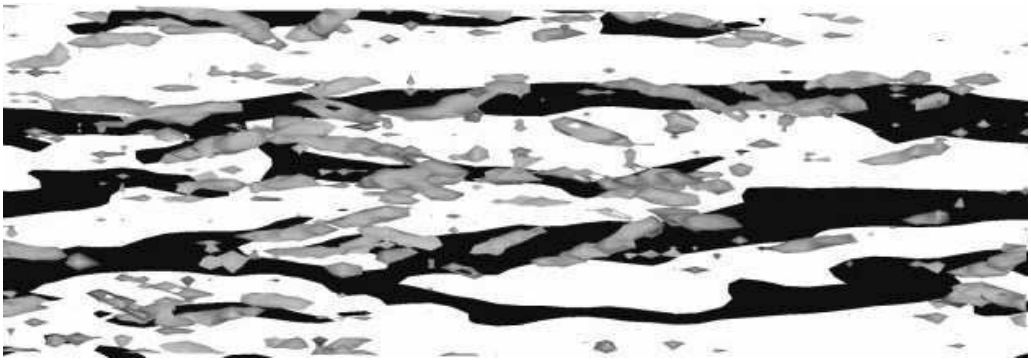

Figure 2.3: Top view of the near-wall flow structures in the streamwise and spanwise directions. Lifted low-speed streaks and streamwise vortices are indicated by the λ_2 vortex definition taken from Schoppa and Hussain [27].

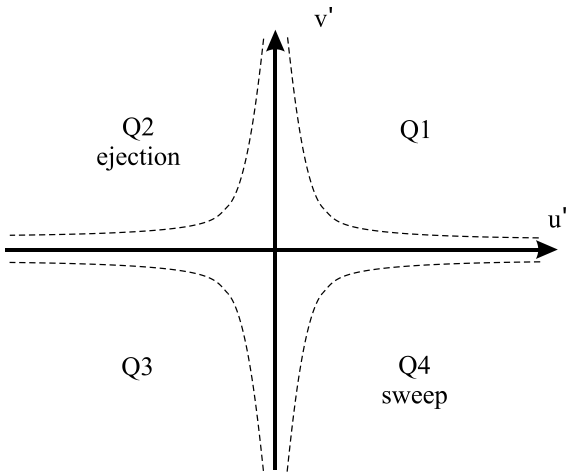

Figure 2.4: Quadrants of the instantaneous *u'*-*v'* plot.

To classify the ejection and sweep events, four quadrants (Q*i*, $i = 1, 2, 3, 4$) are defined in the Cartesian coordinate system of the *u'*-*v'* plot (i.e., $u' > 0$ and $v' > 0$, $u' < 0$ and $v' > 0$, $u' < 0$ and $v' < 0$, $u' > 0$ and $v' < 0$) according to Wallace [21] as shown in figure 2.4. The ejection and sweep events are represented by Q2 and Q4 events, respectively. The Q1 and Q3 motions are called outward and inward interactions.

In the buffer layer and the lower logarithmic region ($y^+ < 100$), the QSVs dominate the coherent structures. The QSVs are elongated vortical structures aligned in the streamwise direction. They start at the upper edge of the buffer layer and protrude into the logarithmic

region. Near the wall, the QSVs strongly influence the turbulence production and the friction drag generation by inducing both ejection and sweep events at their sides. On the one side of the QSVs, the low-speed streaks are pulled up from the wall towards the main flow whereas on the other side the high-speed streaks are pushed down to the wall. The vortical structures further out in the outer region of the TBL are hairpin-like vortices. Adrian *et al.* [20] showed that the hairpin vortices occur in streamwise-aligned packets and grow upwards in the streamwise direction. In figure 2.5, a hairpin vortex attached to the wall is depicted schematically. The various parts of the hairpin are called the head, neck, and legs. The legs and the neck of the hairpin vortex are located in the buffer layer and the head reaches into the outer region. Adrian *et al.* [20] suggested the projection of the velocity pattern of the hairpin vortices in the *x-y* plane contains a spanwise vortex core of the head and a region of low-momentum fluid located below and upstream the head (see figure 2.5 (b)).

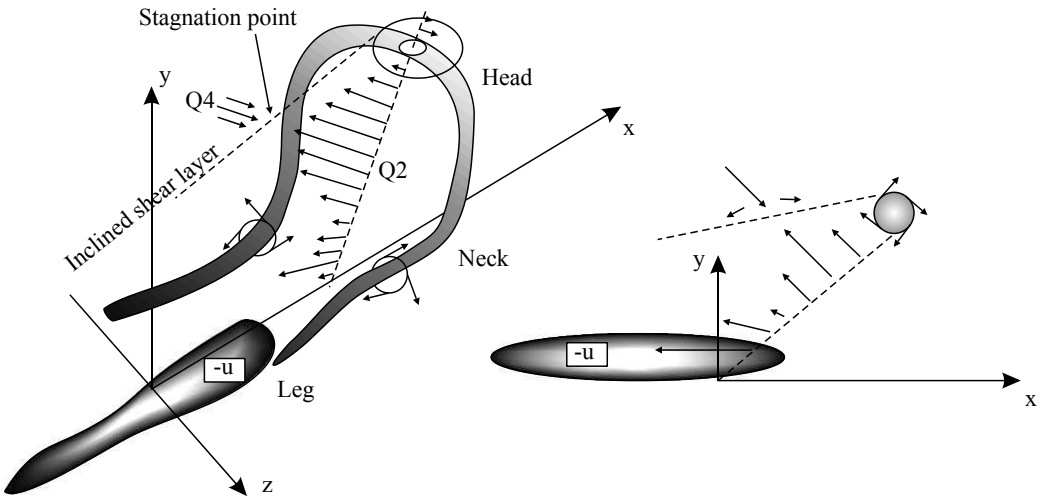

Figure 2.5: Schematic of a hairpin vortex attached to the wall, taken from Adrian *et al.* [20].

More recently, two large coherent structures, namely large-scale motions (LSMs) and very-large-scale motions (VLSMs), have been found by numerical simulations and experimental studies [28-31] in high Reynolds number flows. The review paper by Smits *et al.* [32] has described the characteristics of these two organized motions. The LSMs are believed to be associated with packets of hairpin vortices and extend 2-3 time of the boundary layer thickness in the streamwise direction. Adrian *et al.* [20] and Zhou *et al.* [26] showed that the hairpin vortices induce regions of low momentum between their legs. The VLSM extends about 10δ in streamwise direction and its streamwise momentum and Reynolds shear stress increase with increasing Reynolds numbers. They are observed in the outer layer, i.e., the logarithmic and wake regions, of wall-bounded flows. In TBL, the VLSM is often referred as superstructure. Balakumar and Adrian [28] showed through spectral analysis that the LSMs and VLSMs make a significant contribution to the kinetic energy and turbulence productions. They noticed that 40% to 65% of the kinetic energy and 30% to 50% of the Reynolds shear stress are related to the large-scale modes with streamwise wavelength larger than 3δs. Although the origin of these large-scale motions is not clear, numerous investigations suggest

that these motions in the logarithmic and outer layer may have a strong influence on the behavior of the near-wall turbulence [32].

Based on the regeneration process of the self-sustained near-wall turbulence, a number of wall-based flow control schemes have been developed and studied. These control schemes include passive means using riblets [5, 33-37] and active methods using wall motions [9, 12, 14, 38-43] to reduce the friction drag in wall-bounded turbulent flows.

2.2 Passive flow control

Riblets are tiny surface protrusions aligned in the direction of flow with different shapes. They have been recognized as one of the few passive flow control techniques that can reduce friction drag in turbulent wall-bounded flows. Figure 2.6 shows a highly magnified picture of the cross section of a triangular micro-scale riblet surface demonstrating the tiny surface protrusions. Numerous studies [5, 6, 34-36, 44-50] have reported that riblets reduce friction drag by up to 10% in both internal and external flows.

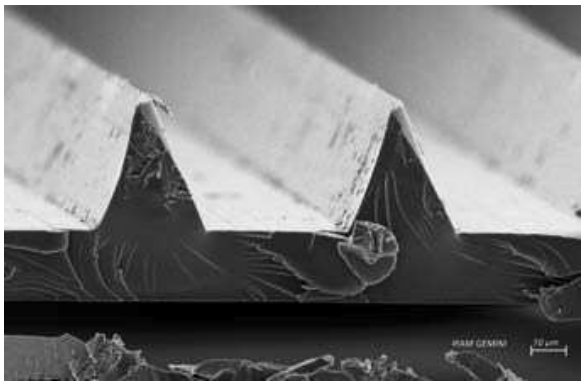

Figure 2.6: Cross section of the micro-scale riblet surface [51].

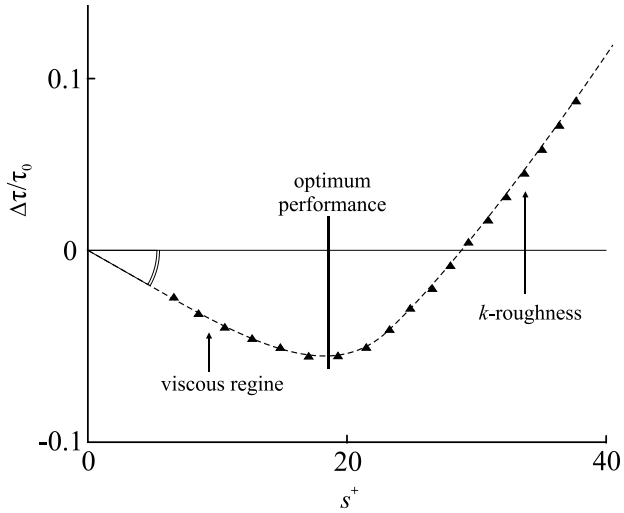

Figure 2.7: Drag reduction curve of triangular riblets with 60° tip angle as a function of the riblet spacing [36].

The concept of riblets is usually attributed to Walsh and Weinstein [52] at the NASA Langley Research Center. They investigated riblets with different geometries and were able to show

that the riblet surfaces reduce the friction drag in TBL flows under certain conditions. The maximum drag reduction of 8% was obtained at the dimensionless riblet spacing of s^+ =15. Choi [35] conducted hot-wire/-film measurements and flow visualization over a riblet surface in a wind tunnel. He showed that the turbulence intensity was reduced by up to 10%, which meant the near-wall turbulence became less violent in the buffer layer due to the riblet surface. Bechert *et al.* [34] measured the friction drag on riblet surfaces in an oil channel with a shear-stress balance and obtained a maximum drag reduction of 9.9% with the 'blade-shaped' riblets and approximately 7% on the parabolic riblets with s^+ = 15. In figure 2.7, the drag reduction curve as a function of the riblet spacing is plotted to show the different drag regimes that are defined according to s^+. In the regime of $s^+ < 10$ - 15, the drag reduction is proportional to s^+. By increasing s^+ the viscous regime breaks down near the optimum spacing for DR and the drag reduction is increased at even larger spacings [36].

Bechert and Bartenwerfer [53] proposed the concept of protrusion height to quantify the relation between the riblets geometry and the amount of friction reduction. As shown in figure 2.8, the protrusion height is defined as the vertical distance between the riblet tips and the theoretical flow origin. In addition, the protrusion height can be calculated for the longitudinal (h_{pl}) and cross (h_{pc}) directions. Bechert *et al.* [34] showed that the protrusion height difference, i.e., the difference between both protrusion heights $\Delta h = h_{pl} - h_{pc}$, plays an important role on the hampering effect on the crossflow. In the viscous regime (see figure 2.7), the protrusion height difference Δh is a constant fraction of the riblet spacing s for a given geometry and increases with an increased riblet spacing. Since the damping effect on the crossflow is enhanced by increasing Δh, the turbulent cross-flow is decreased resulting in the reduction of momentum exchange and friction drag reduction. Based on this, the slope of the drag reduction curve is represented by

$$\mathrm{DR} \propto \frac{\Delta h}{s} s^+. \tag{2.12}$$

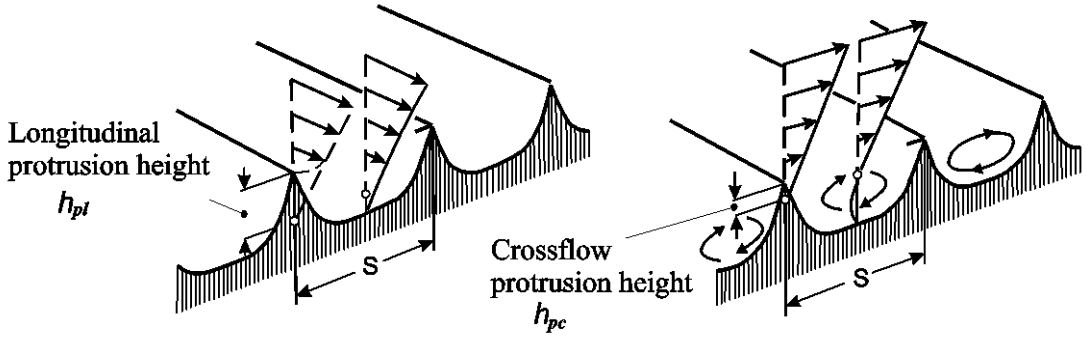

Figure 2.8: Viscous longitudinal and crossflow on a riblet surface. Adapted from Bechert *et al.* [34].

The riblets reduce the friction drag by impeding the spanwise flow motion induced by the streamwise vortices in the near-wall region [46]. This damping effect on the cross flow by riblets has been intensively investigated numerically, e.g., by Choi *et al.* [54] and Goldstein *et al.* [55], and experimentally, e.g., by Suzuki and Kasagi [56], Lee and Choi [49], and Greidanus *et al.* [57]. However, the mechanism of the interaction of the near-wall turbulence

and the riblets is complex and it is not fully understood, yet. One of the general mechanisms is that riblets reduce the friction by preventing the quasi-streamwise vortices from direct interaction with the wall. When the riblet tip spacing s is smaller than the typical diameter of the streamwise aligned vortices, the vortices cannot enter the riblet valleys and can only interact with the protruding riblet tips. Since these vortices lead to a high momentum transfer in the wall-normal direction the momentum transfer and, thus, the shear stress inside the riblet valleys is reduced. This effect was observed by Lee and Lee [58] with flow visualization as shown in figure 2.9. Direct numerical simulations by Choi *et al.* [54] showed that riblets reduce friction drag by restricting the location of the streamwise vortices above the wetted surface such that only a limited area of the riblets is exposed to the downwash of high-speed fluid induced by the vortices. Goldstein and Tuan [59] investigated the mechanism of the drag reduction effect by riblets with DNS and confirmed the drag reduction in experimental investigations. They identified cross-flow damping as one mechanism of the drag reduction. Recently, the fluid structure interaction between the turbulent flow and riblets and its impact on the drag reduction were reviewed by Dean and Bhushan [46] and García-Mayoral and Jiménez [36].

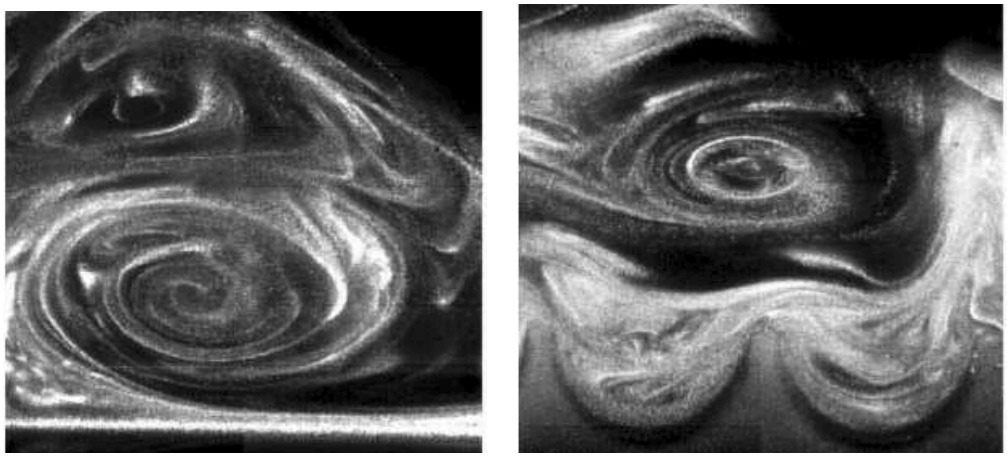

(a) (b)

Figure 2.9: Flow visualization of streamwise vortices on smooth (a) and a drag reducing riblet surfaces (b). Taken from Lee and Lee [58].

Besides the laboratory experiments and numerical simulations, riblets have been used for industrial applications even though some aspects of the physical mechanism remain controversial. One of the earliest examples of transferring the riblet concept to technical applications to reduce the friction drag and increase the efficiency was in the 1980s. Riblets were first successfully used by the United States in the 1984 Summer Olympics. The US rowing team won a silver medal for the first time in a new boat with a riblet skin. A similar structured-skin was used in 1987 on the Stars and Stripes racing yacht. Both cases succeeded, although it is hard to determine whether the major contributor to the results is the riblet.

Many attempts to use riblets on compressor blades have been made. For instance, Fang *et al.* [60] investigated riblets on an isolated 2-d blade and an NACA 65 cascade. They found up to 12% reduction of the total pressure loss. Boese and Fottner [61] investigated a blade cascade with riblets manufactured by a milling process of a sheet of brass and found a maximum

reduction of total pressure loss of 5%.

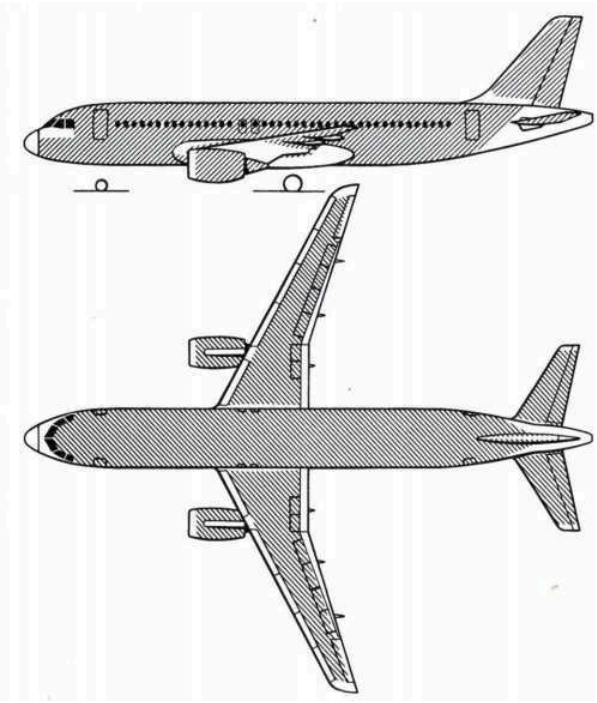

Figure 2.10: The distribution of the riblet surface on an Airbus 320 airplane [62].

Meanwhile, optimized riblets with a size of 30 - 70 μm have been applied to reduce the overall drag of airfoils [63, 64] as well as aircraft [44]. In 1989, an Airbus 320 which was covered by riblets was estimated to save about 2% of the fuel during the 1.5 years test period [62]. The distribution of riblets on the Airbus 320 airplane in figure 2.10 shows that they covered over 70 % of the surface of the aircraft. An Airbus 340 of the Cathay Pacific Airways covered with saw-tooth riblet films with riblet spacing of s = 60 μm came into service in 1996 [44]. During the 2.5 years regular service, the riblets reduced the fuel consumption by about 3% and increased the profit of the airplane by 6%. However, the test was canceled since the plastic riblet films could not stand the loads during service for a long time and this demanded extensive maintenance efforts.

Despite the aforementioned tests that have achieved some success, riblets have not appeared in service among the airline companies, yet. Spalart and Mclean [7] concluded that *riblets have no success stories in the airliner industry*. It is mainly because the durability of the riblets causes serious problems in the long-run service. Riblet films are affected by the leaks of the pressurized air and the pollution of paint and dusts in the environment. These lead to significant cost and labor to reinstall and maintain riblets over the whole life cycle of airplanes. Thus, to bring the riblets to use, new materials and methods have to be developed.

2.3 Active flow control

For high Reynolds number flows, e.g., air flows around airplanes and high-speed trains, the direct local feedback active control is not feasible since the length and time scales of the flows require complex sensing and actuation systems. Therefore, an indirect global flow control based on the manipulation of the near-wall turbulent flow is more appropriate. The

indirect global flow control approaches to reduce turbulent friction drag can be easily realized by large-scale, sensor-less, active open-loop control methods, e.g., body force oscillations, rotating disc arrays, and wall motions. A literature review of the friction drag reduction by manipulating the near-wall turbulent flow via active flow control approaches is given in the following. The discussion will focus on simple turbulent wall-bounded flows, both internal flows (pipe and channel flows) and external boundary layer flows. The flow control methods are considered regarding the excitation forces, e.g., spanwise wall oscillation, body force actuation, surface wave motions via wall deformation, etc. Furthermore, the forcing methods are categorized by directions, i.e., spanwise, streamwise, and wall-normal direction.

The spanwise wall oscillation has been intensively investigated since Jung *et al.* [13] firstly reported that friction drag can be reduced by high-frequency spanwise surface oscillation. By using DNS, Jung *et al.* [13] investigated channel flows undergoing surface oscillations with periods ranging from 25 to 500 dimensionless time units. They found the high-frequency spanwise surface oscillation resulted in drag reduction of 10% to 40%. After that, the spanwise wall oscillation was investigated experimentally by, e.g., Laadhari *et al.* [65], Choi [66], Di Cicca *et al.* [67], Gouder *et al.* [68], Gatti *et al.* [69], and numerically by Akhavan *et al.* [38], Baron and Quadrio [70], Quadrio and Ricco [11] and Touber and Leschziner [71]. Among these investigations, the maximum drag reduction of 45% can be achieved with an oscillation period of $T^+ \approx 100$. The mechanism of the drag reduction of the spanwise wall oscillation is linked to the distortion of the near-wall low- and high-speed streaks and the reduction of the turbulence contribution to the wall-shear stress.

Du *et al*. [9, 14] investigated the spanwise traveling forcing induced by electromagnetic tiles with DNS in channel flows. They found that the spanwise forcing resulted in an enhancement of the streamwise vortices that led to a damping effect of the streak intensity. The drag reduction was around 30% at $Re_\tau = 150$ and a higher drag reduction could be achieved with good overall energetic performance. Huang *et al.* [72] conducted DNS of transversal traveling wave motions via Lorentz force in an electrically conducting channel flow. Their results indicated that the friction drag was reduced through weakening and stabilizing low-speed streaks as well as longitudinal vortices. With variable-interval space averaging (VISA) detective techniques, they observed that the intensity and frequency of burst events were weakened in the drag reduction flow. Regarding airflows, particularly in experiments, the application of body forces is difficult since suitable means to generate such a force are not available. Choi *et al.* [40, 73] proposed an array of dielectric-barrier-discharge (DBD) plasma actuators to generate spanwise traveling waves in a TBL. With the advantage that no moving component is needed, the DBD plasma actuator can achieve high actuation frequencies with sufficient excitation strength. The result by Choi et al. [40, 73] showed that the plasma spanwise traveling waves created streamwise vortices lifting the low-speed streaks from the near-wall region and led to a modification of the turbulence bursting events.

Quadrio *et al.* [12] considered waves of spanwise velocity that were imposed at the wall of a turbulent channel flow. Via DNS, they simulated sinusoidal waves of spanwise velocity varying in time and modulated in space along the streamwise direction. Their results showed that the streamwise traveling waves altered the friction drag significantly. Slowly forward

traveling waves produced a large drag reduction that relaminarized the flow at low Reynolds numbers whereas faster waves produce a drag increase. Hurst *et al.* [74] investigated the effect of the Reynolds number on the turbulent drag reduction by streamwise traveling waves. The ranged from a very low Reynolds number of Re_τ = 200 to a high Reynolds number of Re_τ = 1600. The DNS results confirmed that the effectiveness of the drag reduction deteriorates, i.e., the maximum drag reduction decreases significantly when the Reynolds number increases. In addition, they reported that the values of the optimal wave parameters changed when the Reynold number was increased.

Investigations of turbulent drag reduction by manipulating turbulent channel flow via rotating discs have been conducted by Ricco and Hahn [43] and Wise and Ricco [75]. A rigid flush-mounted discs array undergoing steady ration was applied to the channel wall. With a fixed maximum disc tip velocity, either drag reduction or drag increase can be achieved by altering the disc diameter in their DNS simulations. A maximum drag reduction of 23% was computed with the net saved power of 10%. The latter work by Wise and Ricco [75] employed the Fukagata-Iwanato-Kasagi identity [76] to show that the drag reduction is due to two distinct effects. On the one hand, the direct shear of the near-wall rotating-disc on the wall turbulence causes the attenuation of the turbulent Reynolds stress. On the other hand, the effect is related to the additional Reynolds stresses produced by the streamwise long structures existing between discs.

Meanwhile, the traveling surface motions induced by the wall-normal deformation have been investigated intensively. The propagation of traveling surface wave is in either streamwise or spanwise direction. The streamwise and spanwise surface wave motions have been proved both experimentally and numerically to manipulate the near-wall flow structures and to reduce the corresponding friction drag.

Shen *et al.* [77] generated a streamwise traveling surface wave on a flexible flat plate to simulate turbulent flows passing an actively swimming fish. They pointed out that the wall motion can be optimized to achieve separation suppression and turbulence reduction. With a positive wave speed c, turbulence intensity and turbulent shear stress are reduced significantly. Nakanishi *et al.* [78] conducted direct numerical simulations of a fully developed turbulent channel flow and showed that the traveling wave-like wall deformation leads to flow relaminarization, and the reduction of the wall-shear stress is caused by the suppression of random Reynolds stress.

Several recent experimental and numerical studies have examined the drag reduction potential of spanwise traveling surface waves. Itoh *et al.* [79] used a loudspeaker to generate a spanwise traveling surface wave on a flexible polyethylene sheet in a flat plate TBL. By measuring the thickness of the TBL using hot-wire anemometry (HWA), they reported a maximum drag reduction of 7.5% through the completely flexible sheet. A follow-up investigation by Tamano and Itoh [80] analyzed the drag reduction effect using an improved setup. They showed that the drag reduction increased to 13% when the amplitude is increased to A^+ = 24. Klumpp *et al.* [81] investigated a spanwise traveling surface wave by surface deformation with LES. They reported a drag reduction of up to 6% in a TBL. The drag reduction mechanism was attributed to the suppression of the wall-normal vorticity

fluctuations that led to streak instability and formations of new streaks. Tomiyama and Fukagata [82] conducted a parametric study by performing DNS in a channel flow regarding the influence of the wave parameters, i.e., the amplitude, the wave number, and the phase speed. They found that the key feature of the drag reducing mechanism is the damping effect on the near-wall flow structures by introducing a spanwise velocity component. Koh *et al.* [42] investigated the influence of the Reynolds number of the flow and the amplitude of the wave motion on the wall-shear stress of TBLs with spanwise traveling surface waves with wall deformation numerically. Their results showed that the wave amplitude that possesses the maximum drag reduction effect is a function of the Reynolds number. Meysonnat *et al.* [83] analyzed the effect of the pressure gradient based on LES simulations of a similar setup. They found a drag reduction of up to 6% for an APG TBL while the drag reduction increases by up to 4% if the TBL flow undergoes a favorable pressure gradient (FPG). Roggenkamp *et al.* [15] focused on the experimental analysis of friction drag reduction using a spanwise traveling surface wave with wall deformation in TBL flows. The impact of the wave amplitude and the Reynolds number of the flow on the drag reduction effect was investigated.

The literature review shows that both riblets and surface motions reduce the friction drag by influencing the interaction between the near-wall turbulence and the wall. Considering the similarity in the mechanism leading to the drag reduction, it is natural to link the passive and active flow control concepts. Therefore, the German Research Foundation funds the research group FOR1779 focusing on the investigation of passive and active controls. The group consists of several research groups from different scientific fields including fluid mechanics, mathematics, material sciences, and electrical and control engineering. To create a spanwise traveling surface wave, the Central Institute for Electronics (ZEL) of the Forschungszentrum Jülich develops an electromagnet actuator system that is used to locally deflect a rigid surface whose upper side is either smooth or riblet-structured. The Institute of Metal Forming (IBF) at the RWTH Aachen University produces the riblet-structured surface using a cold rolling process. Experimental investigations and numerical simulations are conducted in the Institute of Aerodynamics for fluid mechanical aspects. The previous investigation by Roggenkamp *et al.* [15] showed that it is possible to excite an aluminum surface to generate a surface wave motion with wall deformation. Their results showed that a spanwise traveling transversal surface wave motion reduced the friction by 3.4% above a smooth surface. The drag reduction was increased at a higher wave amplitude and it was decreased with an increasing Reynolds number.

In this work, on the one hand, the experimental investigations concern the drag reduction effect of the rolled riblet surface in TBLs with ZPG as well as with realistic flow conditions, i.e., APG and unsteady inflows. On the other hand, the conjunction of the spanwise traveling transversal surface wave motion and the riblets is investigated. Whether or not a positive interaction can be achieved by the wave motion is investigated by studying the near-wall flow in TBLs.

3 Experimental setup and methods

This chapter introduces the experimental facilities and setups, the measurement techniques, and the post-processing methods of the experimental data. The discussion is divided into four main parts. The first part describes the test facilities including the wind tunnel, the APG setups, the unsteady flow construction, the riblet surface, and the actuator system. The second part provides a detailed discussion on the measurement techniques including HWA, PIV, μ-PTV. The post-processing methods and the uncertainty analysis are discussed in section 3.3. Section 3.4 presents the measurement positions above and downstream of the non-/actuated riblet surface and discusses the influence on the experimental results.

3.1 Experimental facilities

In this thesis, all the experiments are performed in a low-speed Göttingen-type wind tunnel at the Institute of Aerodynamics of the RWTH Aachen University. The wind tunnel has an open test section which measures 1.8 m in length with a cross-sectional area of 1.2 m × 1.2 m. The flow in the wind tunnel is driven by a 100 kW motor with a single stage axial blower. The maximum speed with an empty test section is 60 m/s, and the streamwise turbulent level is less than 0.3% of the freestream velocity. A close-loop control system is used to regulate the flow velocity and the variation of the flow speed is within 0.05%. As shown in figure 3.1, a flat plate with a thickness of 20 mm, a length of 1750 mm and a width of 1200 mm, is installed in the test section. The plate mounting is constructed to allow a fine adjustment of the inclination within $\pm$ 0.15°. The leading edge of the flat plate has a half 3:1 elliptical shape. Downstream of the elliptical leading edge a tripping wire with a diameter of d = 0.5 mm is fixed to ensure the flow transition from laminar to turbulent flow such that a TBL develops. The center of the flat plate is equipped with a flush-mounted insert where an aluminum surface of 330 × 370 mm² can be actuated by a spanwise traveling sinusoidal wave.

The semi-circular riblet surface is produced by the Institute of Metal Forming (IBF) of the RWTH Aachen University. A novel rolling processing technique [8] is developed to produce large-scale riblet-structured sheets. The principal rolling process is shown in figure 3.2. During the production process, a long round steel wire is continuously attached to a flat cylinder resulting in a negatively structured roll. This cylinder is used to form the upper side of the aluminum sheet to riblet structures in the rolling processing. The riblet spacing s is determined by the diameter of the steel wire. The riblet height depends on the rolling force and material.

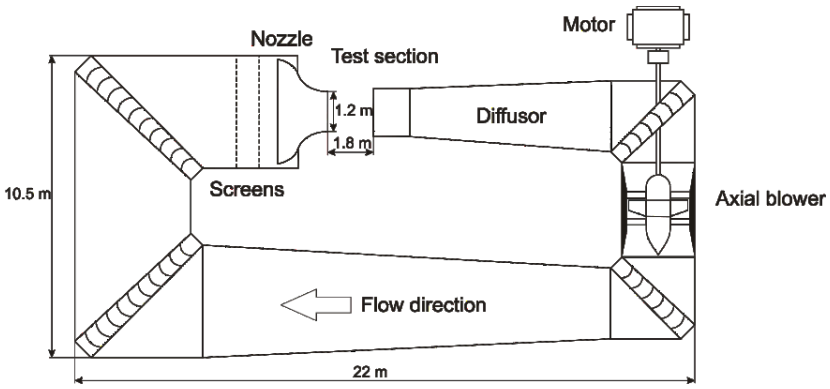

(a)

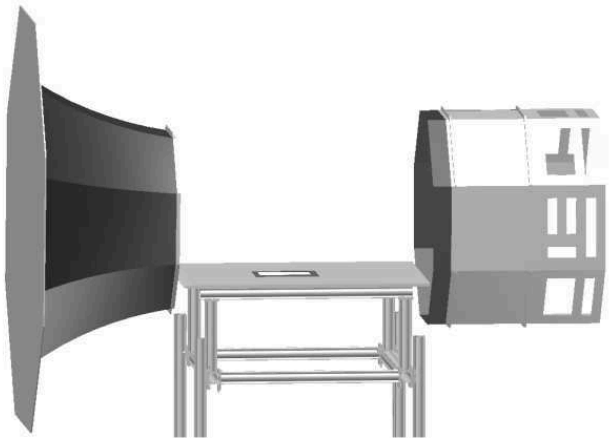

(b)

Figure 3.1: (a) Schematic sketch of the wind tunnel; (b) a 3D model of the test section and the flat plate. A riblet surface can be mounted in the center of the flat plate.

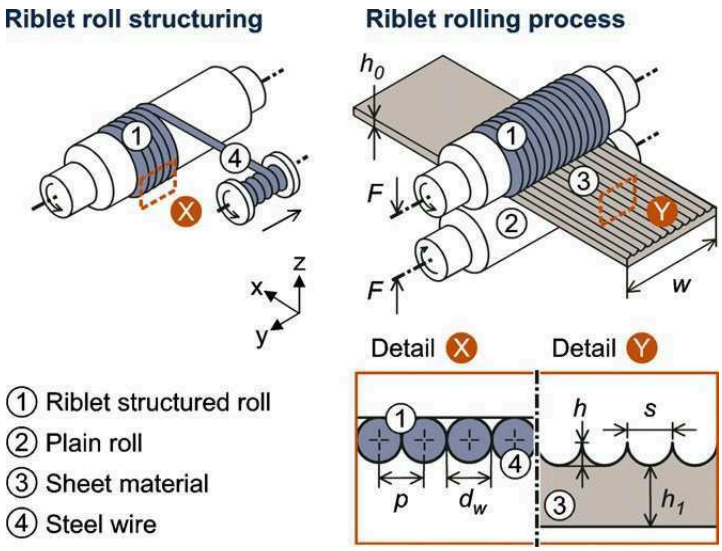

Figure 3.2: Riblet roll structuring and rolling process [8].

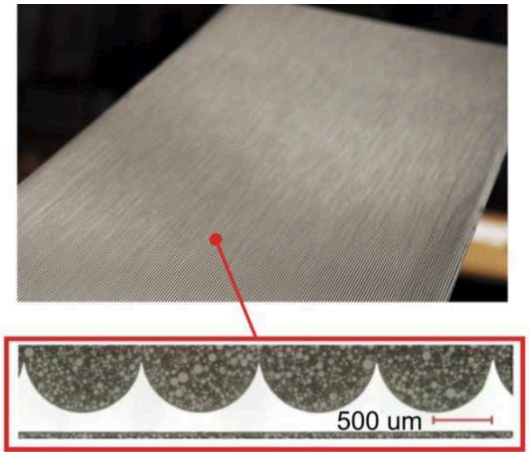

Figure 3.3: Riblet-structured aluminum sheet produced by the IBF and the cross section of the riblet-structured sheet.

To produce a riblet-structured surface that is flexible enough to generate a surface wave motion, a 0.5 mm thick aluminum sheet is processed by the structured 'rolling method'. The diameter of the winding steel wire is 1000 µm resulting in semi-circular riblets with a lateral spacing of the same size and a height of h = 300 µm. In figure 3.3, a sample of the aluminum semi-circular riblet-structured surface is shown. The spanwise dimension of the riblet-structured surface is limited to 220 mm by the width of the roller. The riblet length is limited by the chance of an occurring fracture of the wire. Details of the manufacturing process of the riblets are discussed in Hirt and Thome [8] and Pöplau *et al.* [84].

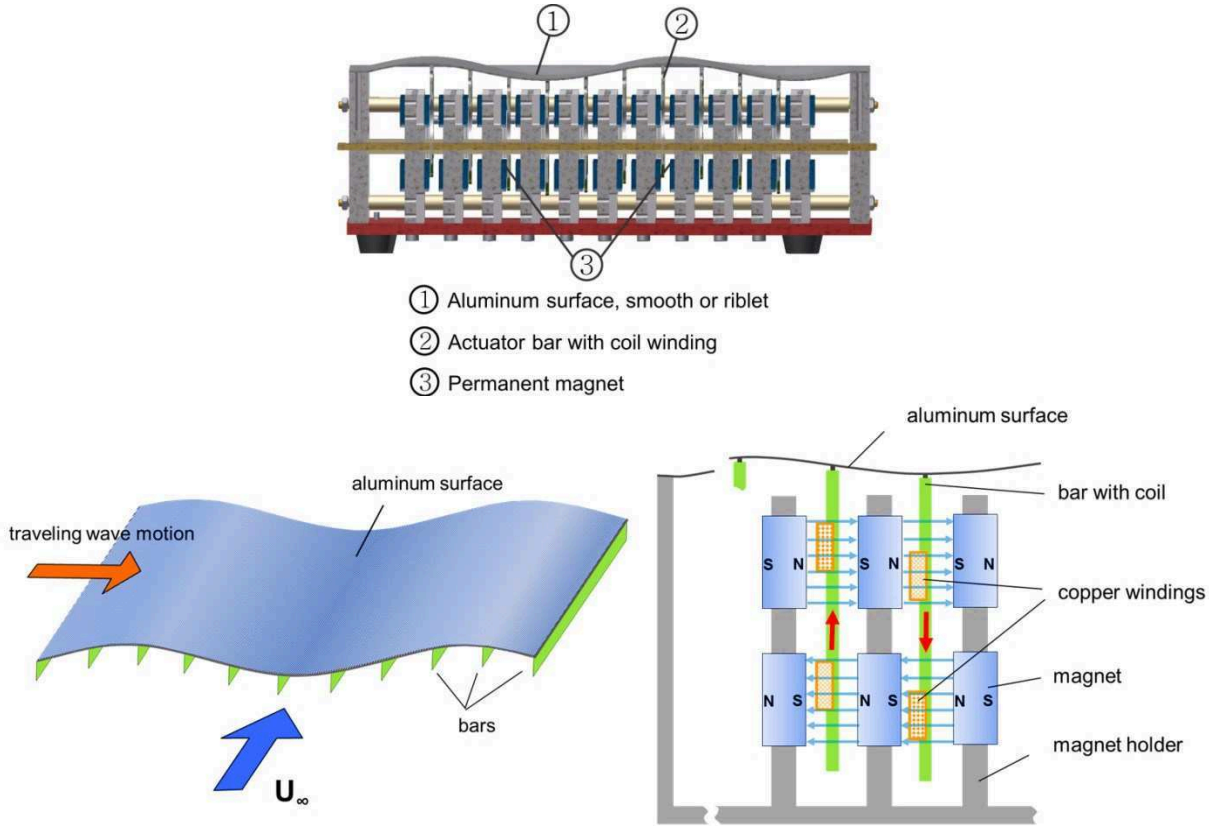

Figure 3.4: The actuator system used to generate a spanwise traveling surface wave.

The spanwise traveling transversal surface wave motion is generated by an electromagnetic actuator system developed by the Central Institute for Electronics (ZEL) of the Forschungszentrum Jülich. It consists of 10 moving actuator bars that are glued to an aluminum sheet from underneath with a lateral spacing of 20 mm aligned in the streamwise direction. Each actuated bar consists of a PCB board and a copper coil of 200 windings located between permanent magnets. All bars are equipped with linear bearings on each end such that they can oscillate in the wall-normal direction. Figure 3.4 shows the operating mode of the electromagnetic actuator system. When it is operated by an alternating current, the actuator bars move up and down in the wall-normal direction resulting in a transversal surface wave motion. The actuator bars are controlled by 3 PCI 6221 multifunction data acquisition cards and 3 current amplifiers which allow the generation of transversal surface waves with an amplitude up to $A = 0.5$ mm and frequencies in the range 0 Hz $< f <$ 160 Hz. The spanwise traveling surface wave is imposed on an aluminum sheet which is located in the center of the flat plate. It measures 350 mm in length and 290 mm in span. Either smooth or riblet-structured aluminum sheets can be installed. Before each measurement, the actuator system is calibrated with a laser displacement sensor Keyence LK-H027 at a sampling rate of 20 kHz.

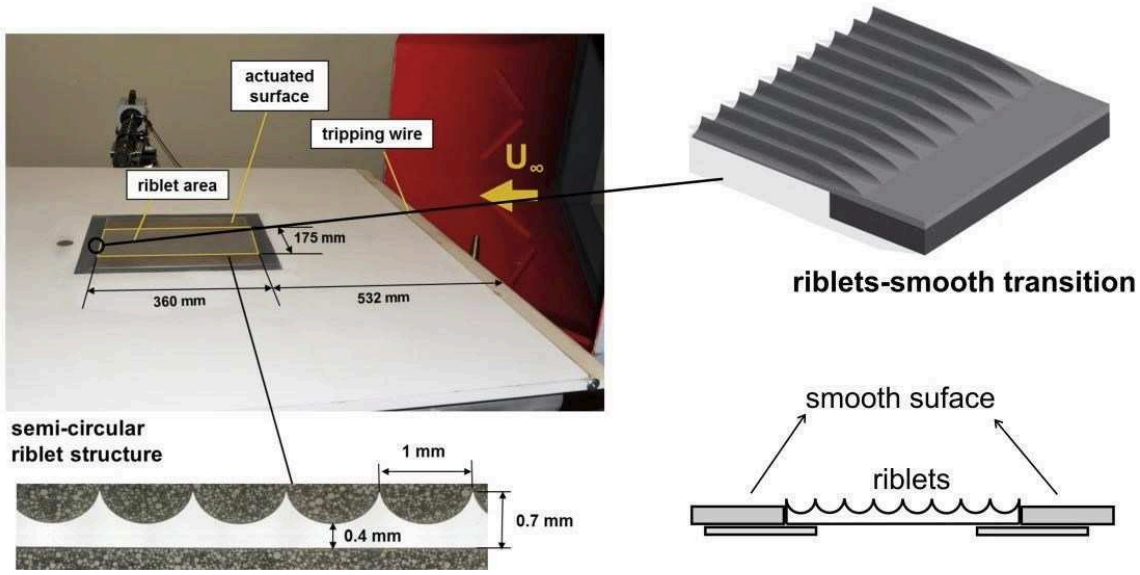

Figure 3.5: The flat plate in the open test section of the wind tunnel with the riblet surface in the center of the actuated domain.

In figure 3.5, the riblet surface together with the actuator system is flash mounted in the flat plate. Since the area of the actuated domain is 350 mm × 290 mm, the width of the riblet sheet is not able to cover it completely. Thus, the riblet sheet is cut into a rectangle area of 175 mm × 360 mm (spanwise × streamwise) and is connected laterally to two pieces of 0.3 mm thick smooth aluminum sheets to fit the actuated domain. The riblet and the smooth surfaces are glued by two pieces of 0.2 mm thick aluminum sheets on the lower side, such that the flow will not be disturbed. The measurements are conducted above and 3 mm downstream of the moving surface. Thus, perturbations due to the transition from the structured surface to a flat one have to be avoided. Special care is taken in the region just

upstream and downstream of the structured area to obtain a smooth transition between the riblet geometry and the flat surface at this position. The smooth transition in the streamwise direction ensures that no impact on the boundary layer flow upstream of the riblet surface is observed and no recirculation occurs downstream of the riblets. For reference measurements, the actuated domain can be replaced by a smooth surface.

The influence of an APG on the drag reduction effect of the riblet surface without and with the spanwise traveling surface wave motion is investigated in sections 5.2 and 6.2.4. To generate an APG, a divergent channel setup is constructed as shown in figure 3.6. The setup is mounted in the test section above the flat plate such that an APG is imposed on the TBL. It consists of two sidewalls and a diffuser-like upper wall with a diverging angle of 16°. A detailed description of the construction of the divergent channel can be found in Roggenkamp [85]. The pressure gradient above the flat plate is determined with 31 pressure tubes located in the streamwise direction. A micromanometer with the minimum resolvable pressure difference of 0.08 Pa is used to measure the static pressure. In figure 3.6, the pressure coefficient defined as $c_p = (p\text{-}p_{ref})/(0.5\rho U_\infty^2)$ is plotted as a function of x / x_{ref}. Here, x_{ref} is the distance between the tripping wire and the leading edge of the actuated domain and p_{ref} is the static pressure at the leading edge of the actuated domain. The pressure gradient dp/dx is characterized by the Clauser parameter $\beta = \delta^*/\tau_w \cdot (dp/dx) = 1.15$. Here, δ^* is the displacement thickness of the TBL and τ_w is the wall-shear stress determined by μ-PTV.

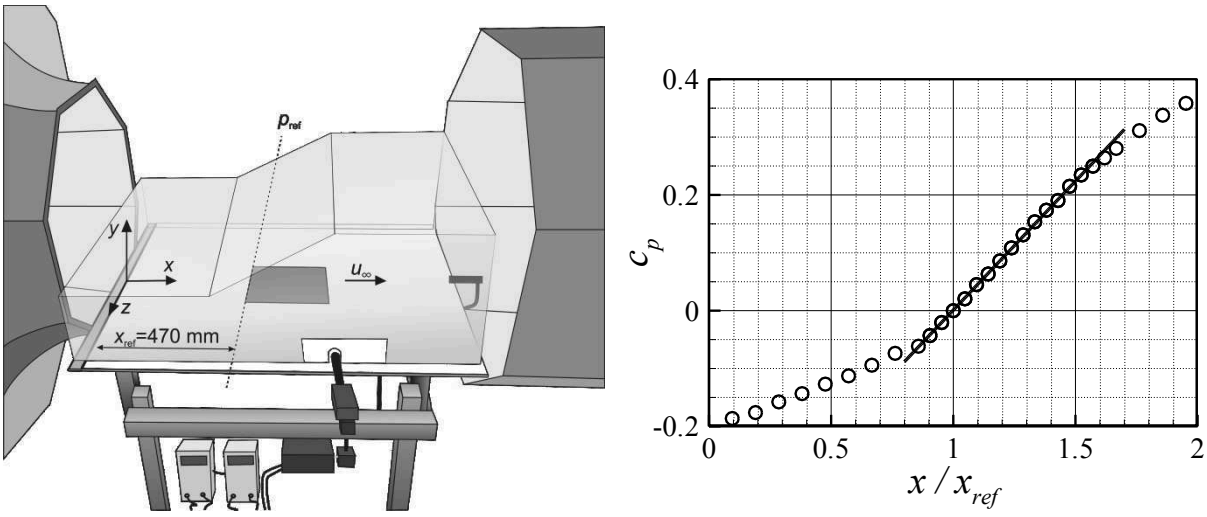

(a) (b)

Figure 3.6: (a) Schematic sketch of the APG setup in the test section of the wind tunnel [85], (b) distribution of the static pressure above the actuated surface.

The influence of a pulsating unsteady inflow condition on the drag reduction effect of the riblet surface is investigated in section 5.3. To establish an unsteady inflow condition, a bypass setup in figure 3.7 is constructed and mounted in the open test section of the wind tunnel. The test section is divided into two sections by three horizontally mounted flat plates. Between the upper and the center plate, a 150 mm wide shutter driven by a stepper motor varies the blockage of the wind tunnel. By driving the shutter with a constant rotation speed, the velocity of the main flow above the lower plate follows a sinusoidal distribution. The

maximum blockage of the shutter is 15% of the test section area, which allows a peak-to-peak velocity fluctuation of more than 10% of the freestream velocity. The distance between the lower and the center plate is 400 mm. This is more than 10 times of the boundary layer thickness when the wind tunnel is operated at 8 m/s. Furthermore, the lower plate consists of two segments. The upstream segment is horizontally mounted to ensure a ZPG whereas the downstream segment can be tilted upwards or downwards to generate a favorable or adverse pressure gradient. A rubber sheet with a thickness of 5 mm is used to fill the gaps between these two segments to ensure that no local flow separation occurs. The riblet surface together with the actuator system is flush mounted in the downstream segment at x = 1410 mm. In section 5.4, a mild adverse pressure gradient of β = 0.53 is generated by tilting the downstream segment downwards with an inclination angle of 2.5°.

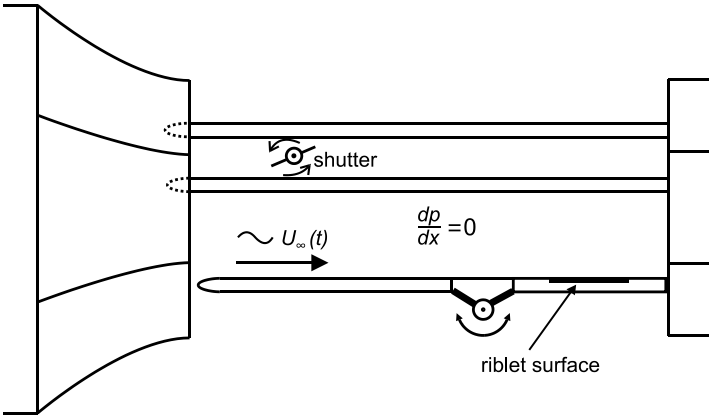

Figure 3.7: Sketch of the unsteady inflow condition setup.

3.2 Measurement techniques

3.2.1 2D-2C PIV, stereo-PIV, and µ-PTV

Particle-image velocimetry (PIV) and particle-tracking velocimetry (PTV) are optical, non-intrusive measurement techniques that capture the velocity field of fluid flows indirectly in a plane or volume. Unlike other flow measurement techniques using sensors or probes, e.g., HWA, pressure sensors, or Pitot tubes, PIV and PTV do not measure the flow properties themselves, but rather the velocity of small particles that are added to the flow. The experimental setup of a PIV or PTV system usually consists of several parts including tracer particle generator, light source, recording device and post-processing software. The flow is seeded by small tracer particles which are illuminated in a plane or a volume by a light source within a short time interval. A recording device records the particle distributions either on a double-exposure frame or on a sequence of frames. In the post-processing, the corresponding particle displacement is calculated from the images. The particle displacement between the two exposures is determined using cross-correlation or auto-correlation algorithms for PIV and a tracking algorithm for PTV. The flow velocity field is determined by converting the image coordinate to the world coordinate by a calibration process. Figure 3.8 shows a standard PIV setup in a wind tunnel experiment. The PIV setup contains tracer particles, a laser as light source, optics to generate a laser light sheet that illuminates the measurement area, and an image acquisition system to capture the particle images in the measurement

plane. By determining the displacement $\Delta\vec{s}$ and the time interval Δt of the double-exposure frame or image sequence, the velocity $\vec{v}$ is determined by $\vec{v} = \Delta\vec{s} / \Delta t$.

According to the general principles of PIV and PTV measurement techniques, several requirements have to be fulfilled by the measurement setup so that the velocity field can be measured accurately. The tracer particles have to follow the flow, i.e., the velocity of the tracer particles has to be close to the flow velocity. Usually, small particles follow the flow better. Secondly, the displacement of the particles should be captured precisely. Furthermore, the time interval Δt between the image pairs needs to be small enough compared to the time-scales to resolve all phenomena of interest. Thus, the determined velocity field can be considered as an instantaneous flow field.

In modern PIV or PTV measurements, the particle images can be acquired by either complementary metal-oxide-semiconductor (CMOS) or charged-coupled device (CCD) camera system. The duration of the exposure must be short enough to freeze the motion of the particle in order to avoid that the moving particles are imaged as streaks. The light source has to provide a significant energy density within a short exposure time to ensure a high signal to noise ratio of the particle images. Lasers or LEDs in continuous or pulsed mode are used for the illumination.

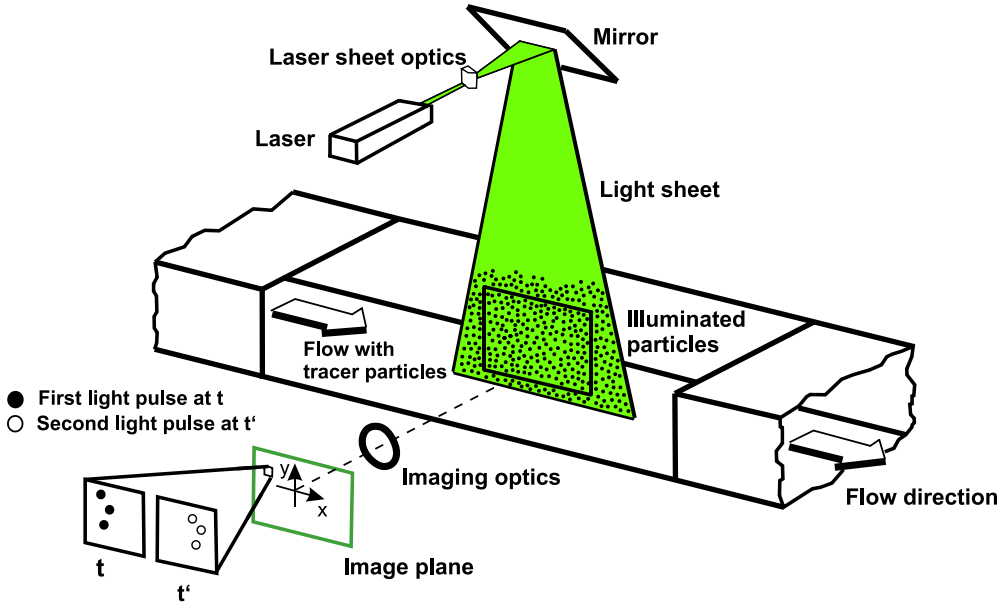

Figure 3.8: Schematic of a standard 2D-2C PIV setup.

As discussed in chapter 2, the viscous sublayer of a TBL is a thin region with a height of 4 - 5 wall units close to the wall. The height of the viscous sublayer is determined by the friction velocity of the flow, i.e., $y \leq 5\nu/u_\tau$. Given the flow conditions in this thesis, the height of the viscous sublayer is smaller than 200 µm. This requires measurement techniques that are able to resolve the flow field with a spatial resolution of several or tens of microns. For PIV the interrogation window size of 16 × 16 pixels is usually needed to ensure a sufficient particle number for the auto- or cross-correlation. This leads to a spatial resolution in an order of 0.1 mm, which is not sufficient to resolve the flow field in the viscous sublayer. Therefore,

the micro-particle-tracking velocimetry (μ-PTV) technique is applied to enhance the spatial resolution by using a long working distance microscope and a particle-tracking algorithm.

For both techniques, the TBL flow is seeded by Di-2-Ethyl-Hexyl-Sebacat (DEHS) droplets with a mean diameter of approximately 1 μm. The DEHS droplets are generated by high pressure driven Laskin nozzles. For the PIV measurements, the wind tunnel flow is full-field seeded to ensure a homogeneous particle distribution. However, for the μ-PTV measurements, the field of view (FOV) has to be magnified significantly near the wall. This requires a higher particle concentration than that of the global seeding. Hence, a seeding nozzle is mounted 200 mm upstream of the leading edge of the flat plate to ensure a sufficient local particle concentration close to the wall as suggested by Kähler *et al.* [86]. To avoid the disturbance by ejecting high-speed flow into the flow, the seeding particles are sucked into the main flow from a plenum that contains air with a high particle concentration.

The intensity of the particle image is directly related to the power of the light source. Usually, highly intensive light sources are used in PIV and PTV measurements to illuminate the tracer particles. In this study, a double-pulse Q-switch laser (Twins BSL 140) from Quantel is used to illuminate the tracer particles. The laser has a maximum energy of 140 mJ per pulse with a maximum double-pulse repetition rate of 30 Hz. Its pulse width is 8 ns, which is able to 'freeze' the particle image to avoid the recording of the blurred motion due to the tracer particle movement. The laser beam generated by the Twins BSL 140 laser is guided by a light arm which contains a set of reflecting mirrors to a set of optical lenses. These lenses form a light sheet with a thickness of 0.3 - 0.5 mm so that the flow can be illuminated in different measurement planes.

Several different types of high-speed CMOS cameras, e.g., SA3, SA5, and PCI 1024 from the Fastcam series of Photron and the Sensicam QE double-frame CCD camera from PCO are used to capture the particle image pairs. The high-speed Fastcam cameras have a full frame resolution of 1024 × 1024 pixel with a frame rate of up to 7000 Hz and the Sensicam QE possesses a full frame resolution of 1376 × 1040 pixel and a maximum frame rate of 10 Hz. To ensure a better spatial resolution in PIV, Tamron macro lenses with a focus length of 180mm and teleconverters with a magnification factor of 2 are coupled with the cameras to capture the particle images. The FOV of the PIV measurements covers the complete height of the TBL, which is dependent on the measurement position and the freestream velocity. For the μ-PTV measurements, the cameras are equipped with a long distance microscope from K2 Infinity to record the particle image pairs. Three zoom lenses are used for the Fastcam cameras and two are used for the Sensicam QE camera to resolve the required FOV. The zoom lenses have a magnification factor of 2 leading to a total magnification factor of about 10 and an FOV of approximately 2 mm × 2 mm when they are coupled with the long distance microscope. Due to the significant loss of light intensity caused by the zoom lenses, a high light intensity is required in the μ-PTV measurement. Therefore, the laser light sheet is focused by an extra concave cylindrical lens to a size of 0.5 mm × 2 mm in the μ-PTV measurement to increase the light energy density.

The cameras and the laser are externally controlled by a synchronizer to capture the sequence of particle image pairs. The time delay Δt between the first and the second laser pulse is

adjusted dependently on the flow velocity and the FOV to ensure a sufficient particle displacement for a large measurement dynamic range. In PIV measurements, a particle image displacement in the order of 10 pixels is required to ensure a significant dynamic range. For the µ-PTV measurements, a much larger displacement of 25 pixels is reached due to the high magnification factor of the long distance microscope. Furthermore, to determine the wall-shear stress distribution and the flow field above the moving surface, the PIV and µ-PTV are synchronized with the wave motion. As shown in figure 3.9, the laser and the cameras are triggered such that the PIV or µ-PTV measurements always occur at a certain phase of the sinusoidal wave motion.

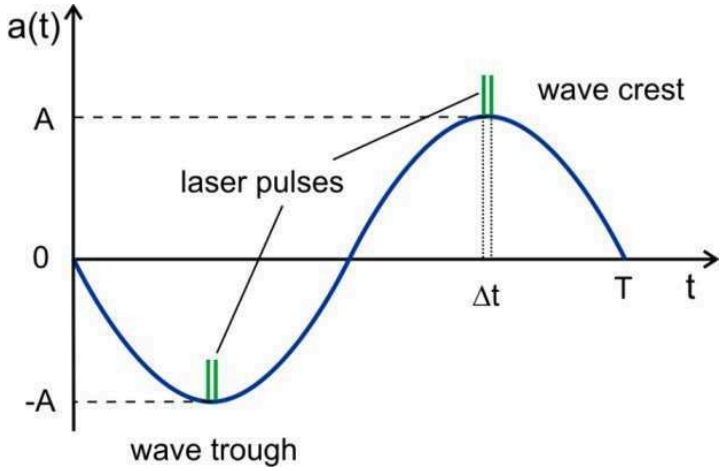

Figure 3.9: Synchronization of the PIV and µ-PTV measurements above the actuated surface.

The 2D-2C standard PIV is only capable of measuring the velocity components in a two-dimensional plane. To measure the out-of-plane velocity component, stereoscopic particle-image velocimetry (stereo-PIV) is applied by using a second camera to achieve a stereoscopic view of the flow field. Both cameras are tilted to observe the same FOV from different viewing angles. To ensure sharp images of the particles in the measurement plane, the Scheimpflug condition [87] has to be fulfilled. Therefore, the lens plane is tilted with respect to the recording plane of the camera. The two cameras record different projections of the velocity vector of the particles. Thus, the complete velocity vector can be reconstructed. The velocity vector of a single interrogation window is calculated by using equations 3.1 - 3.7. The quantities x_i, x_i', y_i, y_i' define the projections of the tracer particles in the x and y directions at t and t' with i = 1, 2 indicating the two cameras, respectively. The variables α_i and β_i are the angles between the z axis and the ray from the tracer particles through the lens center to the recording plane. Here, α is in the x-z plane and β is in the y-z plane.

$$\tan \alpha_i = \frac{x_i(t')}{z_o} \tag{3.1}$$

$$\tan \beta_i = \frac{y_i(t')}{z_o} \tag{3.2}$$

The magnification factor of the lenses are defined by M. To apply the velocity reconstruction, the displacement of the particles in pixels has to be converted to the true displacement in a common coordinate system. A target with regular grids is placed in the measurement plane to transform the image coordinate to the world coordinate. The two calibration images from

both cameras are mapped on a common grid to calculate the velocity vectors. The mapping function is calculated by using a pinhole model. Then, the original particle images from both cameras are mapped and dewarped to the common grid. The 2D velocity fields from both cameras are calculated using equations 3.3 and 3.4 with standard PIV algorithm. Here, the velocity components measured by both cameras are given by u_i and v_i. Finally, the three components of the velocity vector are determined by the reconstruction using equations 3.5 - 3.7 as shown in figure 3.10 (a).

$$u_i = \frac{x_i(t') - x_i(t)}{M \cdot (t' - t)} \tag{3.3}$$

$$v_i = \frac{y_i(t') - y_i(t)}{M \cdot (t' - t)} \tag{3.4}$$

$$u = \frac{u_1 \cdot \tan\alpha_2 + u_2 \cdot \tan\alpha_1}{\tan\alpha_1 + \tan\alpha_2} \tag{3.5}$$

$$v = \frac{v_1 \cdot \tan\beta_2 + v_2 \cdot \tan\beta_1}{\tan\beta_1 + \tan\beta_2} \tag{3.6}$$

$$w = \frac{u_1 - u_2}{\tan\alpha_1 + \tan\alpha_2} \tag{3.7}$$

In figure 3.10 (b), the measurement area in the plane perpendicular to the wall-normal direction above the moving surface is illustrated. Two PCI 1024 high-speed cameras coupled with two Tamron 180 mm macro lenses and 2× teleconverters are used to capture the particle image pairs. The FOV of the stereo-PIV is about 40 × 40 mm covering one-quarter of the wavelength.

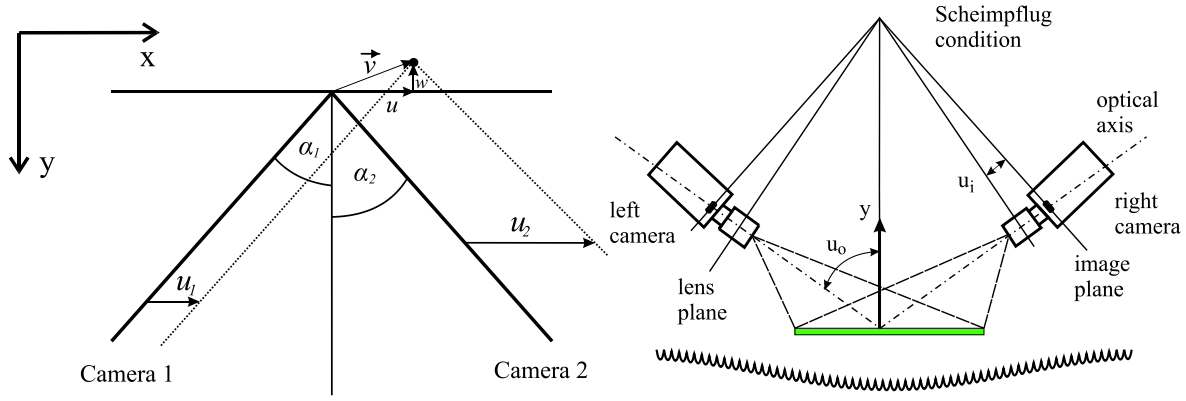

(a) (b)

Figure 3.10: (a) Stereo viewing geometry in the *x-z* plane [87], (b) Schematic sketch of the 2D-3C stereo-PIV configuration.

3.2.2 Near-wall hot-wire anemometry

A hot-wire anemometer is a device that is used to measure the variables occurring in flows, such as mean and fluctuating velocity, energy spectrum, and temperature. It is based on convective heat transfer from a heated wire placed in the flow. The heat transfer from the heated wire to the flow is affected by any change of the flow condition. This change is detected instantaneously by a constant-temperature anemometer (CTA) with servo-loop technique. The information related to the flow is recorded and is translated to the flow

properties through a calibration process. HWA can be used to measure turbulent flows of fine scales and high frequency by using very small sensors and high-temporal resolution CTA system. Usually, an HWA system consists of a probe, a CTA anemometer, and an A/D converter. In addition, a highly accurate traverse system is often used to position the probe in the flow such that profiles can be investigated.

To validate the PIV and μ-PTV techniques of measuring the properties of TBL flows, near-wall hot-wire measurements are conducted at a freestream velocity of 8 m/s. The position of the measurements is located at x = 895 mm above the aluminum surface insert where PIV and μ-PTV measurements are conducted as well. In order to avoid the oscillation of the probe, the hot-wire probe which is shown in figure 3.11 is integrated into the flat plate.

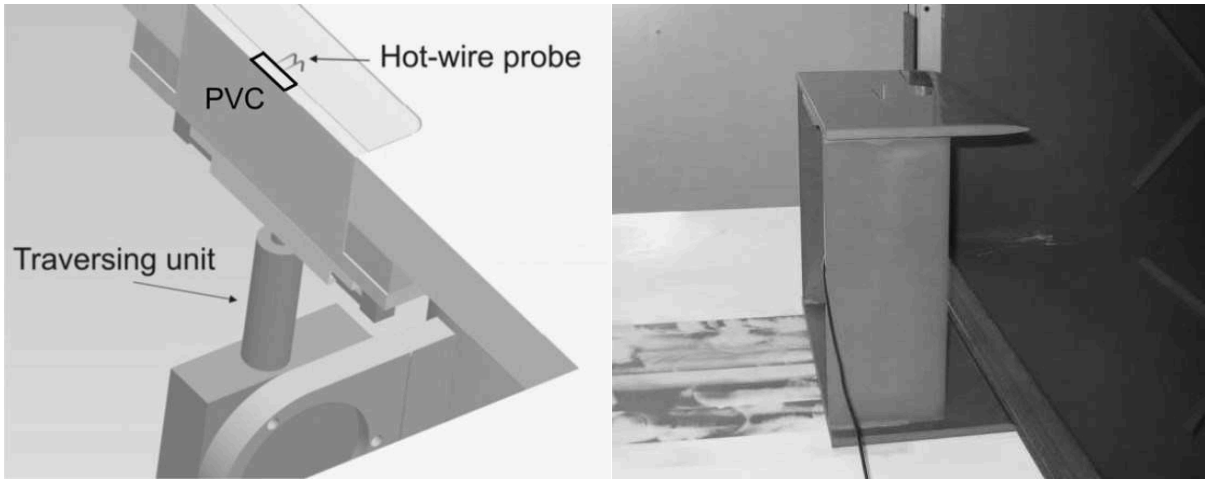

(a) (b)

Figure 3.11: The near-wall hot-wire probe and the calibration configuration.

Due to additional heat transfer from the heated wire into the wall, HWA measurements in the near-wall region are distorted by the so-called wall-effect. This effect is reviewed by Hutchins and Choi [88] and their results show that the wall-effect started to affect the measurement results when the hot-wire approached the wall below $y^+ < 3.5$. Here, a PVC insert is used to replace the wall under the hot-wire probe to reduce the heat transfer from the heated wire to the wall. The gap between the PVC insert and the aluminum surface is filled with wax and the surface is well polished so that no step and gap remains.

The length of the tungsten hot-wire is L = 1 mm corresponding to $L^+ = L\, u_\tau / \nu = 24.1$ in the TBL with a Reynolds number of $Re_\theta = 1200$ based on the momentum thickness. The diameter of the wire is d = 5 μm which gives L / d = 200. The literature review by Ligrani and Bradshaw [89] shows that the spanwise spatial resolution of hot-wire is related to the length of the wire in wall unit. For accurate measurement in TBLs, L^+ needs to be less than 20 to resolve the small structures and the length-to-diameter ratio needs to be equal or larger than 200 to avoid the end-conducting effect. Thus, the required length of the wire is not accomplished for measuring the spectral composition of the velocity fluctuations in the current measurements. Nevertheless, according to Hutchins *et al.* [90], the mean values of the velocity distribution are not affected by the wire length so that the hot-wire measurements can be used to validate the PIV and μ-PTV data.

An IFA 100 CTA system in conjunction with an ME4660 sPCI 16 bit A/D converter is used for the data acquisition. The hot-wire measurements are performed in the constant temperature mode with an overheat ratio of 50%. An offset and a gain are applied to the CTA to make use of the voltage range ± 5 V of the A/D converter. The data sampling rate is 20 kHz and the measurement duration is 20 seconds for each measurement point ensuring data convergence. In addition, a high pass filter with a cut-off frequency of 10 Hz filters out the low-frequency noises.

For the calibration, the hot-wire probe is inserted into a miniature plate which is fixed above the large flat plate in the wind tunnel (see figure 3.11 (b)). The hot-wire is located 7 mm above the miniature plate whose boundary layer thickness is less than 4 mm. This ensures that the probe is calibrated in the freestream flow. To determine the velocity of the freestream, a micromanometer is used to read the dynamic pressure from a Prandtl tube that is fixed near the hot-wire probe. The calibration consists of 15 points and a curve describes the relation between the velocity u and the voltage e from the CTA. Since the flow velocity ranges from zero at the wall to the freestream velocity in a TBL, the calibration requires the data points down to 0 m/s. This needs the voltage from the CTA under no flow condition is recorded. According to Bruun [91], the relation which is known as the King's law between u and e is used to determine the calibration curve, i.e. $e^2 = A + B\,u^n$. The coefficients A, B, and n of the King's law are defined by a best fitting approach. For each measurement, two calibrations are conducted before and after the measurement campaign. If the calibration varied more than 1%, the measurement data are discarded.

A stepper motor coupled with a reduction gear is used to position the hot-wire probe in the wall-normal direction. The travel range is from 0 to 7 mm with a step width of 0.3 µm. This only allows the measurement of the TBL in the inner layer. The position of the hot-wire is determined by moving the wire until it contacted a brass cylinder lying on the wall. The contact generates an electrical signal that triggers the step-motor to stop. The diameter of the cylinder is 3.055 ± 0.001 mm. Thus, the absolute position of the hot-wire is determined. A similar approach was performed by Nottebrock [92] as well. He pointed out that the gear clearance and tolerance have to be taken into consideration. The position of the hot-wire is double checked by a high-resolution PCO 4000 camera coupled with a K2 Infinity long distance microscope with a spatial resolution of 1.319 µm / pixel. It shows that the clearance and the tolerance of the gear lead to a maximum misposition of ± 5 µm.

To resolve the TBL with a proper spatial resolution, more than 50 measurements points are located in the wall-normal direction. The initial measurement step is 500 µm at y = 6.5 mm, and it decreases to 50 - 200 µm when the probe approaches the wall. In the region of y < 200 µm, the measurement step is reduced to 10 µm corresponding to 0.25 wall units to resolve the velocity distribution in the near-wall region.

3.3 Data post-processing and measurement uncertainty analysis

3.3.1 Data post-processing

The PIV data is evaluated with a multigrid algorithm based on window cross-correlation. First, a cross-correlation with a relatively large window size, e.g., 96 × 96 or 64 × 64 pixels is performed such that the displacement is predicted. Then, the window size is refined for the final integration base on the predicted displacement. The multigrid algorithm allows a large dynamic range which is important for the measurement of shear flows with large velocity gradient. The final interrogation window size differs from 16 × 16 to 32 × 32 pixels in the different measurement sets, such that there are 6 - 8 particles per interrogation window. The overlap of the interrogation windows is set to 50%. The invalid vectors are detected by using a normalized median test over 3 × 3 vectors according to Westerweel and Scarano [93] and are replaced by interpolated vectors. For the instantaneous vector fields, the cross-correlation results indicate more than 99% valid vectors.

The μ-PTV data is post-processed by an in-house code based on the work of Crocker and Grier [94]. The images are first pre-processed using a spatial bandpass filter to smooth the image and subtract the background. Then the centroids of the bright particles are calculated to sub-pixel accuracy. Finally, the displacement of each particle per image pair is determined by the tracking algorithm. The accuracy of the particle-tracking method depends on the particle spacing Δx_p in one image and the particle displacement Δx between the two images of an image pair, where Δx_p has to be considerably larger than Δx. Malik *et al.* [95] concluded that $\Delta x_p = 5 \cdot \Delta x$ resulted in more than 98% valid links between particles for synthetic particle images. In the measurements of this thesis, the averaged particle spacing Δx_p and the maximum particle displacement Δx differ with different FOVs and freestream velocities. Overall, the minimal ratio of the particle spacing and the displacement is $\Delta x_p / \Delta x \geq 4.5$. The tracking algorithm yields valid links for more than 98%. Outlier vectors are detected by a window velocity filter specifying a lower and an upper limit for each velocity component. Furthermore, the flow field is divided into intervals in wall-normal direction. Those vectors in one interval that deviate more than three standard deviations from the mean velocity are considered as invalid vectors as well. In each interval, the velocity vectors from the complete sequence are used to determine the statistics of flow, e.g., mean velocity, fluctuations, and Reynolds shear stress.

As mentioned before, the additional heat loss due to the heat transfer from the wire to the wall causes distorted results. Even although the wall bellow the hot-wire probe is replaced by less heat conductive material, the wall-effect cannot be completely avoided. In figure 3.12 (a), the velocity distribution near the wall is plotted to show the wall-effect. It is noticed that the measured velocity is not zero at the wall and the velocity gradient decreases when the hot-wire approaches the wall. Therefore, the diagnostic plot performed by Alfredsson and Örlü [96] is used to examine the viable measurement data in the near-wall region at $Re_\theta = 1200$. In figure 3.12 (b), the root-mean-square of the fluctuation velocity u'_{rms} are plotted against the mean velocity U. A tangent starting from the origin to the near-wall data points with a slope of 0.38 is plotted to determine the biased data points. The measurement data points that do

not lie on the tangent are affected by the wall-effect. These measurement points are marked as distorted data and are discarded in the analysis of the turbulent statistics. The dashed line shows the demarcation point and eventually, the data points below $y^+ < 3.8$ are discarded for the measurement of $Re_\theta = 1200$.

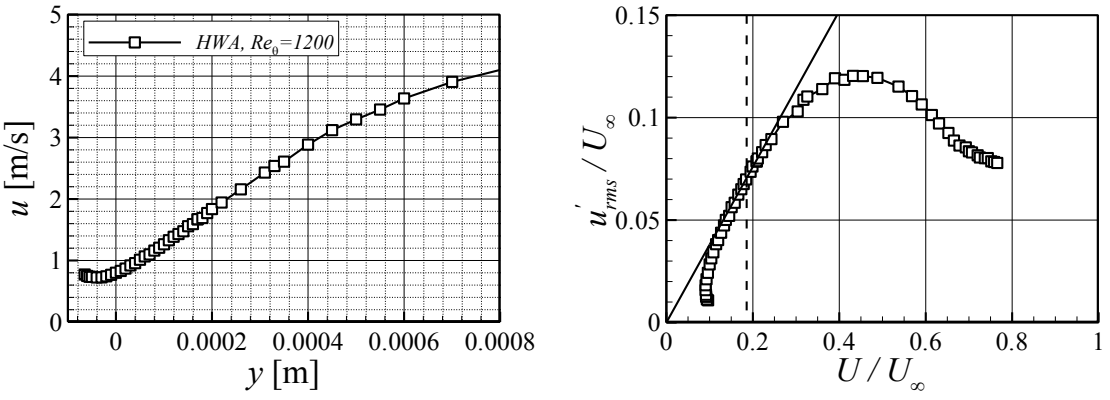

(a) (b)

Figure 3.12: (a) HWA measurement in the near-wall region, $Re_\theta = 1200$; (b) Diagnostic plot for the hot-wire data.

3.3.2 Measurement uncertainty analysis

Accurate PIV measurements of the properties of wall-bounded flows, e.g., velocity distribution, fluctuations, and wall-shear stress, are challenging in large-scale wind tunnels due to the strong velocity gradient and the low concentration of the tracer particles. Furthermore, in turbulent flows, the statistical uncertainty is associated with the sampling of random processes that can lead to errors on the measured turbulence quantities. Thus, the analysis of the measurement uncertainty of the techniques and the statistical uncertainty due to the limited sampling of turbulent flows are presented in this subsection.

According to Kähler *et al.* [86], the uncertainty due to the measurement error of PIV and μ-PTV mainly associated with the (1) dynamic of the tracer particle, (2) light sheet orientation relative to the model and flow, (3) accuracy of the calibration target and the magnification factor, (4) precision of the time delay between the two illuminations, (5) image analysis.

(1) The dynamic of the tracer particle in turbulent flows has been discussed in Melling [97]. It has been showed that the response frequency is up to 10 kHz for olive oil droplets with a diameter of 0.98 μm. The DEHS tracer particles used in this thesis have a similar density ratio and diameter to the olive oil droplets. The error due to the dynamic of the tracer particle can be neglected.

(2) The light sheet orientation has to be considered due to the systematic error caused by the misalignment of the light sheet to the measurement plane. The error due to the light sheet orientation is a function of the sine and it is less than 0.015% for a misalignment up to 1 degree.

(3) The error due to the calibration and the magnification factor according to Kähler *et al.* [86] with a similar setup is less than 0.025% and 0.015%.

(4) The laser and the synchronizer determine the precision of the time delay of the image pairs. According to the laser manufacturer, the timing jitter is ± 2 ns. The error due to the time delay between the illuminations is below 0.07% regarding the minimum time delay of 3 µs.

(5) The evaluation uncertainty of the window-correlation-based algorithm is in an order of 0.05 pixels. Thus, based on the particle displacements outside the boundary layer flows that reach values of 10 pixels, it leads to a relative measurement error about 0.5%. For the µ-PTV post-processing, the error for the particle location is on average $\Delta\varepsilon$ = 0.04 pixels. It is equivalent to an error of 1.5% in the near-wall region for the streamwise velocity.

The statistical uncertainty that is associated with the sampling of random processes is analyzed based on the large sample theory. According to Benedict and Gould [98], a 95% confidence interval of the true value $\bar{m}$ falls within the interval $\bar{m} \pm 1.96\sqrt{var(\bar{m})}$, where $var(\bar{m})$ is the variance of the measurement value. The theoretical sampling error of the mean velocity U in a turbulent boundary layer within a 95% confidence interval is $\Delta U = 1.96\sqrt{var(U)}$. The variance of the mean velocity component U is given by $\mathrm{var}(U) = \overline{u'^2}/N$. For the second-order statistics, i.e., the streamwise velocity fluctuation u'_{rms}, the variance is $\mathrm{var}(u'_{rms}) = [\overline{u'^4} - (\overline{u'^2})^2]/(4N\overline{u'^2})$. Based on that, the statistical uncertainty of the mean streamwise velocity component U and the velocity fluctuation u'_{rms} are shown in figure 3.13. The statistical uncertainty as a dependent variable of the sampling number N is plotted in a semi-log scale. Considering a sample number of $N = 2000$, the maximum theoretical sampling error of the mean streamwise velocity is less than 1% for a 95% confidence interval in the PIV measurements. The maximum error of the streamwise turbulence fluctuation u'_{rms} is less than 3%. For the µ-PTV data, since the statistics is based on the ensemble flow field, the statistical uncertainty is plotted along the wall-normal direction. The maximum theoretical sampling error is less than 0.5% for the mean streamwise velocity in the near-wall region of $0.5 < y^+ < 8$ and less than 1.4% for the streamwise turbulence fluctuation u'_{rms}.

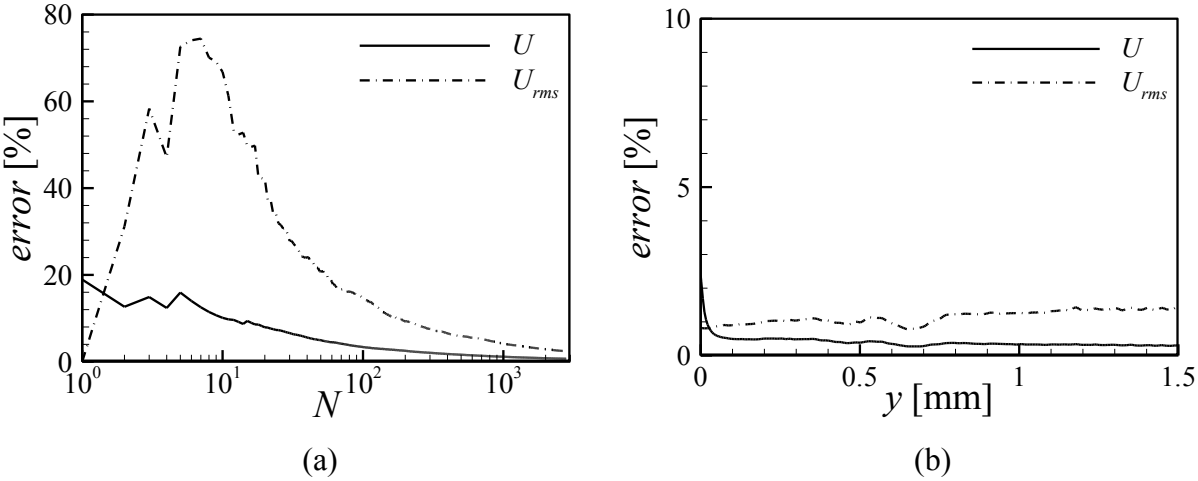

Figure 3.13: Statistical uncertainty of the mean streamwise velocity and fluctuation, (a) PIV data at the near-wall position, y ≈ 1 mm as a dependent variable of the sampling number N. (b) µ-PTV data along the wall-normal direction of the ensemble flow statistics.

3.3.3 Determination of wall-shear stress and drag reduction ratio

The wall-shear stress and the friction velocity are determined by using a least-square linear fitting method of the mean velocity gradient in the viscous sublayer. This method relies on the property of the viscous sublayer in which the velocity increases linearly with increasing wall-normal distance, i.e., $U^+ = y^+$, with $y^+ = yu_\tau / \nu$ and $U^+ = u / u_\tau$. The wall-shear stress is estimated as $\tau_w = \mu \partial U/\partial y \cong \mu dU/dy$. Measurements of the wall-shear stress by this method have been performed by, for instance, Durst *et al.* [99] with laser doppler anemometry (LDA), Hutchins and Choi [88] with HWA, Kähler *et al.* [86] and more recently Roggenkamp *et al.* [15] and Li *et al.* [100] with μ-PTV. In figure 3.14, the wall-shear stress is determined from the velocity distribution measured by μ-PTV. A linear line is used to fit into the scattered experimental data to determine the velocity gradient dU/dy in the viscous sublayer. More than 20 data points are used in the region of $y^+ < 3.5$ at $Re_\theta = 1200$. For the measurement at the highest Reynolds numbers of $Re_\theta = 4070$, the high-spatial resolution μ-PTV measurements ensure more than 10 data points in the region of $y^+ < 3.5$ to achieve a satisfactory linear fitting.

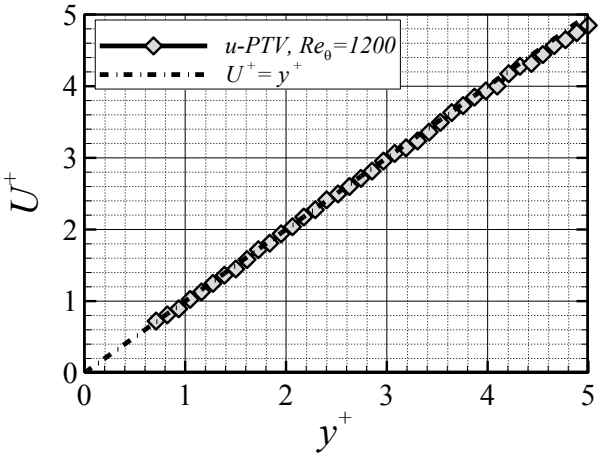

Figure 3.14: Determination of the wall-shear stress from the velocity distribution in the viscous sublayer.

The error of the determination of the wall-shear stress mainly comes from two aspects. On the one hand, the possible measurement error stems from the nonlinear property of velocity distribution in the viscous sublayer. In fully developed turbulent channel and boundary layer flows, the relation $U^+ = y^+$ is only valid in the 'linear region' of $y^+ < y^+_v$ (where $y^+_v = 3 \sim 4$) according to Cenedese *et al.* [101]. When the velocity distribution is beyond the region $y^+ < y^+_v$, an underestimation of τ_w happens when using this method. Thus, to reduce this error, the linear fitting is always conducted in the region of $y^+ < 3.5$. On the other hand, the uncertainty of determining τ_w can come from the least-square linear fitting of the scattered experimental data. According to Hutchins and Choi [88], the error analysis can be conducted easily. A linear line in the form of $u = ky + y_0$ is matched to the velocity distribution in the 'linear region' from the μ-PTV measurement. Here k is the gradient of the velocity in the fitting region and y_0 is the offset of the wall-normal position of the measurement coordinate system. By using a least-square linear fitting, the gradient k is of the form,

$$k = \frac{\sum_{i=1}^{n}(y_i - \bar{y})(u_i - \bar{u})}{\sum_{i=1}^{n}(y_i - \bar{y})} \tag{3.8}$$

and $y_0 = \bar{u} - b\bar{y}$.

Here, $\bar{u}$ is the arithmetic mean of the velocity data set and $\bar{y}$ is the mean wall distance with the wall offset. The estimation for the standard errors of the calculation for k and y_0 are given in the following according to Box *et al.* [102]. The standard error of the wall-shear stress and the wall-normal offset y_0 due to least-squares fitting is

$$S.E.(k) = \frac{\sigma_u}{[\sum_{i=1}^{n}(y_i - \bar{y})^2]^{\frac{1}{2}}} \tag{3.9}$$

and the standard error of the offset of the wall position is

$$S.E.(y_0) = \sigma_u \left[\frac{1}{n} + \frac{\bar{y}^2}{\sum_{i=1}^{n}(y_i - \bar{y})^2}\right]^{1/2} \tag{3.10}$$

Where

$$\sigma_u^2 = \frac{\sum_{i=1}^{n}(u_i - \bar{u})^2 - b\sum_{i=1}^{n}(y_i - \bar{y})(u_i - \bar{u})}{n-2} \tag{3.11}$$

The local drag reduction ratio (DR) is determined from the variation of the local skin friction coefficient $C_f = \tau_w/(\frac{1}{2}\rho U_\infty^2)$:

$$\mathrm{DR} = \left(\frac{C_{f,smooth} - C_{f,non-/actuated\ riblet}}{C_{f,smooth}}\right) \times 100\% \tag{3.12}$$

Here, $C_{f,smooth}$ is the local skin friction coefficient of the surface without the surface wave motion, and $C_{f,non-/actuated\ riblet}$ is the local skin friction coefficient of the riblet configurations.

3.4 Measurement positions and flow recovery effect

To investigate the impact of riblets and the conjunction with the spanwise traveling transversal surface wave motions on the TBL flows, µ-PTV and PIV are conducted at two streamwise measurement positions above (M1) and downstream of the riblet surface (M2). The measurement position M1 is located 230 mm downstream of the leading edge of the inserted aluminum plate, i.e., x = 772 mm. The experiments at M1 are conducted by the phase-locked µ-PTV and PIV measurements to determine the flow above the surface wave. The measurement position M2 is located 3 mm downstream of the riblet surface. The size, orientation, and positions of the measurement planes are shown in figure 3.15.

Before the drag reduction effect of the semi-circular riblets is investigated by comparing the corresponding near-wall velocity profiles with those smooth surfaces, the spanwise impact of the riblet structure and the streamwise flow recovery need to be clarified. Therefore, µ-PTV measurements are conducted at different spanwise locations to identify the variation of the wall-shear stress 3 mm downstream of the riblet structures. Furthermore, the velocity profiles

above and downstream of the actuated riblet surface are compared to explain the flow recovery effect.

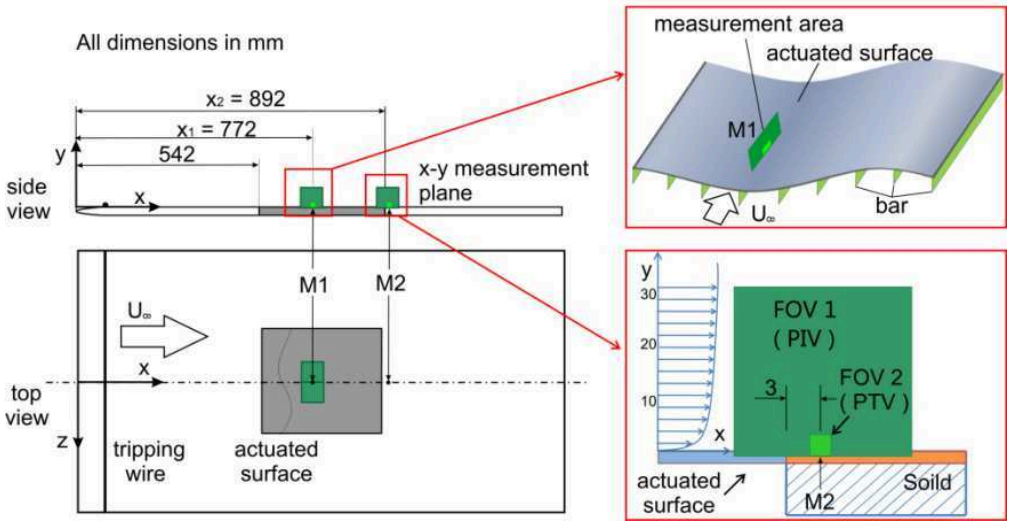

Figure 3.15: Schematic of the measurement station and corresponding measurement planes of PIV and µ-PTV.

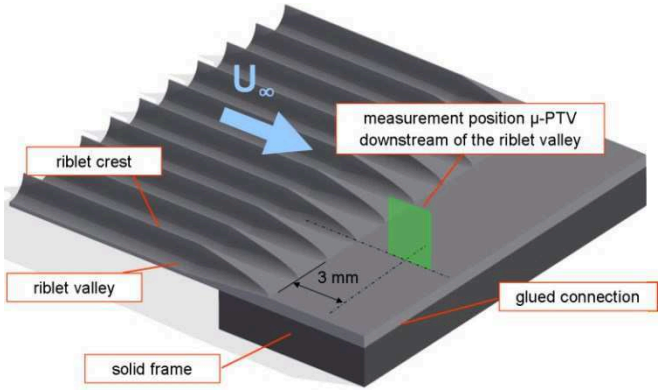

Figure 3.16: Sketch of the riblet structure and its transition to the smooth flat surface with the measurement position downstream of the riblet valley.

As shown in figure 3.16, the laser light sheet thickness is approximately 0.5 mm which only covers half of the riblet spacing. Therefore, the spanwise effect of the measurement has to be examined before the discussion of the drag reduction effect. The spanwise impact of the riblet structure on the wall-shear stress is measured by µ-PTV. The measurements are conducted in 11 planes with a step of 200µm and an overlap of 60% covering 2 riblet dimensions in the spanwise direction. Figure 3.17 shows the non-dimensional wall-shear stress distribution determined by µ-PTV measurements at different spanwise positions in the TBL downstream of the riblet surface. The standard deviation of the wall-shear stress on these 11 planes $\sigma =$ 0.9% shows that there is no significant spanwise variation of the wall-shear stress due to the riblet structure. In other words, due to the smooth transition from the riblet to the smooth surface, the near-wall velocity gradient at 3mm downstream of the riblets surface is not impacted by the upstream crest or trough geometry. Note that a likewise statement on the

independence of the spanwise location of the measurement cross section holds for the actuated riblet surface in Chapter 6.

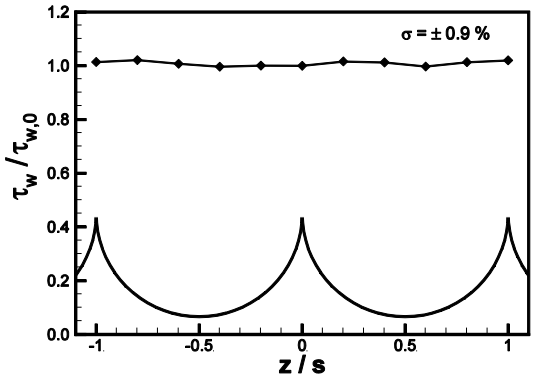

Figure 3.17: Spanwise distribution of the wall-shear stress measured by μ-PTV, $Re_\theta = 1200$.

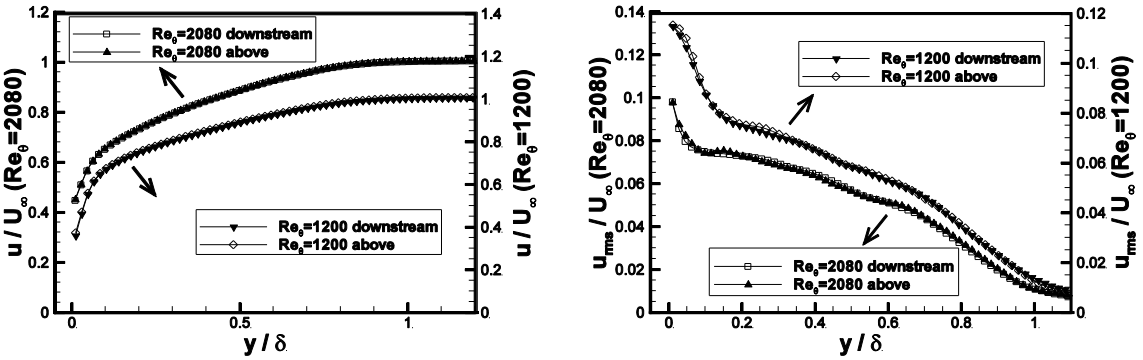

(a) (b)

Figure 3.18: Comparison of mean streamwise velocity profiles (a) and streamwise velocity fluctuations (b) 3mm downstream of the ribbed surface and above the riblets at both Reynolds numbers for an actuation amplitude of $A = 0.375$ mm, the wall-normal coordinate is normalized by the boundary layer thickness at the downstream position and the velocity by the freestream velocity U_∞.

The measurement cross section on the smooth surface is located 3 mm downstream of the riblet surface trailing edge corresponding to 75 wall units for $Re_\theta = 1200$ and 150 wall units for $Re_\theta = 2080$. Tamano and Itoh [80] reported a recovery length of about 80 mm or 2000 wall units in a spanwise traveling wave setup. Fukagata and Kasagi [103] showed that the drag reduction effect was lowered by approximately 10% at 75 wall units and 35% at 150 wall units downstream of the control region. A similar effect was shown by Gouder *et al.* [68] over an electromagnetically driven surface, the drag reduction effect was reduced by 25% at 240 wall units downstream of the oscillating surface.

Due to the difficulty of directly measuring the wall-shear stress over a riblet surface, the measurement of the mean velocity profiles and streamwise velocity fluctuations downstream and above the riblet surface are considered. Figure 3.18 shows the comparison of the mean velocity distribution and streamwise velocity fluctuation profiles 10 mm upstream and 3 mm downstream of the actuated riblet surface trailing edge at both Reynolds number $Re_\theta = 1200$

and 2080 for an actuation amplitude of A = 0.375 mm. The wall-normal distance is scaled by the boundary layer thickness δ at the downstream position and the streamwise velocity u and streamwise velocity fluctuation u'_{rms} are normalized by the freestream velocity U_∞. At both Reynolds numbers the upstream and downstream velocity and streamwise velocity fluctuation profiles agree well with respect to the different measurement positions. The match of the distributions measured upstream and downstream of the moving surface illustrates the small drag variation in the streamwise direction. Based on the aforementioned analysis, the flow recovery of the drag reduction effect is around 10 - 20% at 3 mm downstream of the flow-controlled domain. Even though this flow recovery is observed over the streamwise distance between the trailing edge of the moving wall and the measurement cross section downstream of the moving wall it can be stated that the small variation does not affect the overall impact of the wall movement on the near-wall flow.

4 Validation of PIV and μ-PTV

In this chapter, ZPG TBL flows are measured by using HWA, PIV and μ-PTV. The measurements examine the accuracy and capability of different measurement techniques in high-velocity gradient and complex TBL flows which are necessary for the friction drag reduction investigation. HWA is used to validate the μ-PTV and PIV measurements. It is found that the μ-PTV is able to resolve the TBL flow with a high-spatial resolution and the wall-shear stress can be efficiently estimated from the velocity gradient in the viscous sublayer. To further examine the accuracy and performance of the μ-PTV and PIV measurement techniques the streamwise turbulence intensity and wall-shear stress fluctuations are investigated for seven Reynolds numbers based on the momentum thickness in the range of $1009 \leq Re_\theta \leq 4070$ with a spatial resolution up to 0.06 - 0.23 wall units. The turbulent statistics evidence good agreement with DNS simulations and experimental results from the literature.

4.1 Experimental procedure

In TBL, the spatial resolution of the measurement techniques is one of the main limitations of understanding the characteristics of the high-velocity gradient and complex flows. According to Marusic *et al.* [104], the spatial averaging effect has clouded several important trends of near-wall turbulence including the streamwise turbulence intensity and the wall-shear stress fluctuation. The trivial reason is that the sensor cannot truly reflect the behavior of flow structures whose scales are smaller than the dimensions of sensors. The spatial resolution issue exists in all standard measurement techniques such as HWA, LDA, and PIV, etc. In turbulent flow, this effect is amplified by the fact that the smallest structures are time-dependent and extremely small down to the Kolmogorov microscale. Therefore, accurate measurement techniques are of great importance in the investigations of friction drag reduction and the corresponding mechanism in TBLs.

Among the current boundary layer measurement techniques, HWA is still the preferred tool due to its high spatial and temporal resolution. The diameter of the wire d is usually smaller than the smallest flow scale. However, the limit is defined by the length of the wire l, which is necessary to prevent end-conduction effects. Typical values are given by the ratio of $l / d \geq 200$. The spatial averaging effect along the spanwise direction of the wire introduces a filtering effect to the fluctuating flow. Various authors, e.g., Hutchins *et al.* [90] and Örlü and Alfredsson [105], have described this effect in detail and proposed correction methods based on different theories. Furthermore, efforts of manufacturing miniature hot-wire probes by

microelectromechanical systems (MEMS) have been made by Bailey *et al.* [106] and more recently Fan *et al.* [107]. Using the MEMS technique, the length of the hot-wire sensor is reduced to 30 µm by Hultmark *et al.* [108]. The MEMS-based nanoscale hot-wire sensor possesses a better spatial resolution and faster temporal response than conventional sensors. However, the results of them show that the spatial averaging effect ($l^+ = 45.5$ in wall units) seems to still exist in extremely high Reynolds number $Re_D = 2RU / \nu = 6.0 \times 10^6$ turbulent pipe flow.

In fully turbulent flows, however, it is very difficult to distinguish whether the experimental results reflect the true flow behavior or are somewhat biased by the spatial averaging effect. To capture TBL flows with respect to the fluctuating streamwise velocity and wall-shear stress, innovative measurement techniques with enhanced spatial resolution need to be developed.

According to Kähler *et al.* [109], the spatial resolution of µ-PTV is nearly not limited and it is a promising technique for wall-bounded flow investigations. Therefore, a combined PIV and µ-PTV setup is used to measure ZPG TBLs. The near-wall HWA is conducted to validate the PIV and µ- PTV results.

The PIV and µ-PTV measurement are conducted at two different positions, i.e., $x_1 = 895$ mm and $x_2 = 1400$ mm downstream of the leading edge of the flat plate. Under the same flow conditions, i.e., $U_\infty = 8$ m/s and $Re_\theta = 1200$, HWA measurements are conducted at x_1 for the validation of the PIV and µ-PTV measurement techniques. Moreover, measurements at $x_2 =$ 1400 mm are conducted at 7 freestream velocities, with the corresponding Reynolds numbers of $1009 \leq Re_\theta \leq 4070$. Additional flow parameters are listed in table 4.1.

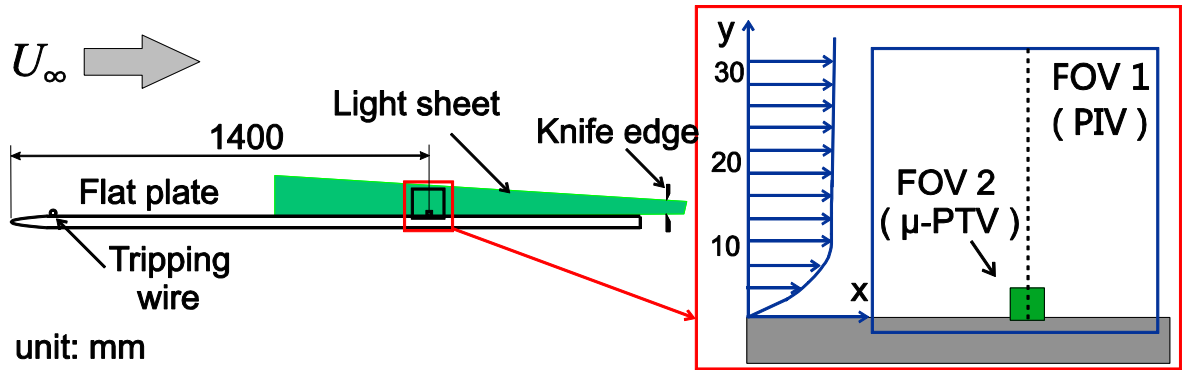

Figure 4.1: Schematic of the measurement setup and the corresponding PIV (FOV 1) and µ-PTV (FOV 2) measurement areas. The PIV flow statistics are extracted from the centerline of FOV 2.

Following De Silva *et al.* [110] and Knopp *et al.* [111], the measurement area is decomposed into two parts. Figure 4.1 shows a schematic drawing of the flat plate, the position of the measurement area and its decomposition into different fields of view. Using a large field of view (FOV 1), the whole boundary layer is measured by PIV. The near-wall region (FOV 2) is measured by µ-PTV allowing a high-spatial resolution to detect the small flow structures. The PIV measurements are conducted first, followed by the µ-PTV measurements. The flow statistics derived from the PIV measurements are extracted from the centerline of FOV 2.

Table 4.1: Flow parameters of the turbulent boundary layer at x_2 = 1400 mm; Re_θ momentum thickness based Reynolds number; U_∞ freestream velocity; Θ momentum thickness; u_τ friction velocity; ν / u_τ wall unit size in µm; H_{12} shape factor, i.e., the ratio of displacement and momentum thickness. The definitions of Re_θ, Θ, u_τ, and H_{12} can be found in Schlichting and Gersten [16].

Re_θ	U_∞ (m/s)	Θ (mm)	u_τ (m/s)	ν / u_τ (µm)	H_{12}
1009	3.96	3.965	0.183	84.0	1.473
1634	5.96	4.355	0.251	61.1	1.449
2130	7.93	4.126	0.326	47.1	1.435
2565	9.79	4.075	0.395	38.9	1.426
2978	11.78	3.92	0.460	33.4	1.419
3638	15.70	3.573	0.601	25.5	1.402
4070	18.65	3.389	0.709	21.7	1.396

According to the discussion in Chapter 3, the maximum theoretical sampling error based on $\bar{u}$ of the PIV data is less than 1% for a 95% confidence interval with the number of samples N = 2000. For the µ-PTV data, the maximum error is less than 0.5% in the near-wall region $y^+ < 8$. The maximum error of the streamwise turbulence intensity u'_{rms} is less than 3% for the PIV data in the near-wall region and less than 1.4% for the µ-PTV results.

As described in Chapter 3, the wall-shear stress and the friction velocity are determined using a least-square linear fitting method of the mean velocity gradient in the viscous sublayer. The present high-resolution µ-PTV measurement (5 µm) allows more than 50 data points at the lowest Reynolds number of Re_θ = 1009 and at least 10 data points at the highest Reynolds number of Re_θ = 4070 in the near-wall region $y^+ < 3.5$ such that a satisfying linear fit can be achieved. The standard linear fitting error of the gradient of the velocity distribution, i.e., du / dy in the region of $y^+ < 3.5$, is determined based on the method of Hutchins and Choi [88]. Table 4.2 shows the linear fitting error of the velocity gradient, i.e., the error of the wall-shear stress at 7 different Reynolds numbers. The maximum linear fitting error occurs at the higher Reynolds numbers but remains smaller than 1%.

Table 4.2: Linear fitting error of the skin friction at several Reynolds numbers.

Re_θ	1009	1634	2130	2565	2978	3638	4070
Error (%)	0.32	0.34	0.40	0.53	0.47	0.86	0.82

4.2 Systematic error correction of µ-PTV

Analytically, the measured flow velocity can be decomposed into the mean velocity $\bar{u}$ and the overall measured velocity fluctuation u'_{meas}, the latter of which can be regarded as the superposition of the real velocity fluctuation u'_{turb} and a fluctuation u'_{SE} due to systematic errors caused by the measurement system,

$$u_{meas} = \bar{u}_{meas} + u'_{meas} = \bar{u}_{meas} + u'_{turb} + u'_{SE}. \tag{4.1}$$

Consequently, the root-mean-square (RMS) value of the overall velocity fluctuation $u'_{meas,rms}$ can be expressed as

$$u'_{meas,rms} = \sqrt{\frac{1}{n}\sum_{i=1}^{n} u'^{2}_{meas}}$$

$$= \sqrt{\frac{1}{n}\sum_{i=1}^{n} u'^{2}_{turb} + \frac{1}{n}\sum_{i=1}^{n} 2u'_{turb}u'_{SE} + \frac{1}{n}\sum_{i=1}^{n} u'^{2}_{SE}}\,. \tag{4.2}$$

Thus, the RMS value of the turbulent velocity fluctuation $u'_{turb,rms}$ can be computed using

$$u'^{2}_{turb,rms} = u'^{2}_{meas,\,rms} - u'^{2}_{SE,\,rms} - \frac{1}{n}\sum_{i=1}^{n} 2u'_{turb}u'_{SE}. \tag{4.3}$$

Therefore, the real turbulent fluctuation of the flow and their RMS values can be determined with higher accuracy when the systematic error of the measurement system and its distribution in wall-normal direction are known.

In other words, the accuracy of the measurement of the turbulent flow statistics depends mainly on the uncertainty associated with several error sources. These error sources are discussed in chapter 3 leading to a low total uncertainty (max. 0.025%) of the local velocity measurement. However, due to the high-velocity gradient in the near-wall region and relatively small particle displacement, the measurements of turbulent statistics are easily biased. In the near-wall high-shear flow region, the main error sources can be divided into three parts, i.e., the uncertainty of particle tracking or window correlation algorithm, the systemic error due to the perspective viewing or parallax effect in the finite thick laser light sheet, and the spatial statistics error by binning measured vectors in the finite area in μ-PTV post-processing. Since the spatial resolution of the PIV measurement (6.6 - 25.6 wall units) is not sufficient enough to resolve the near-wall flow, the following discussion of the near-wall flow results mainly focuses on the μ-PTV data.

The first main error source is the uncertainty of particle tracking algorithm which depends on the particle image diameter, displacement, and density. In this study, the particle image diameter is approx. 15 pixels at a low particle concentration of 230 per image pair. According to Kähler *et al.* [112], with such a particle image diameter and low concentration the root-mean-square error of the displacement estimation of the particle tracking algorithm ΔX_{rms} where ΔX is particle displacement, is below 0.04 pixels. This leads to a streamwise velocity uncertainty $u'_{PTV,\,rms}$ of 0.007 - 0.032 m/s depending on the laser pulse offset.

The second part of the main error comes from the spatial statistics error u'_{SSE} by binning measured vectors over the measurement area intervals [113]. It occurs in the near-wall region

where the local velocity gradient is usually much higher than that off the wall. This effect introduces an additional velocity fluctuation component to the streamwise velocity. Durst *et al.* [99] discussed this problem analytically and applied a correction to the turbulence intensity of pipe flow data. The authors state that the root-mean-square of the spatial statistics error $u'_{\mathrm{SSE},rms}$ is proportional to the gradient of mean velocity.

The third part of the main error source is the perspective viewing error u'_{PVE} due to the finite thickness of the laser light sheet. Since in the μ-PTV measurement the measurement area is much smaller than the diameter of the optics, the axes of the camera and the long distance microscope are shifted to be above the center of the measurement area and are tilted at an angle of $\varphi = tan^{-1}(r/w_d)$, where r = 20 mm is the radius of the lens and w_d = 700 mm is the working distance, to avoid the obstruction of the flat plate. This results in an angle of $\varphi = 0.028$ rad, i.e., $\varphi = 1.6°$. Due to the finite thickness of the laser light sheet in the μ-PTV tracking method, a perspective viewing error occurs in the μ-PTV measurements. This error, which is also called the parallax effect, means that particle images that have the same y positions in the image space could have different positions above the wall in the world coordinate. An illustration of the parallax effect is shown in figure 4.2. Cierpka *et al.* [114] reviewed this effect and applied a correction using the mirrored particle images of the well-polished surface. Their results show that the mean velocity is not influenced by the perspective viewing error since the velocity gradient is constant in the viscous sublayer. However, regarding the higher order statistics, the perspective viewing error has a strong influence. It only occurs in the near-wall region (~ 90 μm). Since the present μ-PTV wall-normal measurement range 1.8 mm is much smaller than that of Cierpka *et al.* [114] , the region influenced by the mean velocity is approximately 10 μm (0.12 ~ 0.5 wall-units). The perspective viewing error u'_{PVE} of the mean velocity in the region above 10 μm can be neglected.

For the higher order turbulence statistics, however, the perspective viewing error u'_{PVE} caused by the parallax effect is not negligible. The root-mean-square of the fluctuating velocity (u'_{rms}) is a second-order variable which could be easily wrongly determined due to the systematic errors. Due to the parallax effect, the particle images with different positions in the real-world coordinate system could have the same y position in the image coordinate system depending on their axial positions in the laser light sheet. By using geometric optics theory [115], the magnitude of the perspective error can be calculated showing small variations in the measurement volume. Unlike in the investigation of Cierpka *et al.* [114], the perspective angle varies slightly between 1.6° at the bottom and 1.47° at the top of the present measurement area. In the small region of the viscous sublayer at the bottom of FOV 2, the perspective angle can be regarded constant of 1.6°. Therefore, in the near-wall region $y^+ < 5$, also the perspective viewing error u'_{PVE} can be considered constant. Similar to the spatial statistics error in the finite measurement area, the parallax effect of μ-PTV measurements leads to the systematic error $u'_{PVE,rms}$ of the fluctuating velocity (u'_{rms}) which is proportional to the velocity gradient.

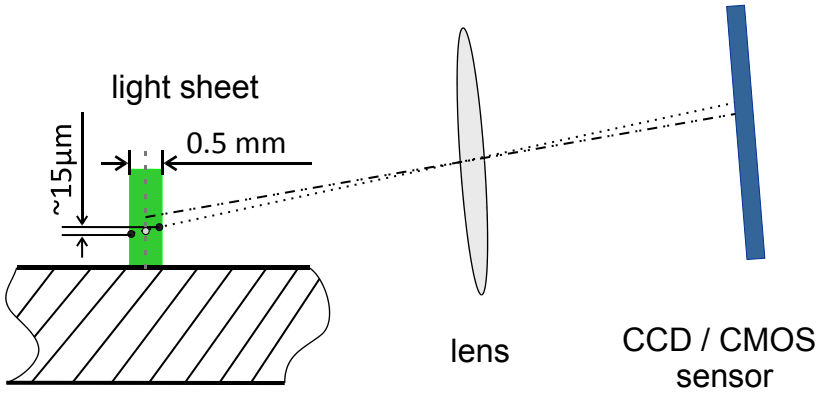

Figure 4.2: Parallax effect of the μ-PTV measurement.

A constant systematic error $u'_{PTV,\,rms}$ by the particle tracking algorithm, an error by the parallax effect $u'_{PVE,rms}$ and another error by the spatial statistics $u'_{SSE,rms}$ are introduced to the measured fluctuating velocity $u'_{meas,rms}$. Errors by the spatial average effect and the parallax effect depend on the velocity gradient such that in the region with constant velocity gradient the error can be treated constant. In the following, the three main measurement errors are integrated into the total systematic error $u'_{SE,rms}(\frac{du}{dy})$ as a function of velocity gradient.

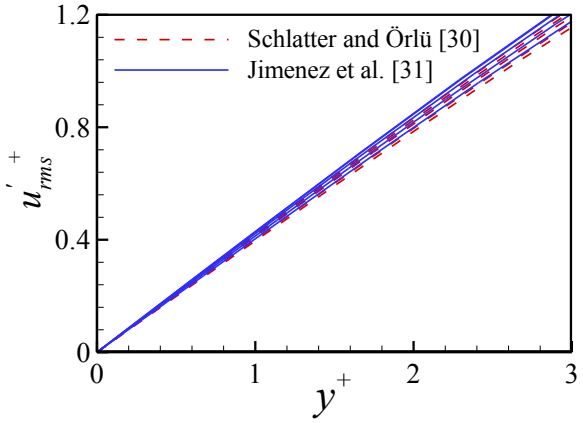

Figure 4.3: Linear behavior of the velocity fluctuation in the very near-wall region, DNS results from Schlatter and Örlü [116], dashed line, $677 \leq Re_\theta \leq 4000$; Jimenez *et al.* [117], solid line, $1100 \leq Re_\theta \leq 6500$.

Since the systematic error is mainly caused by the uncertainty of the positions of the tracked vectors from the measurement and the final spatial statistics, the true turbulent fluctuation u'_{turb} in equation (4.3) has no correlation or just a weak correlation with the systematic error u'_{SE} , which leads to

$$\sum_{i=1}^{n} 2u'_{turb}u'_{SE} \approx 0.$$

Hence, the turbulent fluctuation which is a function of the wall distance y can be expressed by

$$u'^{2}_{turb,rms}(y^+) \approx u'^{2}_{\mathrm{meas},\,rms}(y^+) \; - \; u'^{2}_{SE,\,rms}\left(\frac{du}{dy}\right). \tag{4.4}$$

That is, although the distribution of the experimental velocity fluctuation $u'_{meas,\,rms}(y^+)$ is known, the real turbulent fluctuation can only be determined if the distribution of the systematic error $u'_{SE,\,rms}(\frac{du}{dy})$ is available. Therefore, an additional relation of the velocity fluctuation has to be introduced to equation (4.4) to obtain the real turbulent fluctuation $u'_{turb,rms}(y^+)$. The comparison of the DNS databases by Schlatter and Örlü [116] and Jimenez *et al.* [117] in figure 4.3 shows a linear distribution of the velocity fluctuations in the very near-wall region $y^+ < 2$ over a large Reynolds number range $677 \leq Re_\theta \leq 6500$. Such a linear distribution was also exploited by Alfredsson and Örlü [96] to examine hot-wire data of wall-bounded turbulent flow. Based on this linear relationship between the velocity fluctuation and the wall-normal distance, $u'_{turb,rms}$ can be expressed as $u'_{turb,rms}(y^+) = ky^+$ for $y^+ < 2$ where k is a constant slope of $u'_{turb,rms}$ and y^+. Moreover, since the velocity gradient $\frac{du}{dy}$ is constant in this region and the systematic error only depends on the velocity gradient, $u'^{2}_{SE,\,rms}$ can be also considered as constant. Thus, from equation (4.4) we obtain

$$u'^{2}_{meas,\,rms}(y^+) = (ky^+)^2 + u'^{2}_{SE,\,rms}\,. \tag{3.5}$$

The intersection $u'^{2}_{SE,\,rms}$ of equation (4.5) can be determined by a least-square linear fitting of $u'^{2}_{meas,\,rms}$ and y^{+2} in the very near-wall region $y^+ < 2$. Thus, the systematic error of the velocity fluctuation $u'_{SE,\,rms}$ can be obtained in the viscous sublayer. Figure 4.4 shows the comparison of the experimentally determined streamwise turbulence intensity at $Re_\theta = 2129$ and the DNS results by Schlatter and Örlü [116] at $Re_\theta = 2000$. The uncorrected data show an apparent bias error at $y^+ < 2$. With the increase of the wall-normal distance, the influence of the systematic error decreases rapidly. For a wall-normal distance $y^+ \geq 2$, the experimental data both with and without correction deviate less than 0.5% from the DNS data since the measured streamwise turbulence intensity $u'^{2}_{meas,\,rms}(y^+)$ is dominated by the larger real flow fluctuation $u'^{2}_{turb,rms}$. On the one hand, the magnitude of the turbulence component by the turbulent flow is increased at higher wall-normal distances and on the other hand, the systematic error is decreased due to the decrease of the mean velocity gradient. In the region $y^+ \geq 2$, the magnitude of the real flow fluctuation is much larger than the systematic error and dominates the experimental results. Thus, the systematic error only shows a significant influence in the very near-wall region of $y^+ < 2$.

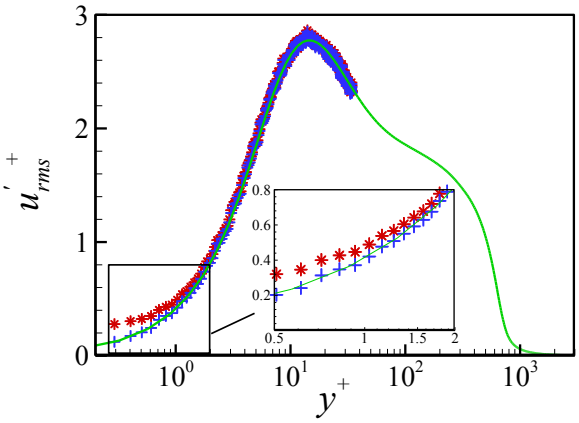

Figure 4.4: Present experimental results of $Re_\theta = 2129$, asterisk (✳): without correction; cross (+): with correction; solid line: DNS data by Schlatter and Örlü [116] at $Re_\theta = 2000$.

4.3 Results and discussion

The results of the HWA, PIV, and μ-PTV measurements are discussed in the following. First, the results at the measurement position x_1 from all three techniques are compared to validate the measurement quality. Then, to examine the accuracy and performance of PIV and μ-PTV in capturing TBL flows, the results at the measurement position x_2 are discussed. The results, on the one hand, show that the PIV and μ-PTV are able to measure TBL flows with a high accuracy. On the other hand, the results at x_2 show the streamwise turbulence intensity and wall-shear stress fluctuation to grow at increasing Reynolds numbers.

4.3.1 Validation of PIV and μ-PTV with HWA

Turbulent statistics

To validate the PIV and μ-PTV measurements, the TBL statistics measured by HWA, PIV, and μ-PTV in conjunction with the DNS simulation by Schlatter and Örlü [116] are plotted in the inner scaling in figure 4.5. Note that the Reynolds number for the DNS is $Re_\theta = 1000$ and for the measured results it is $Re_\theta = 1200$. In the near-wall region, due to the high-velocity gradient the PIV data below $y = 1$ mm are biased. Thus, the first 4 measurement data points above the wall are discarded. The mean streamwise velocity distributions plotted in figure 4.5 (a) show that the μ-PTV and the hot-wire data match very well in the buffer layer ($5 < y^+ < 30$). The μ-PTV results in the viscous sublayer overlap with the DNS simulation which indicates that the mean flow is well resolved by the measurement technique. In the logarithmic region ($30 < y^+ < 150$) the variance between the PIV and hot-wire data is less than 1%. This shows that both measurements have a good agreement. The uncorrected streamwise turbulence intensity is plotted in figure 4.5 (b). It is noticed that the uncorrected u'^{+}_{rms} from μ-PTV shows a much higher value than the DNS simulation in the very near-wall region of $y^+ < 2$. It is mainly due to the systemic error of the μ-PTV measurement technique which has been discussed in section 4.2. In a higher wall-normal position, the μ-PTV and hot-wire data match with the DNS results indicating the higher order turbulent statistics, i.e. streamwise turbulence intensity u'^{+}_{rms} can captured accurately by the μ-PTV.

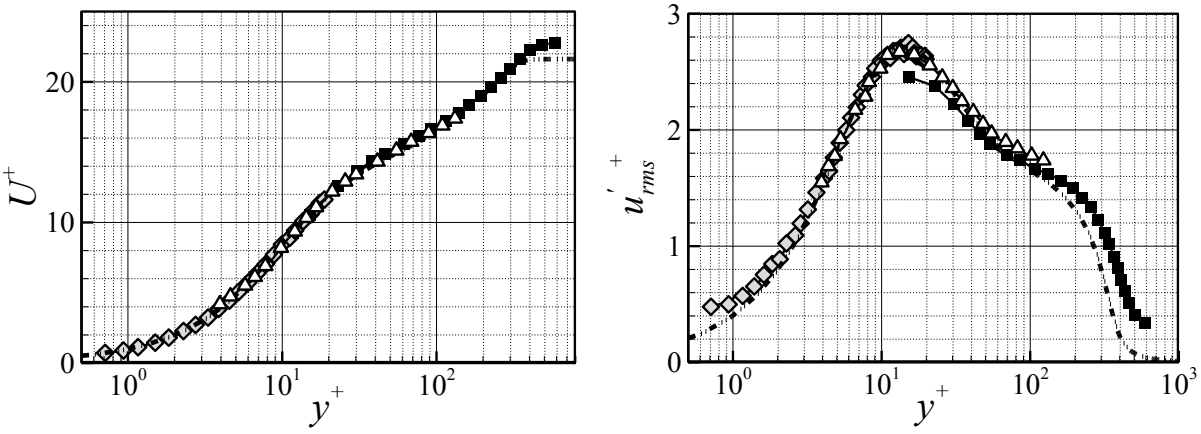

(a) (b)

Figure 4.5: Comparisons of the experimental data from the HWA, PIV, and μ-PTV measurements at Re_θ = 1200 and the DNS simulation by Schlatter and Örlü [116] at Re_θ = 1000. (a) Mean streamwise velocity U^+ in the inner scaling; delta (Δ): HWA; diamond (◊): μ-PTV without correction; square (■): PIV; dash-dotted line: DNS. (b) Streamwise turbulence intensity u'^+_{rms} in the inner scaling, symbols are the same as figure 4.5 (a).

Wall-shear stress

For the canonical ZPG TBLs, the wall-shear stress can be estimated either from the linear relation of the streamwise velocity and the wall-normal distance in the viscous sublayer or from a fitting to a composite velocity distribution, e.g. the log-law, Spalding and Musker profiles [118]. After applying the diagnostic plot of the hot-wire data, only a few data points exist in the viscous sublayer. These results are not enough to estimate the wall-shear stress accurately. According Kendall and Koochesfahani [118], the error of the friction velocity can be less than 0.5% using the fitting estimation with Musker profile. The wall-shear stress of 0.157 Pa is estimated from the HWA data at Re_θ = 1200. However, this method is only limited to the canonical ZPG TBLs and cannot be used to investigate the wall-shear stress distributions in passive/active controlled TBLs. In the μ-PTV measurements, the spatial resolution in the wall-normal direction is 5 μm. It allows more than 25 data points in the linear region of $y^+ < 3.5$ at Re_θ = 1200 and ensures a favorable linear fitting to determine the wall-shear stress. Here, the wall-shear stresses obtained from the μ-PTV is 0.155 Pa which shows a variance of 1.3% from the one estimated by using the Musker profile.

4.3.2 TBL characteristics at different Re_θ

Integral and global quantities

The integral and global quantities such as the shape factor H_{12}, i.e., the ratio of displacement and momentum thickness, and the friction coefficient c_f are standard criteria to quantify TBL flows. The importance of the shape factor as one of the criteria to judge the equilibrium state of the flow has been shown, e.g., by Chauhan *et al.* [119], Schlatter and Örlü [116], and Örlü and Schlatter [120]. The values obtained from the present experiments listed in table 4.1 are shown in figure 4.6 (a) together with the integration of the composite profile by Chauhan *et al.* [119] with a tolerance limit of 1%. Most of the experimental data points are located in the given tolerance interval and agree well with the analytical value by Chauhan *et al.* [119]. The

friction coefficient c_f is plotted in figure 4.6 (b) together with the widely-known Coles-Fernholz friction relation [121] and its tolerance limit of 5%. The current results deviate less than 2% from the empirical formulation at higher Reynolds numbers. Even for the worst case at the lowest Reynolds number $Re_\theta = 1009$ the deviation between the experimental results and the empirical formulation is less than 5%. Thus, the integral and global quantities show the high measurement quality of the current setup.

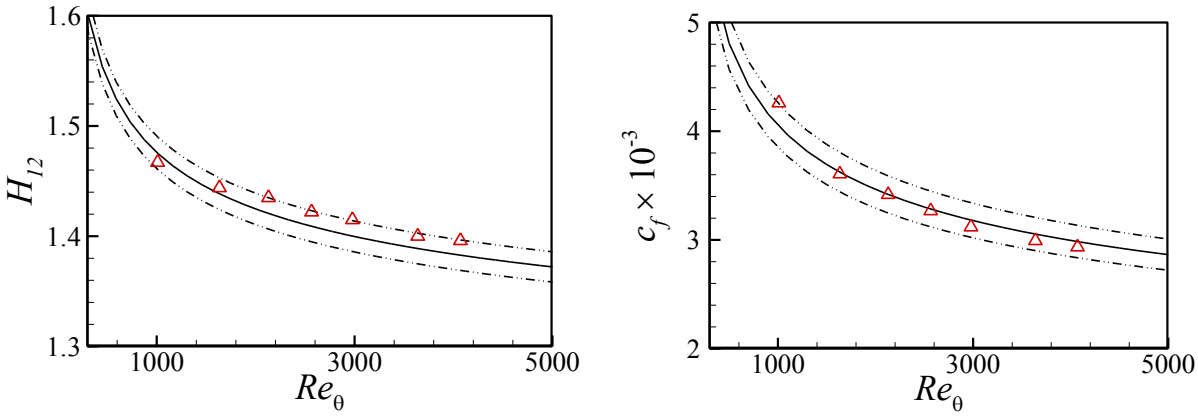

(a) (b)

Figure 4.6: (a) Shape factor H_{12} as a function of the momentum thickness based Reynolds number Re_θ. The solid line indicates the integration of composite profile of Chauhan *et al.* [119], the dash-dotted lines represent a ±1% tolerance limit. (b) Friction coefficient c_f as a function of the momentum thickness based Reynolds number Re_θ. The solid line indicates the Coles-Fernholz friction relation [121] with $\kappa = 0.383$ and $C = 4.147$, the dash-dotted lines represent a ±5% tolerance limit.

Streamwise velocity and turbulence intensity In the following, the boundary layer flow is illustrated in inner wall units. Figure 4.7 (a) and figure 4.8 (a) show a comparison of the measured streamwise mean velocity and turbulence intensity profiles as a function of the normalized wall-distance with the DNS results at $Re_\theta = 2000$ by Schlatter and Örlü [116]. The linear region in the viscous sublayer ($y^+ < 5$) and the distribution in the buffer layer $5 < y^+ < 30$ are captured by the μ-PTV data in the smaller FOV. As expected, a biased error of the PIV measurement is observed in the near-wall region $y < 1$ mm, i.e., y^+ less than 12 to 46 wall units, where a high-velocity gradient exists. This error caused by the window correlation of the velocity gradient flow has been analyzed by Kähler *et al.* [112] with synthetic particle images. The results indicate that the error depends on the interrogation window size and the mean velocity gradient. The 4 data points of the PIV measurement closest to the wall at $y < 1$ mm, i.e., y^+ less than 12 to 46 wall units, are discarded and supplemented by μ-PTV data. The normalized mean streamwise velocity distribution shows a convincing agreement with the universal law of the wall indicating a high accuracy of the wall-shear stress measurement method. Moreover, the comparison of the experimental results at $Re_\theta = 2130$ and the DNS data at $Re_\theta = 2000$ shows a good correspondence. The experimental results are overlapping with the DNS data especially in the near-wall region and the logarithmic region. Since the Reynolds number of the experiment $Re_\theta = 2130$ is higher than that of the DNS, a slight overshoot of 1.8% of u^+ is noticed.

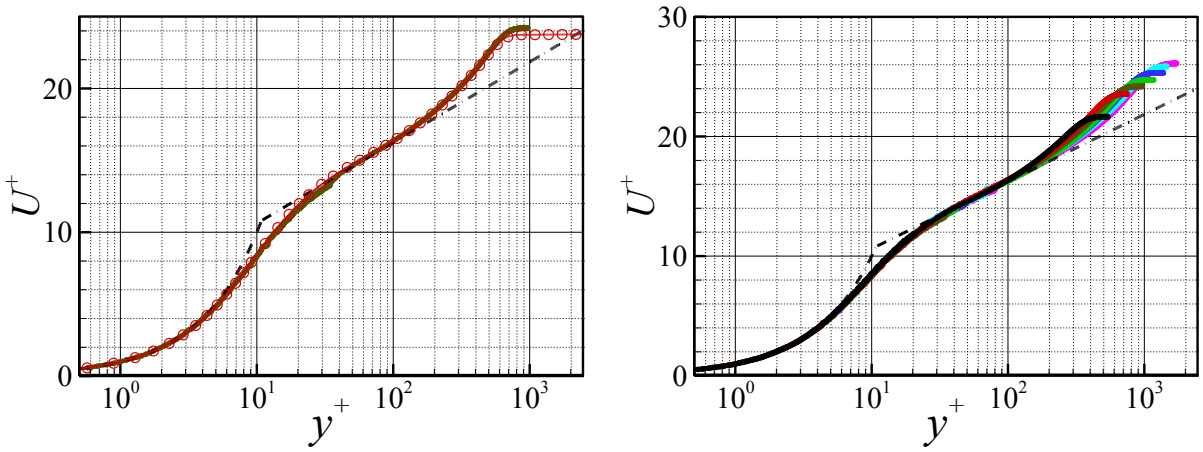

(a) (b)

Figure 4.7: (a) Mean streamwise velocity u^+ in inner scaling; solid line: present PIV and µ-PTV measurements at $Re_\theta = 2130$; circles: DNS simulation by Schlatter and Örlü [116] at $Re_\theta = 2000$. (b) Measured profiles of the mean streamwise velocity at $Re_\theta = 1009$ (black), $Re_\theta = 1634$ (red), $Re_\theta = 2130$ (dark green), $Re_\theta = 2565$ (green), $Re_\theta = 2978$ (blue), $Re_\theta = 3638$ (light blue), and $Re_\theta = 4070$ (pink). Dash-dotted line, law of the wall, $u^+ = y^+$ and $u^+ = 1/\kappa \ln y^+ + B$, with $\kappa = 0.41$ and $B = 5$.

The spanwise spatial averaging effect of the measurement techniques such as HWA is one of the major systematic errors that can cause misleading experimental results and conclusions. Unlike HWA whose sensor size is usually constant µ-PTV tracks individual particles and thus has a much higher spatial resolution. It is discussed in detail by Kähler *et al.* [109] that µ-PTV evaluation methods allow to increase the spatial resolution to the subpixel limit for flow field statistics and do not show bias errors which are typically generated by window correlation.

In figure 4.8 (a) the streamwise turbulence intensity based on the DNS data from Schlatter and Örlü [116] at $Re_\theta = 2000$ and the experimental results at $Re_\theta = 2130$ are juxtaposed. It is evident that the streamwise turbulence intensities of the µ-PTV and DNS data are overlapping in the near-wall region. Both of the µ-PTV and DNS show that the streamwise turbulence intensity $u'_{rms}{}^+$ reaches a peak close to the wall at approx. $y^+ = 14$. This matches the value $y^+ \approx 15 \pm 1$ reported in the literature. Note that in figure 4.8 (a) the interrogation window size of the PIV measurement is about 12 × 12 wall units at $Re_\theta = 2130$ which causes a spatial turbulence intensity attenuation of 5 % less than the DNS data in the log region $35 < y^+ < 140$. This effect also exists for the other Reynolds numbers. For more details on this filtering effect of PIV, readers are referred to Atkinson *et al.* [122]. Figure 4.8 (b) shows the distributions of the streamwise turbulence intensity in the Reynolds number range $1009 \leq Re_\theta \leq 4070$. The $u'_{rms}{}^+$ profiles indicate that the peak of the streamwise turbulence intensity grows at higher Reynolds numbers. In the inner region, the streamwise turbulence intensity does not follow the universal scaling law.

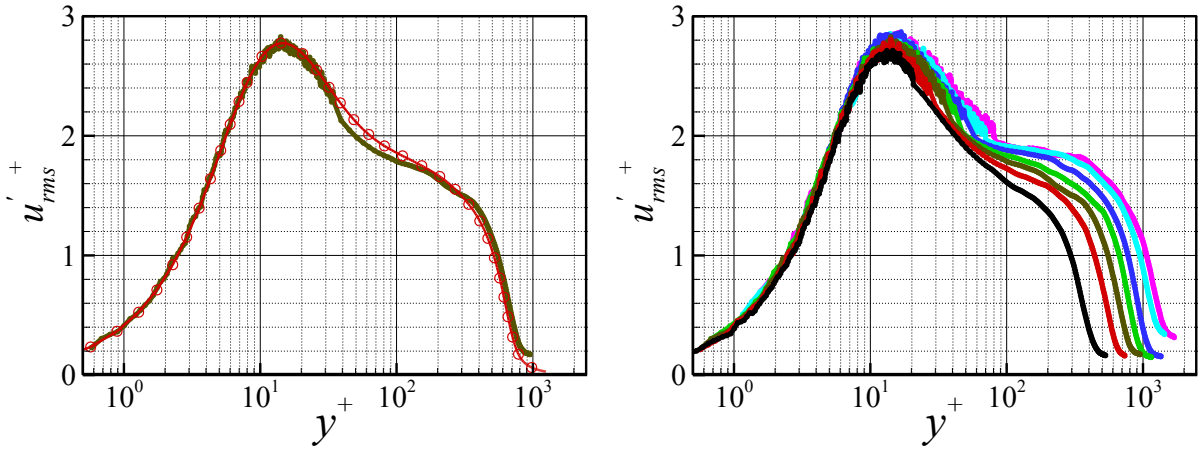

Figure 4.8: (a) Streamwise turbulence intensity u'^{+}_{rms} in inner scaling; solid line: present PIV and μ-PTV measurement at $Re_\theta = 2130$; circles: DNS simulation by Schlatter and Örlü [116] $Re_\theta = 2000$. (b) Measured profiles of the streamwise turbulence intensity with systematic correction at $Re_\theta = 1009$ (black), $Re_\theta = 1634$ (red), $Re_\theta = 2130$ (dark green), $Re_\theta = 2565$ (green), $Re_\theta = 2978$ (blue), $Re_\theta = 3638$ (light blue), and $Re_\theta = 4070$ (pink).

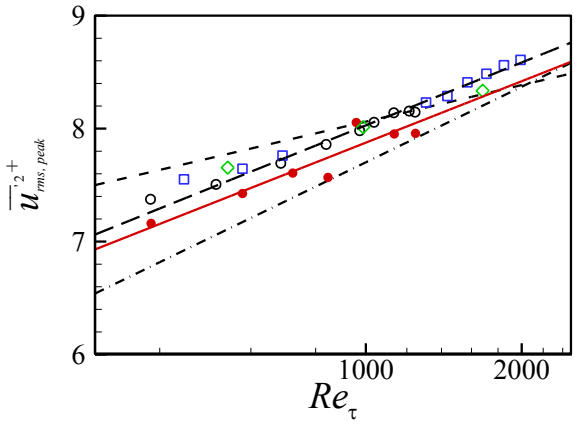

Figure 4.9: Peak value of the inner scaling streamwise turbulence intensity as a function of the Reynolds number, circles (○): DNS results by Schlatter and Örlü [116]; squares (□): DNS results by Jimenez *et al.* [117]; diamonds (◇): LDA measurements by De Graaff and Eaton [123]; red bullet points (●): present μ-PTV results; dashed line: semi-empirical prediction $\overline{u'^2}^{+}_{max} = 1.036 + 0.965 \ln Re_\tau$ by Marusic and Kunkel [124]; dash-dotted line: $\overline{u'^2}^{+}_{max} = 4.837 + 1.075 \log_{10} Re_\tau$ by Hutchins *et al.* [90]; long-dashed line: $\overline{u'^2}^{+}_{max} = 2.482 + 0.803 \ln Re_\tau$ prediction from the DNS data by Schlatter and Örlü [116] and Jimenez *et al.* [117]; solid line: $\overline{u'^2}^{+}_{max} = 2.377 + 0.798 \ln Re_\tau$ prediction from present μ-PTV results.

The attached eddy hypothesis suggests that the streamwise turbulence intensity does not follow the wall scaling [104]. This behavior of the streamwise turbulence intensity has been discussed, e.g., by Townsend [125] and Marusic and Kunkel [124]. Figure 4.9 shows the comparison of the peak value of the inner scaling streamwise turbulence intensity as a function of the Reynolds number based on the friction velocity Re_τ. The peak value of the turbulent intensity is determined by a 4th-order polynomial fitting of the data points in 8 <

y^+< 30. The present results are located between the semi-empirical prediction by Marusic and Kunkel [124] and Hutchins *et al.* [90]. They show good agreement with the DNS simulations by Jimenez *et al.* [117] and Schlatter and Örlü [116] as well as LDA measurements by De Graaff and Eaton [123]. Preliminary semi-empirical predictions based on the present results and the DNS simulations are also plotted in figure 4.9. The experimental prediction indicates a slightly lower value by 2% than the DNS prediction. This might due to the difference of the inflow boundary conditions and tripping effects between the experimental setup and DNS. To achieve a more accurate prediction of the turbulent intensity peak, additional investigations need to be performed at higher Reynolds numbers.

Wall-shear stress fluctuation

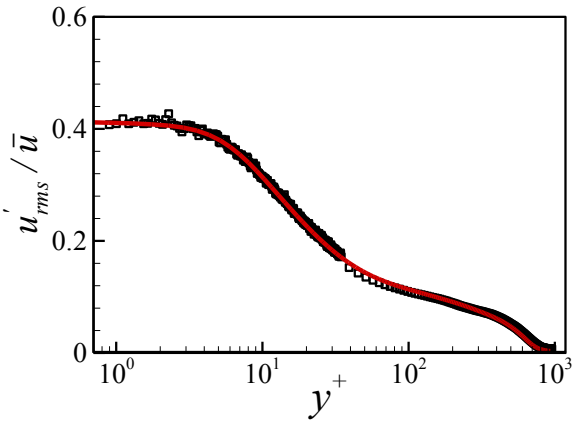

Figure 4.10: Distribution of the normalized streamwise turbulence intensity $u'_{rms}/\bar{u}$ scaled by local mean velocity in inner scaling; solid line: DNS, Re_θ = 2000 [116]; squares: present measurements, Re_θ = 2130.

Different measurement methods, see e.g., Alfredsson *et al.* [126], Große and Schröder [127] and Österlund [128] have been used to determine the fluctuating wall-shear stress distribution. The only direct measurement of the wall-shear stress fluctuation is to measure the instantaneous force in every point of the wall. However, this is hardly feasible with current measurement techniques. According to Alfredsson *et al.* [126], a simple expression of the normalized wall-shear stress fluctuation can be written as

$$\tau^+_{w,rms} = \frac{\tau'_{w,rms}}{\overline{\tau_w}} \cong \lim_{y\to 0} \frac{u'_{rms}}{\bar{u}}\,, \tag{4.6}$$

with the mean and fluctuating streamwise velocity $\bar{u}$ and u'_{rms}.

The distributions of $u'_{rms}/\bar{u}$ of the DNS data at Re_θ = 2000 and the experimental results at Re_θ = 2130 are plotted as a function of the normalized wall distance y^+ in figure 4.10. Obviously, the wall-shear stress fluctuation $u'_{rms}/\bar{u}$ has the maximum value on the wall and is nearly constant in a small near-wall region. It decreases at increasing wall distance. According to the DNS data by Schlatter and Örlü [116], the data are underestimated by 8% at y^+ = 5 and 1.5% at y^+ = 2 when equation (4.6) is applied to determine the wall-shear stress fluctuation. This means that equation (4.6) of the normalized wall-shear stress can be only used in the near-wall region, i.e., for $y^+ \leq 2$. Therefore, to minimize the underestimation error

by equation (4.6) and decrease the uncertainty of the experimental data, the wall-shear stress fluctuation is determined by the mean value of $u'_{rms}/\bar{u}$ only in the region $y^+ \leq 2$

$$\tau^+_{w,rms} = \frac{\tau'_{w,rms}}{\overline{\tau_w}} \cong \overline{\left(\frac{u'_{rms}}{\bar{u}}\right)}\Big|_{y^+\leq 2} . \tag{4.7}$$

The underestimation error of the wall-shear stress fluctuation by equation (4.7) examined by the DNS data is 0.67% at a standard deviation of 0.6 %.

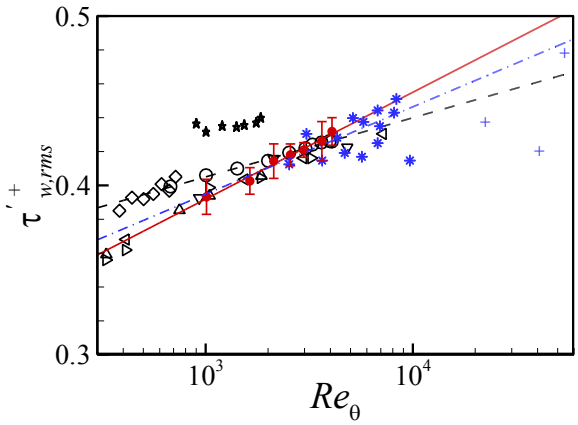

Figure 4.11: Wall-shear stress fluctuation distribution as a function of the momentum thickness based Reynolds number Re_θ. Turbulent boundary layer DNS results: diamond (◇), Komminaho and Skote [129]; pentacle (☆), Wu and Moin [130]; circle (○), Schlatter and Örlü [116]; Channel flow DNS results: delta (△), Iwamoto *et al.* [131]; gradient (▽), Hu *et al.* [132]; right triangle (▷), Abe *et al.* [133]; left triangle (◁), Del Alamo *et al.* [134]; Turbulent boundary layer results: cross (+), PIV results by De Silva *et al.* [110]; asterisk (✳), Österlund [128] hot-wire results corrected by Örlü and Schlatter [135]; red bullet point (●), present μ-PTV results, error bar indicates the standard deviation of u'_{rms}/U in the region of $y^+ < 2$; dashed line, semi-empirical prediction $\tau^+_{w,rms} = 0.298 + 0.018 \ln Re_\tau = 0.3 + 0.0152 \ln Re_\theta$ for $Re_\tau = 1.13 Re_\theta^{0.843}$ by Schlatter and Örlü [116]; solid line, prediction based on present results $\tau^+_{w,rms} = 0.2037 + 0.0274 \ln Re_\theta$; dash-dotted line, prediction based on present results and the corrected data by Örlü and Schlatter [135] $\tau^+_{w,rms} = 0.2401 + 0.0224 \ln Re_\theta$.

A comparison of the wall-shear stress fluctuation as a function of Re_θ is plotted in Figure 4.11. The wall-shear stress fluctuations from various numerical simulations and experiments of internal and external flows in the literature are presented in the Reynolds number range $300 \leq Re_\theta \leq 54500$. The wall-shear stress fluctuation value of 0.4 was reported by Alfredsson *et al.* [126], however, more recent investigations by Hutchins *et al.* [90], Örlü and Schlatter [120], and Smits [136] suggest a slight Reynolds number dependence of the wall-shear stress fluctuation. Örlü and Schlatter [135] attributed this effect to the growing influence of the large-scale turbulence structures and their impact on the wall-shear stress. By assessing various numerical simulation data of turbulent boundary layers, Schlatter and Örlü [116] obtained an empirical expression of the wall-shear stress fluctuation $\tau^+_{w,rms} = 0.298 + 0.018 \ln Re_\tau$ showing the wall-shear stress fluctuation to increase at growing Reynolds number. However, due to the difficulty in measuring the wall-shear stress fluctuation

accurately, only a few experimental investigations reported this effect. For turbulent pipe flows, Große and Schröder [127] showed a decrease of $\tau_{w,rms}^{+}$ from 0.39 to 0.33 when Re_τ was increased from 630 to 1150. The wall-shear stress was determined by integrating the motion of micro-pillar wall-shear stress sensors (MPS^3) whose lengths were 3 to 10 wall units which may cause the decrease of $\tau_{w,rms}^{+}$ due to the integration on the sensor length. Fischer *et al.* [137] found by LDA measurements that $\tau_{w,rms}^{+}$ increases from 0.33 to 0.38 when Re_τ grows from 118 to 481 in channel flows. The effect was confirmed by Keirsbulck *et al.* [138] in a similar Re_τ range in channel flows. Colella and Keith [139] reported that $\tau_{w,rms}^{+}$ decreases from 0.36 to 0.25 when Re_θ increases from 2160 to 3150 in boundary layer flows. This decrease of the wall-shear stress fluctuation probably results from the spatial average effect by the flush-mounted hot-film sensor. Hot-wire results by Österlund [128] showed that $\tau_{w,rms}^{+}$ spreads from 0.28 to 0.41 in the Reynolds number range of $2000 < Re_\theta < 10000$. With an especially designed wall-hot-wire ($L^+ = 6.2$) Österlund [128] concluded that $\tau_{w,rms}^{+}$ is close to 0.41 for $Re_\theta = 10000$. More recently, PIV data by De Silva *et al.* [110] yielded a higher value $\tau_{w,rms}^{+} = 0.48$ at a very large Reynolds number $Re_\theta = 54000$. In the present investigation, the wall-shear stress fluctuation varies from 0.39 to 0.43 in the Reynolds number range $1009 \leq Re_\theta \leq 4070$. Consequently, the results confirmed the DNS findings by Schlatter and Örlü [116] and Örlü and Schlatter [135]. The semi-empirical prediction $\tau_{w,rms}^{+} = 0.2037 + 0.0274 \ln Re_\theta$ based on the present measurements and that based on the DNS prediction of $\tau_{w,rms}^{+} = 0.298 + 0.018 \ln Re_\tau = 0.3 + 0.0152 \ln Re_\theta$ for $Re_\tau = 1.13 Re_\theta^{0.843}$ by Schlatter and Örlü [116] are shown in Figure10. Note that the relation $Re_\tau = 1.13 Re_\theta^{0.843}$ is from a best fit of channel and TBL flows while the relation $\tau_{w,rms}^{+} = 0.298 + 0.018 \ln Re_\tau$ is derived from TBL DNS data. Schlatter and Örlü [116] further stated that the relation for Re_τ in terms of Re_θ provides a good fit to the data and can be used to convert between the two Reynolds numbers. For comparison, a similar prediction $\tau_{w,rms}^{+} = 0.2401 + 0.0224 \ln Re_\theta$ based on the experimental results, i.e., the corrected data of Österlund [128] by Örlü and Schlatter [135] and present measurements, is plotted in Figure 4.11. At increasing Reynolds number, the present predictions based on experimental results shows higher values than that by Schlatter and Örlü [116]. However, although the PIV measurements by De Silva *et al.* [110] show a better agreement with Schlatter and Örlü [116]'s prediction at higher Reynolds numbers, it still can be assumed that the results for $\tau_{w,rms}^{+}$ are likely to be underestimated. There are two reasons for this. On the one hand, unlike μ-PTV, PIV is a volume based measurement technique. The wall-shear stress fluctuation is averaged over the relatively large interrogation window size of 5 × 5 wall units and 11 wall units in the spanwise direction at $Re_\theta = 22\,400$ and 14 × 14 wall units and 30 wall units in the spanwise direction at $Re_\theta = 54\,000$. This averaging effect leads to an underestimation of $u'_{rms}{}^{+}$ and $\tau_{w,rms}^{+}$. On the other hand, the PIV data may not be close enough to the wall to determine the wall-shear stress fluctuation by equation (4.6) which expects the wall-normal distance to be $y^+ \leq 2$. The flow in the interrogation window whose upper bound is at $y^+ = 14$ at $Re_\theta = 54\,000$ will result in a relatively smaller value of $u'_{rms}/\bar{u}$.

4.4 Summary

In this chapter, high-spatial resolution μ-PTV, standard 2C-2D PIV, and near-wall hot-wire measurements are conducted in TBLs to validate the measurement techniques. The streamwise velocity and fluctuation are compared to examine the accuracy and performance of μ-PTV and PIV. Furthermore, μ-PTV and PIV are performed at Reynolds numbers of $1009 \leq Re_\theta \leq 4070$ to determine the impact of the Reynolds number on the distributions of the streamwise turbulence intensity and the wall-shear stress fluctuation which is hardly be captured by standard measurement techniques. The present measurements are in good agreement with experimental results and DNS data from the literature. On the one hand, the results show that the μ-PTV technique enables a near-wall high-spatial resolution of TBLs up to 5 μm such that the near-wall velocity gradient which determines the wall-shear stress is accurately captured. It overcomes the common spatial resolution issues of other measurement techniques and provides a suitable tool for investigation of the passive/active drag reduction. On the other hand, by introducing a simple model in which linearity between the streamwise turbulence intensity and the wall distance in the near-wall region is assumed, the spatial statistics error by the parallax effect over the measurement volume is corrected. The streamwise turbulence intensity and wall-shear stress fluctuation results confirm the Reynolds number impact discussed by Örlü and Alfredsson [140] and Örlü and Schlatter [135]. This enriches the database of the research of wall-bounded turbulent flows.

5 Passive friction drag reduction

In this chapter, the friction drag reduction effect of the rolled semi-circular riblet structure in TBL flows is investigated by PIV and μ-PTV. The measurements are performed above and directly downstream of the riblet-structured surface at various flow conditions, i.e., ZPG, APG, and periodical unsteady inflows. Results downstream of the riblet-structured surface in ZPG TBLs are firstly analyzed. The measurements at 3 mm downstream of the riblet-structured surface indicate a local drag reduction of 4.7% at Re_θ = 1200 with the riblet spacing of s^+ = 24 and a local drag reduction of 0.7% at Re_θ = 2080 with s^+ = 45. Then, the drag reduction effect of the riblet-structured surface in uncanonical TBLs is discussed. Finally, the drag reduction mechanism of the riblet-structured surface in a ZPG TBL is analyzed with respect to the quadrant analysis of the near-wall turbulent flows.

5.1 Drag reduction effect in zero-pressure gradient

In order to investigate the friction drag reduction effect of the rolled riblets in ZPG TBLs, the experiments are performed above a flat plate horizontally mounted in the wind tunnel. The PIV and μ-PTV measurements are conducted in the streamwise and wall-normal plane at x = 895 mm, i.e., 3 mm downstream of the riblet-smooth surface transition. The freestream velocities are 8 m/s and 16 m/s resulting in two different Reynolds numbers of Re_Θ = 1200 and 2080 based on the momentum thickness. The riblet spacing is s^+ = 24 and 45 respectively. Furthermore, PIV and μ-PTV are conducted at x = 772 mm (M1) above the riblet surface to investigate the direct impact on the TBL flows. Table 5.1 gives an overview of the parameters in dimensional and dimensionless notations.

As described in chapter 3, the wall-shear stress is determined by the velocity gradient in the near-wall region of $y^+ < 3.5$ in the TBL. The local friction drag reduction ratio is defined as the variation of the wall-shear stress downstream of the riblet surface to the smooth reference surface in equation 3.12.

In figure 5.1, the distribution of the streamwise velocity component above the smooth and the riblet surface is used to determine the wall-shear stress at Reynolds number of Re_θ = 1200 and 2080. To make a direct comparison, the streamwise velocity distributions are scaled by the friction velocity u_τ of the smooth surface. At Re_θ = 1200, the riblet spacing is s^+ = 24 and the riblet height is h^+ = 7.2. It is evident in figure 5.1 (a) that the gradient of the streamwise velocity downstream of the riblet surface is approximately 5% lower than that of the smooth one. This indicates a drag reduction effect by the riblet surface in the same order. The result

agrees well with the results by Bechert *et al.* [34] that a drag reduction ratio of 5 - 6% was achieved by the semi-circular scalloped riblet surface in channel flows. At the higher Reynolds number of $Re_\theta = 2080$, the riblet spacing is increased to $s^+ = 45$ and the riblet height is $h^+ = 13.5$ due to a larger friction velocity. The streamwise velocity distributions of the smooth and riblet configurations in figure 5.1 (b) collapse, indicating no noticeable drag reduction effect exists. The linear fitting of the velocity distribution in the viscous sublayer shows that the velocity gradient decreases by 0.7% for the riblet configuration. Considering the uncertainty of the μ-PTV measurement technique, there is no clear evidence that showing a reduced local wall-shear stress at the higher Reynolds number of $Re_\theta = 2080$.

Table 5.1: Parameters of the flow and riblets in ZPG TBL

Parameter	Dimensional	Dimensionless
Position 1	$x = 895$ mm	-
Freestream velocity	$U_\infty = 8$, 16 m/s	$Re_\theta = 1200$, 2080
Riblet spacing	$s = 1$ mm	$s^+ = 24$, 45
Riblet height	$h = 0.3$ mm	$h^+ = 7.2$, 13.5
Position 2	$x = 772$ mm	-
Freestream velocity	$U_\infty = 8$ m/s	$Re_\theta = 1150$
Riblet spacing	$s = 1$ mm	$s^+ = 21.9$
Riblet height	$h = 0.3$ mm	$h^+ = 6.6$

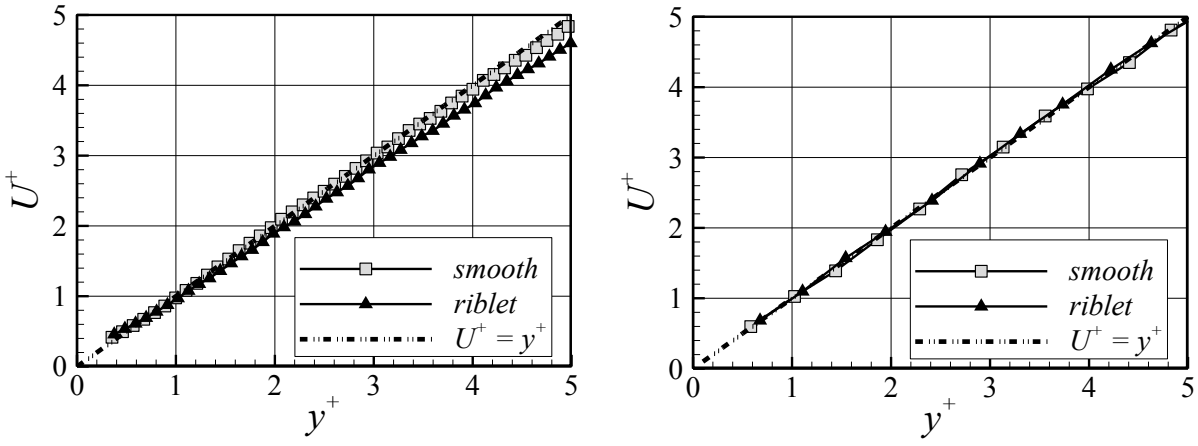

Figure 5.1: Streamwise velocity distribution in the viscous sublayer of the smooth surface and 3 mm downstream of the riblet surface for the zero-pressure gradient turbulent boundary layer; (a) $Re_\theta = 1200$, $s^+ = 24$; (b) $Re_\theta = 2080$, $s^+ = 45$; inner wall units are defined by the friction velocity u_τ of the smooth surface.

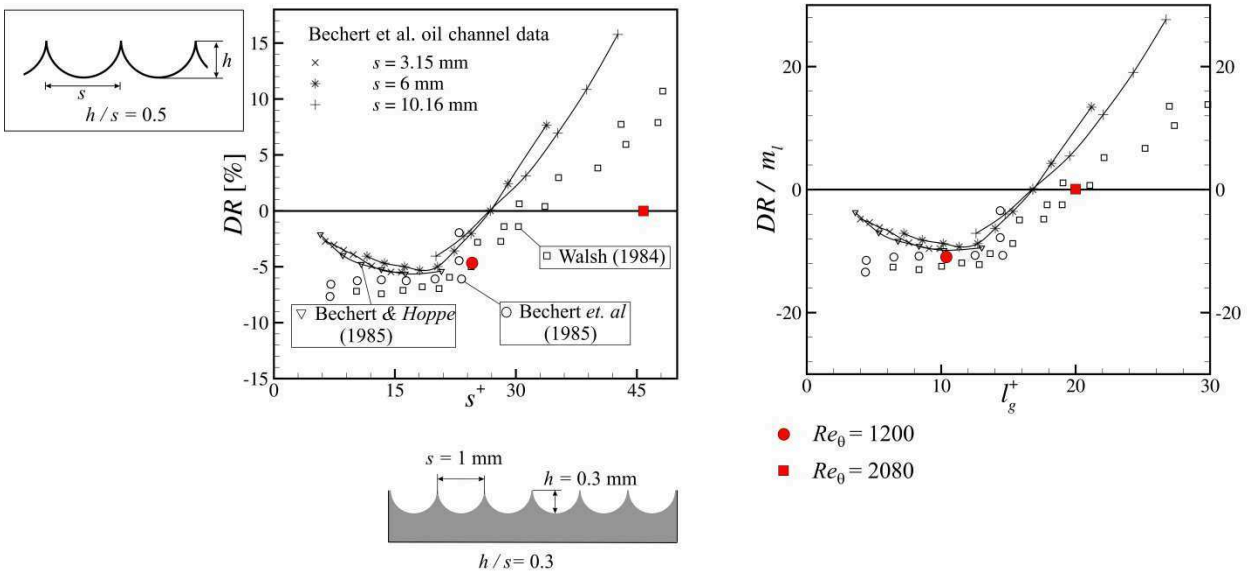

Figure 5.2: Drag reduction ratio (DR) of a semi-circular riblet structure according to Bechert *et al.* [34] versus riblet spacing s^+ in inner coordinates (left) and versus groove-area-based scaling (right); the data of this study are plotted with full symbols.

Many investigations report that the maximum drag reduction by the riblet surface is usually below 10% and the optimal spanwise spacing is about $s^+ = 15$ in wall units. However, the optimal spanwise spacing varies with different riblet geometries. For instance, Bechert *et al.* [34] showed that the maximum drag reduction of 5% occurs at $s^+ = 18$ for the saw-tooth riblet with ridge angle of 60° whereas the optimal spanwise spacing of a semi-circular scalloped riblet is $s^+ = 20$. Thus, the scaling of drag reduction curve of riblets needs to be considered to compare the current measurements with literature. Garcia-Mayoral and Jimenez [47] pointed out that for a particular shape the drag reduction curve can be described in terms of s^+ or h^+, whereas this is not valid when comparing riblets with different geometries. A scaling of the drag reduction curve in terms of the groove cross-section, $l_g^+ = (A_g^+)^{1/2}$ is proposed [47], where A_g^+ is the normalized area of the groove cross-section. The drag reduction is scaled by the viscous slope $m_l = \mu_0/((2c_{f0})^{-1/2} + (2\kappa)^{-1})(\Delta h/l_g)$, where Δh is the protrusion height, κ is the von Karman constant, c_{f0} is the friction coefficient of a smooth surface, and $\mu_0 = 0.66$ is the proportionality constant [47]. The current results along with the results from Walsh and Lindemann [141] and Bechert *et al.* [45] are shown in figure 5.2 with the riblet size normalized by l_g^+ and the drag reduction ratio scaled with the viscous slope of m_l. Apparently, the current results at Reynolds numbers of $Re_\theta = 1200$ and especially of $Re_\theta = 2080$ show a more convincing agreement with the aforementioned results in the new scaling than that in the classical scaling with s^+.

Figure 5.3 shows the comparison of mean streamwise velocity profiles of the TBL above the smooth surface and at 3 mm downstream of the riblet-smooth surface transition. The velocity distributions from the combined PIV and μ-PTV results are plotted in a semi-log. In figure 5.3 (a), the scaling using the same friction velocity u_τ of the smooth configuration at Re_θ = 1200 allows a direct comparison between the smooth and riblet configurations. Meanwhile,

the velocity distributions based on the law of the wall, i.e., the log-law and the near-wall linear distribution, is juxtaposed. Since the friction velocity u_τ is determined from the velocity gradient in the viscous sublayer, the normalized velocity profile of the smooth surface agree with the linear relation of $U^+ = y^+$ at $y^+ < 5$. For the riblet configuration, the magnitude of the velocity is smaller than the smooth configuration, indicating a decreased velocity gradient. In the logarithmic region, the velocity profile of the smooth configuration agrees well with the log-law whereas a slight overshoot of the riblet configuration is noticed. The mean streamwise velocity profiles in figure 5.3 (b) are normalized by the local friction velocity $u_{\tau\text{-}local}$ for both surface configurations. It is shown that the von Karman constant κ of the log-law for the riblet configuration remains the same as that of the smooth configuration, i.e. 0.41, and the intercept of the curve is increased from 5 to 6. The upward shift of the velocity distribution is a significant phenomenon in drag-reduced flows, e.g. TBLs above drag-reduction surface structures [35], [50], spanwise oscillating plate [66], [67], and local surface perturbations [142]. According to Choi [35], the upward shift is related to the balance between the turbulence energy production and the viscous dissipation. It reflects a change of the thickness of the viscous sublayer and the smallest size of turbulent eddies.

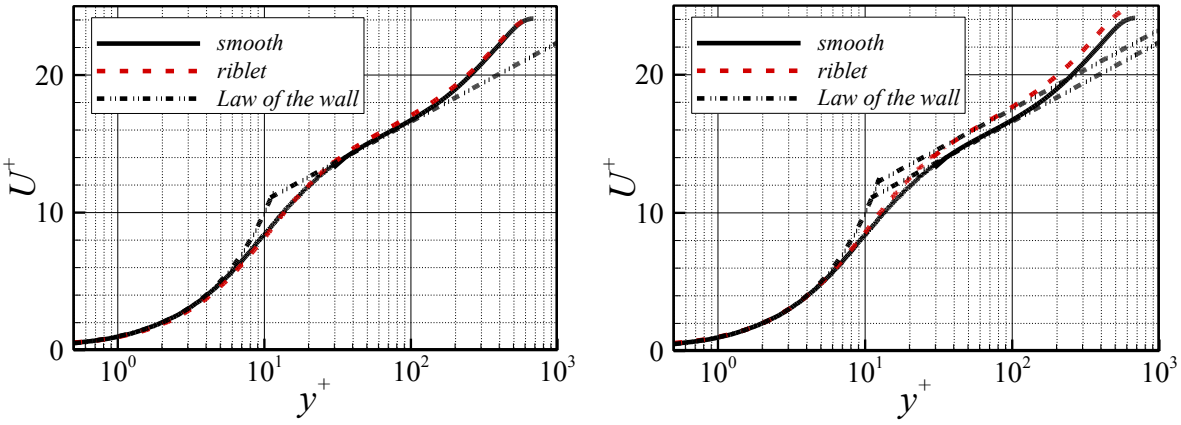

Figure 5.3: Mean streamwise velocity distributions 3 mm downstream of the riblet surface for $Re_\theta = 1200$, compared to the smooth configurations; (a) inner wall units are defined by the friction velocity u_τ of the smooth surface; (b) inner wall units are defined by the local friction velocity $u_{\tau\text{-}local}$ of both surface configurations. Log-law $U^+ = 1/0.41 \ln y^+ + 5$ for the smooth surface and $U^+ = 1/0.41 \ln y^+ + 6$ for the riblet configuration.

In figure 5.4, the distributions of the root-mean-square value of the streamwise and wall-normal velocity fluctuations in inner wall units are compared. The velocity fluctuations are scaled by the friction velocity of the smooth surface and are plotted in a semi-log scale. For $y^+ < 250$, the velocity fluctuations decrease with a magnitude of 3 - 4% for the riblet configuration. The suppression of the velocity fluctuations suggests a reduction of the turbulent kinetic production in the near-wall flows, resulting in the friction drag reduction. In the outer region, such effect is hardly noticeable. This evidences that the modification of the riblet on velocity fluctuations is limited in the inner region whereas no significant impact is found in the outer layer flows. The current results of the streamwise velocity fluctuations

agree well with the HWA results by Choi [35] and Baron and Quadrio [33] and the PIV measurements by Sasamori *et al.* [143].

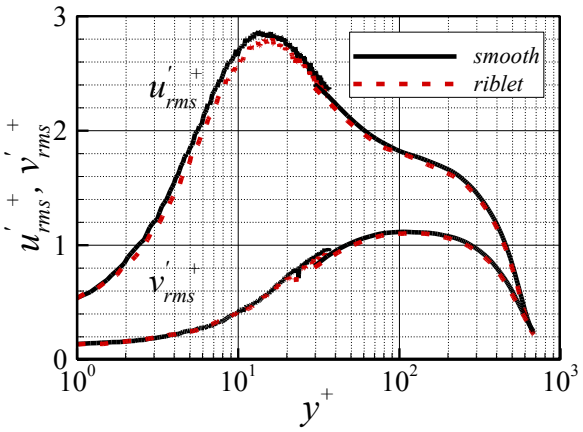

Figure 5.4: Streamwise and wall-normal velocity fluctuations 3 mm downstream of the riblet surface at $Re_\theta = 1200$, compared to the smooth configurations; inner wall units are defined by the friction velocity u_τ of the smooth surface.

5.2 Drag reduction effect in adverse-pressure gradient

The drag reduction effect of riblets in TBLs with pressure gradient has been rarely investigated. Debisschop and Nieuwstadt [144] performed an experimental investigation considering two types of riblet geometries, i.e., triangular and trapezoidal shapes in a TBL with moderate APG. Their measurements showed that the reduction of friction was increased from 9% in ZPG to 13% in APG with the triangular shape riblet. Through LES simulation, Klumpp [41] reported a similar effect that the drag reduction effect of riblets was increased from 4 - 5% in ZPG to 6 - 7% in APG. His results supported the experimental findings by Debisschop and Nieuwstadt [144] although a difference geometry of the riblet was used for the simulation. Recently, Boomsma and Sotiropoulos [145] reported a slight improvement of the friction drag reduction effect of riblet in mild APG. To extend the understanding of the impact of APG on the drag reduction effect, PIV and µ-PTV measurements are performed for the rolled semi-circular riblet configurations.

The experimental setups described in chapter 3 generate two different pressure gradients with the Clauser parameters of $\beta = 0.53$ and 1.15. Similar to the measurements in ZPG TBLs, the local drag reduction is determined by the µ-PTV measurements 3 mm downstream of the transition from the riblet to the smooth surface. The measurements only focus on the riblet parameters with significant drag reduction, i.e. $s^+ \approx 20$ for the ZPG case. Thus, the freestream velocity is adjusted to meet this requirement.

The flow and riblet parameters in the APG TBLs are listed in table 5.2. For the lower pressure gradient configuration of Clauser parameters $\beta = 0.53$, the experiments are conducted at $x = 1410$ mm downstream of the leading edge of the flat plate. The freestream velocity is set to 8.46 m/s resulting in a Reynolds number of $Re_\theta = 3522$ and a riblet spacing of $s^+ = 22.4$. For the higher pressure gradient configuration of $\beta = 1.15$, PIV and µ-PTV measurements are performed at the same location as the measurements at the ZPG condition,

i.e., x = 895 mm. The freestream velocity is set to 8.75 m/s resulting in a local Reynolds number Re_θ = 1955 at the measurement position. The riblet spacing is s^+ = 21.7 based on the friction velocity of the smooth surface.

Table 5.2: Parameters of the flow and riblets in adverse-pressure gradient turbulent boundary layer.

Parameter	Dimensional	Dimensionless
Position	x= 1410, 895 mm	-
Freestream velocity	U_∞ = 8.46, 8.75 m/s	Re_θ = 3522, 1955
Riblet spacing	s = 1 mm	s^+ = 22.4, 21.7
Riblet height	h = 0.3 mm	h^+ = 6.7, 6.5
Pressure gradient	dp/dx = 8.25, 30.7	β = 0.53, 1.15

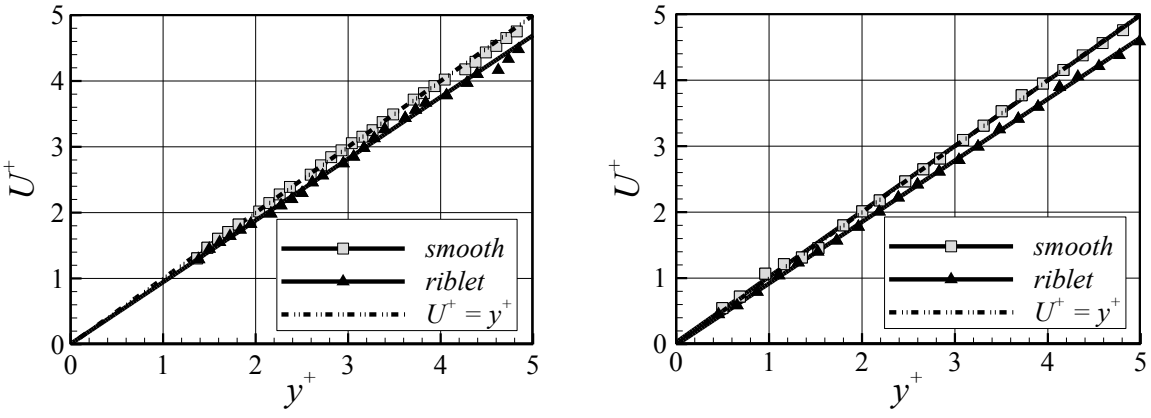

Figure 5.5: Streamwise velocity distribution in the viscous sublayer above the smooth surface and 3 mm downstream of the riblet surface in the adverse-pressure gradient turbulent boundary layer; (a), Re_θ = 3522, β = 0.53, and s^+ = 22.4; (b) Re_θ = 1955, β = 1.15, and s^+ = 21.7; inner wall units are defined by the friction velocity u_τ of the smooth surface.

The near-wall velocity distributions measured by μ-PTV above the smooth surface and 3 mm downstream of the riblet surface in the TBLs with both APG configurations are juxtaposed in figure 5.5. Clearly, the velocity distributions shows smaller gradients for the riblet configuration indicating a local drag reduction of 6% for β = 0.53 and 7% for β = 1.15. The comparison with the results in ZPG indicates that the local drag reduction is increased by around 1% and 2% respectively for APG configurations. To visualize the impact of adverse-pressure gradient on the drag reduction effect of the riblet surface, the difference in the drag reduction ratio between the ZPG and APG configurations based on several experimental and numerical investigations [37] [48] [144] [145] is listed in figure 5.6. It is noticed that with a similar Clauser parameter the current measurements agree well with the LES simulation by Boomsma and Sotiropoulos [145]. Note that the ratio of the riblet height to the spacing h / s is 0.3 whereas in the simulation of Boomsma and Sotiropoulos [145] h / s is 0.5. For a larger

Clauser parameter β = 1.15, i.e., a higher pressure gradient, the drag reduction effect increases. This shows a similar tendency as the experimental findings by Debisschop and Nieuwstadt [144] and Nieuwstadt *et al.* [37].

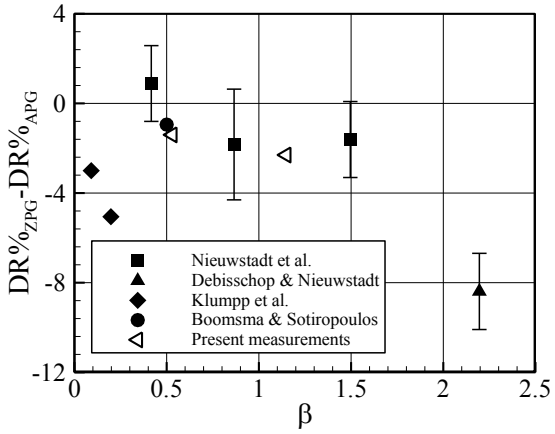

Figure 5.6: The variations of the drag reduction by riblets in zero-pressure gradient and adverse-pressure gradient TBLs as a function of the Clauser parameter. The present experimental results are compared with the large-eddy simulation results of Boomsma and Sotiropoulos [145], Klumpp *et al.* [48], and the measurements of Debisschop and Nieuwstadt [144] and Nieuwstadt *et al.* [37].

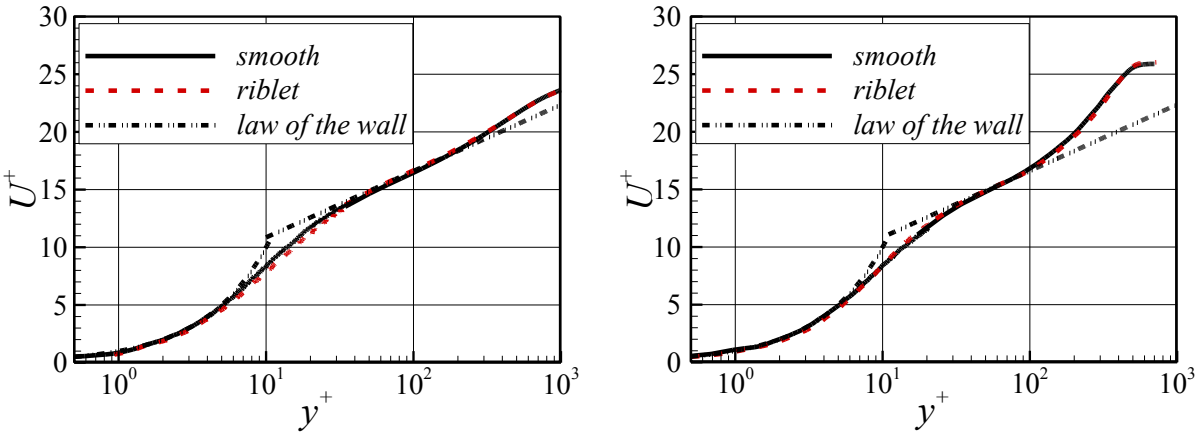

Figure 5.7: Streamwise velocity distributions for the smooth surface and 3 mm downstream of the riblet surface in the adverse-pressure gradient turbulent boundary layer; (a), Re_θ = 3522, β = 0.53, and s^+ = 22.4; (b) Re_θ = 1955, β = 1.15, and s^+ = 21.7; inner wall units are defined by the friction velocity u_τ of the smooth surface.

The streamwise velocity distributions measured by μ-PTV and PIV for the two APG configurations are depicted in figure 5.7 for the smooth and riblet configurations, both normalized by the friction velocity u_τ of the smooth configurations. To ensure a similar spatial resolution, the FOV of the lower pressure gradient configuration only covers 1000 wall units in the PIV measurement. In figure 5.7 (b), the mean streamwise velocity profile shows a larger defect than that in the ZPG TBL due to a lower wall-shear stress induced by the APG. Similar to the findings in ZPG, the streamwise velocity distributions in the

logarithmic region and the wake region are almost identical for the riblets and the smooth surfaces.

In figure 5.8, the streamwise and wall-normal velocity fluctuations and the Reynolds shear stress 3 mm downstream the riblet and above the smooth surfaces are plotted for the smaller APG of Clauser parameters β = 0.53. For the smooth configuration, two peaks of the steamwise velocity fluctuation are observed. The near-wall fluctuation peak $u'_{\text{rms-peak}}$ reaches approximately 3 and it is 10% higher compared to the ZPG TBL. The wall-normal position of this peak is invariant around $y^+ = 15$ which agrees with the LES simulation by Bobke *et al.* [146]. The second peak, which occurs in the outer layer of the boundary layer, is related to the strength of the pressure gradient. The magnitudes of the streamwise and wall-normal velocity fluctuations and the Reynolds shear stress are increased in the outer region due to the pressure gradient. Comparing the smooth and riblet cases, it is observed that the impact of riblets on the streamwise and wall-normal velocity fluctuations is not significant and is limited in the region of $y^+ < 200$. In figure 5.8 (b), the Reynolds shear stress is reduced by approximately 6% due to the riblet surface at $y^+ < 200$ - 300.

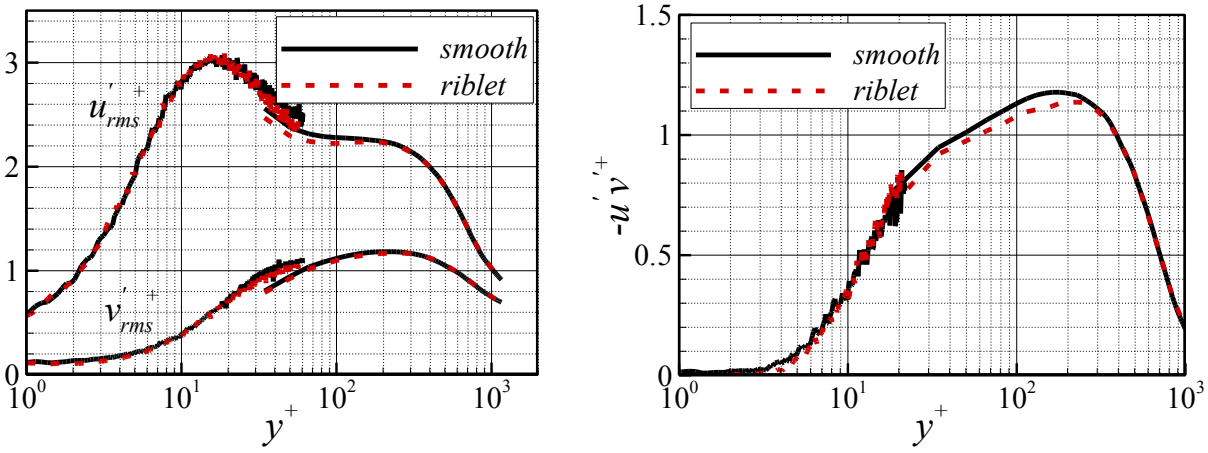

Figure 5.8: Streamwise and wall-normal velocity fluctuations 3 mm downstream of the riblet surface for the mild adverse-pressure gradient turbulent boundary layer compared to the smooth configuration, Re_θ = 3522, β = 0.53, and s^+ = 22.4; inner wall units are defined by the friction velocity u_τ of the smooth surface.

5.3 Drag reduction effect in unsteady flow

PIV measurements are conducted for the smooth and the riblet configurations in a ZPG TBL to investigate the influence of unsteady inflows on the drag reduction mechanism. The unsteady flow setup has been described in section 3.1.

The PIV measurements are conducted at x = 1410 mm downstream of the leading edge of the flat plate for the smooth and the riblet configurations. Similar to the measurements in sections 5.1 and 5.2, the PIV measurement area is divided into two FOVs, i.e., one FOV covers the complete TBL and the second FOV covers an area of 3.5 mm × 3.5 mm in the near-wall region. To determine the instantaneous velocity distribution for the measurements in the

small FOV, the particle images are post-processed using the cross-correlation PIV algorithm with a rectangle interrogation window of 8 × 48 pixels. The instantaneous wall-shear stress is determined by a linear fitting in the viscous sublayer of $y^+ < 4$ with 5 measurement points. In figure 5.9, the unsteady freestream velocity is determined by PIV in the upper part of the large FOV. The results show that the freestream velocity possesses a sinusoidal distributions at a frequency $f = 0.5$ Hz and a mean velocity of 7.35 m/s. The local Reynolds number based on the time-averaged flow field is $Re_\theta = 1573$ and the friction velocity of the smooth configuration is $u_\tau = 0.313$ m/s, resulting in a riblet spacing of $s^+ = 20.4$.

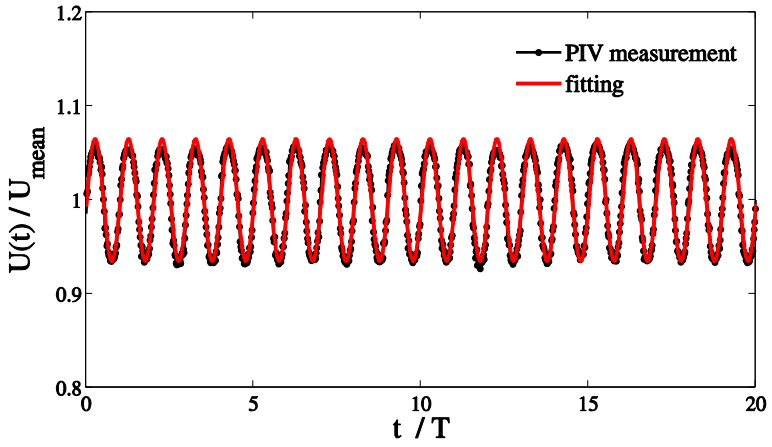

Figure 5.9: Pulsating freestream velocity out of the turbulent boundary layer measured by PIV, $U_\infty(t) / U_{mean} = 0.065 \sin(\pi t)+1$.

The measurement frequency of PIV is 25 Hz. For each configuration, 60,000 image pairs are acquired. The flow fields for each phase of the periodical inflow have been analyzed in a phase-locked sense. In figure 5.10, the phase-averaged velocity distributions in the TBL are plotted with different wall-normal positions. It is shown that with different wall-normal distance of y = 0.6, 3.6, and 19.6 mm the phase-averaged streamwise velocities possess a similar sinusoidal distribution as the freestream velocity. This indicates that the turbulent statistics, as well as the wall-shear stress, are dependent variables of the phase of the freestream velocity.

In figure 5.11, the phase-averaged local friction coefficient c_f is depicted for the smooth and riblet configurations. The c_f values are determined from the freestream velocity and the wall-shear stress of each phase. The distribution shows a smaller c_f for the phase of $0.5T$ with a higher freestream velocity, i.e., a larger Reynolds number. Compared with the smooth configuration, the time-averaged friction coefficient of the riblet configuration shows a reduction of 6.7%, suggesting a slightly higher drag reduction ratio of 2% than that within a ZPG configuration. Note that the current riblet spacing of $s^+ = 20.4$ is smaller than the one in the steady ZPG configuration. Considering $s^+ = 20.4$ approaches the optimal riblet spacing of the drag reduction diagram in figure 5.2 (a), it is difficult to determine whether the higher drag reduction is a conquence of the unsteadiness of the flow or a smaller riblet spacing. Nevertheless, the current measurements indicate that the drag reduction effect of the semi-circular riblet is still effective in a TBL with pulsating inflows.

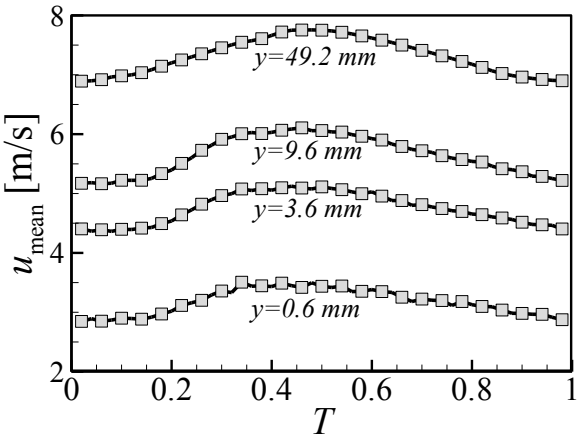

Figure 5.10: Phase-averaged velocity distributions in the turbulent boundary layer with different wall-normal distance.

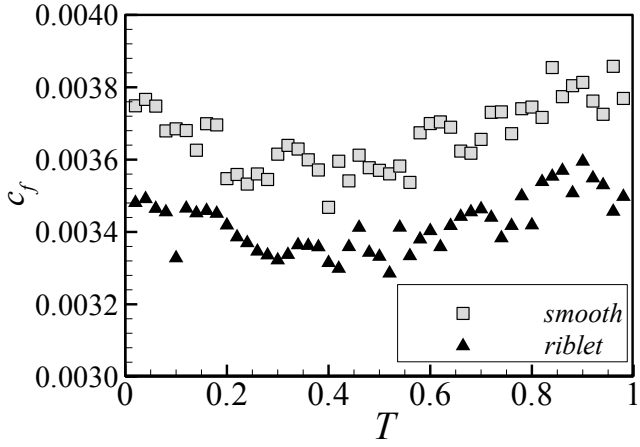

Figure 5.11: Phase-averaged wall-shear stress distributions in the turbulent boundary layer with pulsating inflow condition.

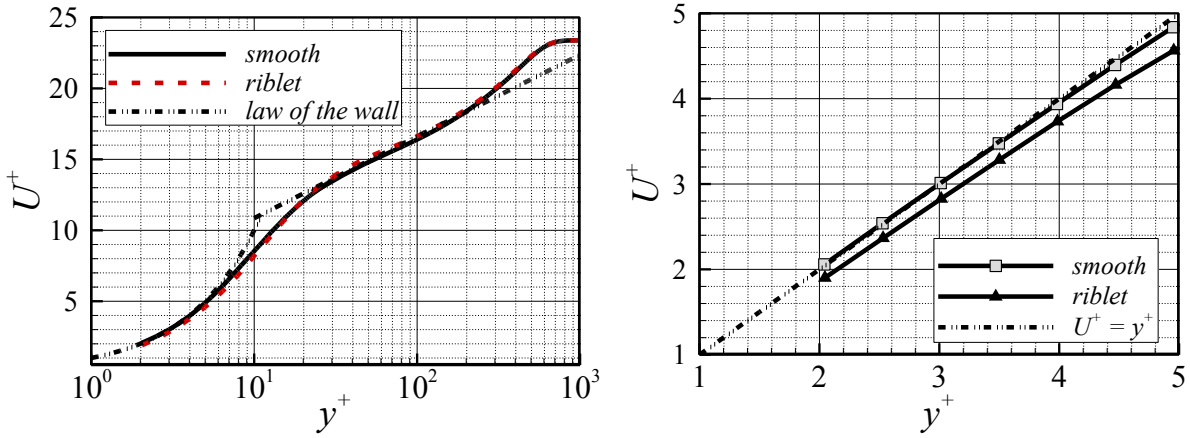

(a) (b)

Figure 5.12: Time-averaged streamwise velocity distribution measured by the PIV 3 mm downstream of the riblet surface, compared to the smooth configurations; inner wall units are defined by the friction velocity u_τ of the smooth surface.

Figure 5.12 shows the time-averaged streamwise velocity distributions for the smooth and the riblet surfaces. The streamwise velocity distributions are averaged from all the 60,000 snapshots in each set of the PIV and μ-PIV measurements. The semi-log plot of the streamwise velocity distributions in figure 5.12 (a) indicate that the streamwise velocity for both surface configurations agree well with the log-law in the region of $35 < y^+ < 250$. The riblet configuration shows a slight overshoot which has been noticed in ZPG and APG TBLs. To mark the influence of the riblet structure on the near-wall flow, the enlargement of the viscous sublayer is illustrated in the linear scaling. A lower velocity gradient for the riblet configuration is exhibited in figure 5.12 (b), indicating a drag reduction ratio of 6.7% compared with the smooth configuration.

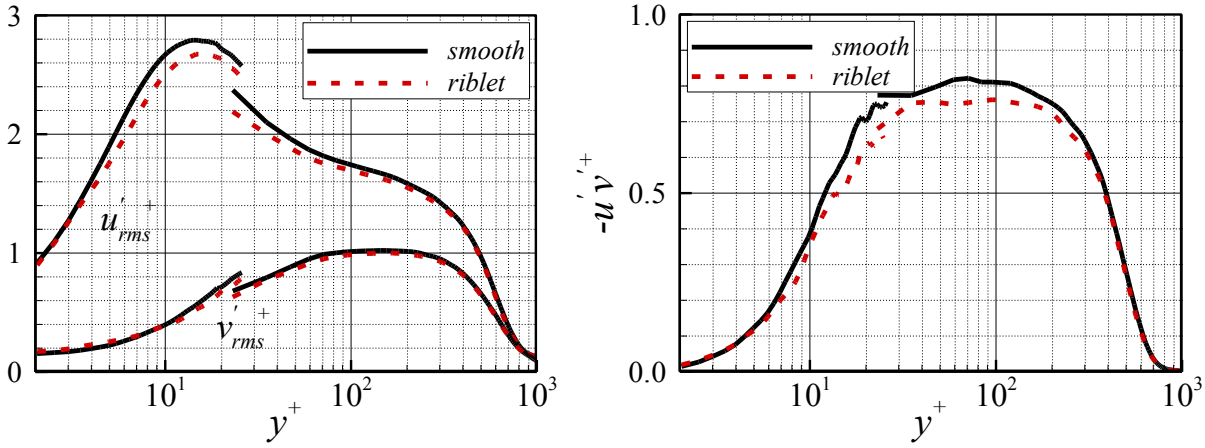

Figure 5.13: Time-averaged streamwise and wall-normal velocity fluctuations (a) and Reynolds shear stress (b) 3 mm downstream of the riblet surface comparing with the smooth configurations; inner wall units are defined by the friction velocity u_τ of the smooth surface.

Figure 5.13 depicts the streamwise and wall-normal velocity fluctuations and the Reynolds shear stress for both configurations. Similar to the aforementioned finding in ZPG and APG, the unsteady inflow results demonstrate smaller fluctuations for the riblet configuration in the region of $y^+ < 250$. The Reynolds shear stress is decreased for the riblet configuration at $y^+ < 350$ with the maximum reduction of 10% at $y^+ = 70$. The reduction of the turbulence production is more pronounced than that in the steady ZPG TBLs due to a higher drag reduction ratio.

5.4 Influence on the flow

To investigate the influence of the riblet structure on the TBL flows, PIV and μ-PTV measurements are conducted above the riblet surface in the ZPG TBL. The measurement location is at M2, $x = 772$ mm downstream of the leading edge of the flat plate. This results in a local Reynolds number $Re_\theta = 1150$ with the freestream velocity of $U_\infty = 8$ m/s.

The main difficulty in determining the velocity profile above riblet surfaces is that no predefined origin exists for the wall-normal coordinate [33]. Figure 5.14 shows the streamwise velocity distributions above the riblet trough and the crest while the origin is

placed at the riblet valley. Due to the riblet structure, the velocity distribution inside the riblet trough, i.e. $y^+ < 7$, cannot be measured by the current 2D-2C μ-PTV techniques. The results indicate that in the near-wall region the streamwise velocity profile above the riblet trough coincide with the one above the crest. In the region of $y^+ > 40$, the velocity distributions above the riblet trough and crest are not affected by the riblet structure. This confirms the LES simulations by Klumpp [41]. Similarly, Djenidi and Antonia [147] showed that the spanwise variation in the streamwise velocity only exists with a distance of about one riblet height above the riblet crest plane. In their LDA measurement, the spanwise dimension of the measurement volume of the LDA is only 1/5 of riblet spacing. In contrast, in the current PIV and μ-PTV measurements the thickness of the laser light sheet is about 0.5 mm covering half of the riblet spacing. The small variation of the velocity distributions above the riblet trough and crest can be explained by the averaging effect in the spanwise direction.

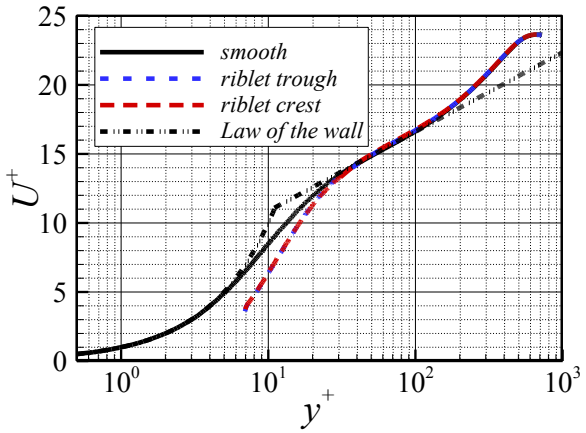

Figure 5.14: Mean streamwise velocity distributions above of the riblet surface for $Re_\theta = 1150$, compared to the smooth configurations; inner wall units are defined by the friction velocity u_τ of the smooth surface; the origin points are placed at the riblet valley.

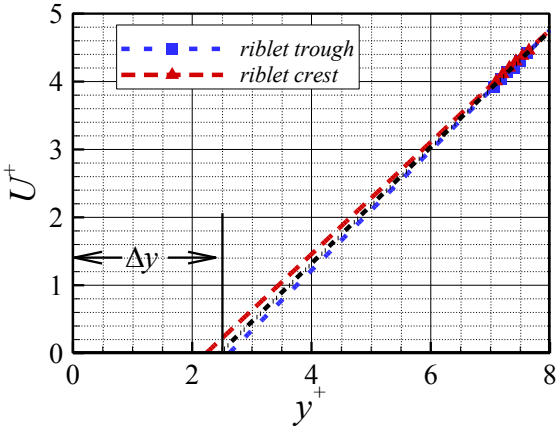

Figure 5.15: Determination of the virtual origin Δy.

According to Bechert and Bartenwerfer [53] and Djenidi and Antonia [147], a virtual origin of the riblet configuration is introduced to compare the TBL flows above the riblet and the smooth surfaces. The virtual origin Δy is defined as the origin of the spanwise averaged velocity profiles [53]. In figure 5.15, the streamwise velocity profiles are linearly extended from $U^+ < 4.5$ to $U^+ = 0$ on the y-axis. The intersection Δy defines the virtual origin. The

virtual origin determined in figure 5.15 is located at $\Delta y^+ = 2.5$ and the longitudinal protrusion height $h_{lp}^+ = h^+ - \Delta y^+$ is 4.1, approximately. Thus, the protrusion height h_{lp}^+ of the riblet surface is 19% of the lateral riblet spacing and it is below the upper limit of 22% in the analytical solution by Bechert and Bartenwerfer [53]. The streamwise velocity distributions with the zero point located at the virtual origin are plotted in figure 5.16. Clearly, the velocity profiles of both configurations collapse in the near-wall region.

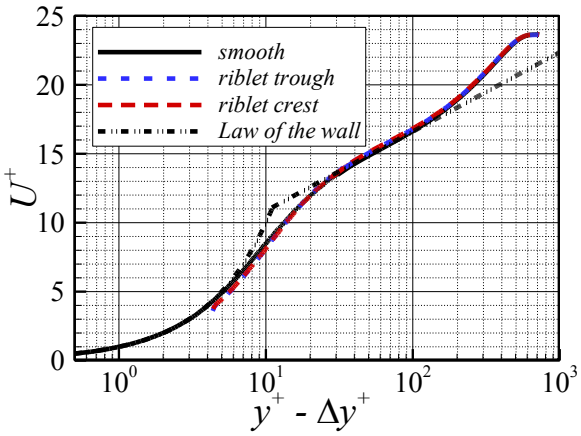

Figure 5.16: Mean streamwise velocity distributions above of the riblet surface for $Re_\theta = 1150$, compared to the smooth configurations; inner wall units are defined by the friction velocity u_τ of the smooth surface; the origin points are placed at the virtual origin.

In figure 5.17, the streamwise and wall-normal velocity fluctuations above the riblet and the smooth surfaces for $Re_\theta = 1150$ are juxtaposed. For both configurations, the peak values of the streamwise velocity fluctuations lie at $y^+ = 15$. This agrees well with the results in section 4.4.2 that the maximum streamwise velocity fluctuation occurs at $y^+ \approx 15 \pm 1$ above a smooth surface. The results indicate a larger reduction of the velocity fluctuations than that from the measurements downstream of the riblet surface. This is due to the flow recovery effect downstream of the riblet-smooth transition.

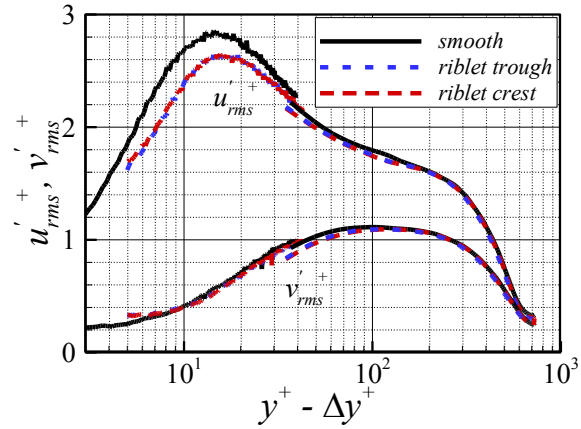

Figure 5.17: Comparison of the distributions of the streamwise and wall-normal velocity fluctuations above the riblet surface for $Re_\theta = 1150$, compared to the smooth configurations; inner wall units are defined by the friction velocity u_τ of the smooth surface.

An instantaneous flow field in the *x-y* plane is plotted in figure 5.18 to show the turbulent bursting events. The vectors denote the fluctuating velocity (*u' v'*) in the streamwise and wall-normal direction. The ejection and sweep (Q2 and Q4) events are highlighted in figure 5.18 to illustrate the near-wall flow structures. In the following, a quadrant analysis of the turbulence production is considered to determine the impact of riblets on the near-wall turbulent structures.

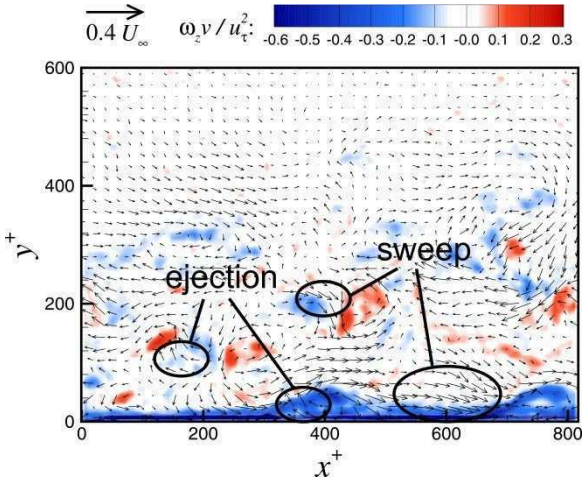

Figure 5.18: Instantaneous fluctuating flow field (*u'*, *v'*) in the *x-y* plane, ejection and sweep events are highlighted. For clarity, only one in three vectors are plotted in the streamwise direction and one in three are plotted in the wall-normal direction.

The quadrant decomposition of turbulence production is conducted by introducing a joint probability density function (joint-PDF) of the streamwise and wall-normal velocity fluctuations *u'* and *v'*. The joint-PDF *u'v'P(u',v')* is weighted by the probability density function *P(u',v')* and the fluctuating velocity components *u', v'*. In TBL flows, the joint-PDF reveals how the velocity components contribute to the Reynolds shear stress *-u'v'*. The joint-PDFs plotted in figure 5.19 are determined from the PIV measurements at y^+ = 18 and 63 above the riblet and the smooth surfaces with 2800 snapshots. The velocity fluctuations are normalized by the root-mean-square value of the smooth surface. At y^+ = 18 (figure 5.19 (a)), a significant reduction for the Q4 motions is found above the riblet trough and the crest. This indicates that the sweep events are suppressed due to the riblet structure, leading to a reduction of the Reynolds shear stress. The same effect was reported in the hot-wire measurements by Tamano and Itoh [80] and LES simulations by Klumpp *et al.* [148] over moving surfaces. They found that the *u'* component was weakened in the sweep and ejection events within drag reduction cases. The suppression of the Q4 motions is also observed for the joint-PDFs at y^+ = 63 in the logarithmic region (figure 5.19 (b)). However, the suppression effect is not as significant as that in the near-wall region. Since the sweep events interact with the ejection events in the turbulence regeneration process, the Q2 motions are weakened as well above the riblet structure.

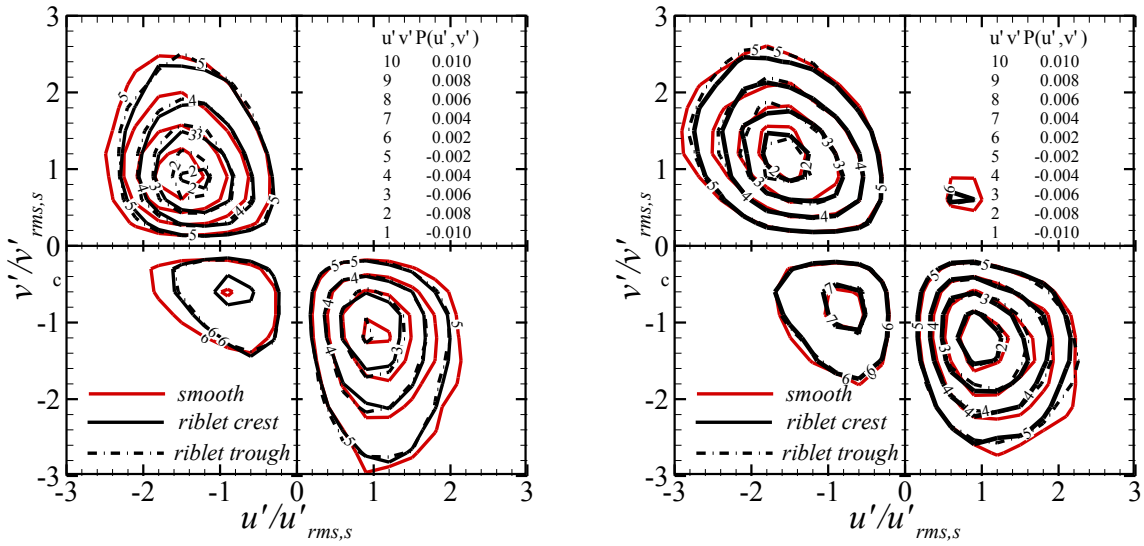

(a) $y^+ = 18$ (b) $y^+ = 63$

Figure 5.19: Comparison of the joint probability density functions (joint-PDF) *u'v'P(u',v')* determined from the PIV data above the riblet and the smooth surfaces at $Re_\theta = 1150$; the streamwise and wall-normal velocity fluctuations are scaled by the root-mean-square values of the smooth configuration.

A quadrant decomposition of the Reynolds shear stress is performed to show the contributions from the fluctuating streamwise and wall-normal velocity to the total turbulent energy production. The Reynolds shear stress is decomposed as

$$\overline{u'v'} = \sum_{i=1}^{4} \overline{u'v'}B_i \tag{5.1}$$

where the index i indicates the four quadrants and B_i indicates the probability of the Reynolds shear stress in each quadrant. The quadrant decompositions of the Reynold stress $\overline{u'v'}B_i$ as well as the total value of the Reynolds shear stress $\overline{u'v'}/u_\tau^2$ in the wall-normal direction above the riblet crest and the smooth surface are plotted in inner wall units in figure 5.20. It is clearly shown that the magnitudes of the Reynolds shear stress are reduced by about 10% by riblets in the region of $y^+ < 200$. The decompositions of the Reynolds shear stress in quadrant 2 and 4 possess lower magnitudes, indicating that the reduction of the Reynolds shear stress above the riblet surface is due to a less contribution from Q2 and Q4 events. The intensity of the Reynold shear stress due to the Q2 and Q4 events are decreased significantly in the region of $y^+ < 200$, whereas the magnitudes of the Q1 and Q3 events are virtually unchanged. This leads to an eventual reduction of the total Reynolds shear stress in the inner layer above the riblet surface. In conclusion, the decrease of the intensities of Q2 and Q4 events agrees with the analysis of the joint-PDFs that the fluctuating velocity components are suppressed by the riblet structure.

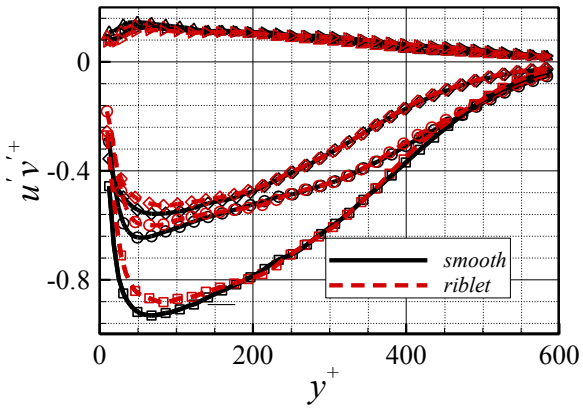

Figure 5.20: Quadrant decomposition of the Reynolds shear stress $\overline{u'v'}/u_\tau^2$ in the wall-normal direction above the riblet crest and the smooth surface at $Re_\theta = 1150$; the Reynolds shear stress is scaled by the friction velocity of the smooth surface; Q1, delta; Q2, circle; Q3, right triangle; Q4, diamond; total Reynolds shear stress, square.

5.5 Summary

In this chapter, the friction drag reduction effect of the semi-circular riblet surface is investigated by PIV and μ-PTV in the TBLs with different inflow conditions, e.g., zero and adverse pressure gradient, and periodical unsteady freestream inflows.

The results of the ZPG configuration show a local friction drag reduction of approximately 5% by riblets at Re_θ = 1200 with s^+ = 24 and 0.7% at Re_θ = 2080 with s^+ = 45, resulting in a convincing agreement with the friction force measurements in channel flows by Bechert *et al.* [34]. Results of the adverse pressure gradient and the unsteady inflow configurations indicate a slightly higher drag reduction than that of the ZPG configuration due to the smaller riblet spacing. The streamwise and wall-normal velocity fluctuations, as well as the Reynolds shear stress, are decreased compared with the smooth surface for all the flow configurations in the inner region. This suggests that the turbulence energy production and the viscous dissipation are altered by the riblet structure. Furthermore, measurements above the riblet surface are conducted using PIV and μ-PTV at a local Reynolds number Re_θ = 1150 in ZPG TBL. The quadrant decompositions of the turbulence production depict that the sweep and ejection events are suppressed due to the riblet structure. This leads to a reduction of the turbulence production.

6 Active friction drag reduction

In this chapter, the combination of the passive and the active friction drag reduction methods is investigated by imposing a surface wave motion on an aluminum riblet surface. The first part of this chapter summarizes the investigations of the spanwise traveling surface wave on a smooth surface. The impact of the wave parameter and the inflow conditions are analyzed. The second part concentrates on the combination of the passive and the active drag reduction methods. The passive semi-circular riblet surface is excited by a spanwise traveling transversal surface wave motion with wall-normal deformation. First, the freestream Reynolds number, the wavelength, and the frequency of the transversal wave remain constant whereas the amplitude of the surface wave is increased, i.e., the perturbation imposed on the TBL is enlarged. Subsequently, the influence of a higher freestream Reynolds number and an adverse-pressure gradient is investigated regarding the drag reduction effect and the turbulence statistics. Finally, the near-wall flow field perpendicular to the wall-normal direction is analyzed by conducting a stereoscopic PIV above the moving riblet surface.

6.1 Transversal waves of a smooth surface

The parameters of a spanwise traveling transversal surface wave have certain impact on the drag reduction effect. Roggenkamp *et al.* [15] studied the influence of the wave parameters and the flow conditions. The results showed that the local friction drag reduction caused by the wave motion is up to 3.4% at $Re_\Theta = 1200$ at wave amplitude $A^+ = Au_\tau/\nu = 9$, wavelength $\lambda^+ = \lambda u_\tau / \nu = 3862$, and period $T^+ = u_\tau^2 / (f\nu) = 110$, i.e., frequency of $f^+ = f\nu / u_\tau^2 = 0.009$.

Figure 6.1 compares the distributions of the streamwise velocity in the viscous sublayer at $Re_\Theta = 1200$ and wave period of $T^+ = 110$. The wave amplitudes are $A^+ = 6$, 7, and 9, respectively. The velocity distributions clearly show lower gradients for the actuated surface compared with the non-actuated configuration. This confirms a reduction of the friction drag. Furthermore, the results evidence that the friction drag reduction effect grows as the wave amplitude increases. The maximum drag reduction up to 3.4% occurs at the highest amplitude of $A^+ = 9$. A similar trend is observed by Koh *et al.* [42] in their LES simulations of TBLs above a surface actuated by spanwise traveling transversal waves. Their numerical results show the optimal wave amplitude is around $A^+ = 50$ for $Re_\Theta = 2000$ and 5000. The drag reduction increases with the increase of the wave amplitude. The drag reduction starts to drop when the amplitude is increased to $A^+ = 70$. In this study, due to the limitation of the actuator system, the drag reduction effect of the wave motion is not investigated for wave amplitudes higher than $A = 0.5$ mm.

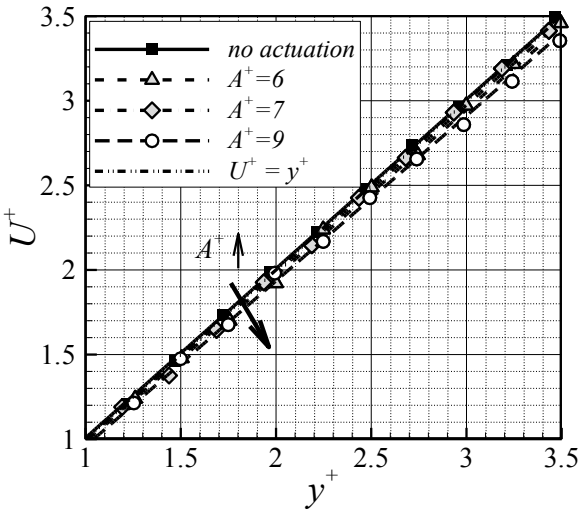

Figure 6.1: Comparison of the mean streamwise velocity distributions in the viscous sublayer at $Re_\Theta = 1200$, $T^+ = 110$, $\lambda^+ = 3862$, and $A^+ = 6$, 7, and 9. The results show local drag reduction of 2.0, 2.7, and 3.4% for the three amplitudes, correspondingly. Inner wall units are defined by the friction velocity of the non-actuated surface (reproduced from Roggenkamp *et al.* [15]).

Table 6.1 summarizes the local drag reduction ratio of the spanwise traveling transversal surface wave at three different Reynolds numbers [15]. The measurements are conducted at three different Reynolds numbers of $Re_\Theta = 1200$, 1660, and 2080. The corresponding friction velocity $u_\tau = 0.364$, 0.515, and 0.671 m/s are determined through a linear fitting in the viscous sublayer. The surface wave possesses a constant wavelength of $\lambda = 160$ mm, a frequency of $f = 81$ Hz, and three amplitudes of $A = 0.25$, 0.3, and 0.375 mm. Thus, the dimensionless wavelength, wave amplitude, and wave period increase simultaneously for higher Reynolds numbers. The results show a drag reduction of 3.4% with $A = 0.375$ mm at $Re_\Theta = 1200$ and DR = 0.6% at $Re_\Theta = 1660$. Furthermore, at the highest Reynolds number of $Re_\Theta = 2080$, a slight trend toward drag increase is observed. Note that the variations of the friction drag between the actuated and non-actuated cases for $Re_\Theta = 1660$ and 2080 are smaller than 1% which are lying in the interval of measurement uncertainty.

Table 6.1: Local friction drag reduction for the actuated smooth surface at three Reynolds numbers and three wave amplitudes; the normalized parameters are defined by $A^+ = Au_\tau / \nu$, $T^+ = u_\tau^2 / (f\nu)$, $\lambda^+ = \lambda u_\tau / \nu$ where the nominal friction velocity u_τ is determined above the non-actuated smooth surface [15].

Re_θ	T^+	λ^+	A^+	DR (%)
1200	110	3862	6	2
1200	110	3862	7	2.7
1200	110	3862	9	3.4
1660	230	5536	9	0.4
1660	230	5536	10	0.6

1660	230	5536	13	-0.3
2080	380	7170	11	-0.4
2080	380	7170	14	-0.2
2080	380	7170	17	-0.7

A spanwise traveling wave motion has been shown as a potentially effective control method for drag reduction by Roggenkamp *et al.* [15] whereas the influence of the parameters on the drag reduction mechanism is not fully understood, yet. Therefore, the following analysis focuses on the impact of the wave frequency and amplitude on the drag reduction effect.

Table 6.2: Experimental parameter combinations of the wave frequency and the amplitude with a constant wavelength of λ = 160 mm at Re_θ = 1200.

A^+	f	T^+
6.1	27, 54 Hz	302.5, 158
7.4	27, 54 Hz	302.5, 158
8.9	27, 54 Hz	302.5, 158
11.8	27, 54 Hz	302.5, 158

To analyze the impact of the wave period on the drag reduction effect of the spanwise traveling transversal surface wave motion, PIV and μ-PTV measurements are conducted at different wave frequencies and a constant Reynolds number of Re_Θ = 1200 based on the momentum thickness Θ at x = 895 mm (M2). Similar to Roggenkamp *et al.* [15], the wavelength of the surface wave is kept at a constant value of λ = 160 mm, whereas four amplitudes, namely A = 0.26, 0.315, 0.375, and 0.5 mm are investigated. Additionally, two more frequencies of f = 27 and 54 Hz are analyzed. In table 6.2, the parameter combinations of the wave frequency and amplitude are summarized. In the following, all values are listed in both dimensional and dimensionless forms. The wave parameters correspond to dimensionless values of amplitude A^+ = 6.1, 7.4, 8.9, and 11.8 and period T^+ = 302.5 and 158 (f^+ = 0.003, 0.006).

The μ-PTV and PIV measurements are conducted at the measurement position of x = 895 mm (M2) which is chosen to be similar to the investigation by Roggenkamp *et al.* [15]. The distance from M2 to the moving surface is 3 mm corresponding to 75 wall units.

The local drag reduction ratio downstream of the actuated surface at M2 is plotted in figure 6.2 for the combinations of different frequencies and amplitudes as well as the findings by Roggenkamp *et al.* [15]. On the one hand, the maximum drag reduction of 3.8% is found at the highest amplitude A^+ = 11.8 with a normalized actuation period of T^+ = 158. With an increasing wave amplitude the drag reduction ratio is found to increase, which agrees with the findings by Roggenkamp *et al.* [15]. On the other hand, with the lowest frequency of f = 27 Hz corresponding to T^+ = 302.5, the maximum drag reduction is less than 1%.

Considering the uncertainty of the measurement technique, there is no distinct drag reduction effect. Clearly, the results indicate a frequency dependent effect of the drag reduction, i.e., higher excitation frequency leads to stronger drag reduction effect. A similar frequency dependent effect was reported by various studies for different control strategies. For instance, Gatti *et al.* [69] showed that the drag reduction of the spanwise oscillating surface in a channel flow increases when the oscillation period decreases and an optimal value exists at $T^+ \approx 70$. Due to the strong acceleration induced by surface excitation, the actuator system is not able to generate a surface wave with a higher frequency. Thus, no optimal value of T^+ is observed in this study.

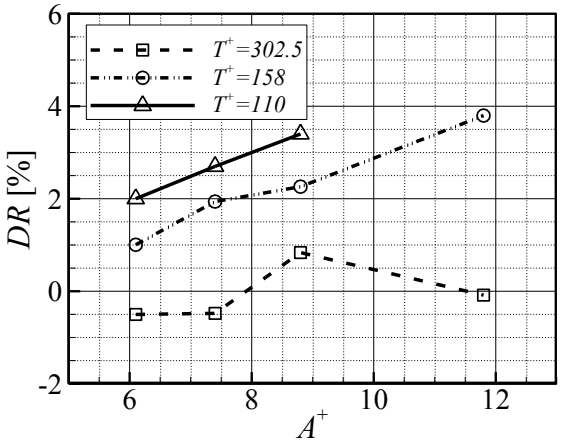

Figure 6.2: Local drag reduction ratio derived from the μ-PTV measurements at M2 as a function of the wave amplitude and period. The results of $T^+ = 110$ ($f^+ = 0.009$) are from Roggenkamp *et al.* [15] using the same experimental setup.

6.2 Transversal waves of a riblet-structured surface

The riblet surface investigated in chapter 5 is excited by the actuator system to generate a spanwise traveling transversal surface wave such that the passive and active flow control approaches are combined for friction drag reduction. The PIV and μ-PTV measurements are conducted at two Reynolds numbers of $Re_\Theta = 1200$ and 2080. The spanwise traveling surface wave motion imposed on the riblet surface possesses different amplitudes and a constant wavelength of $\lambda = 160$ mm. To investigate the impact of the excitation frequency, the surface is actuated at $f = 54$ and 81Hz. The parameters of the wave motion are listed in table 6.3 and table 6.4 in dimensional and dimensionless notations. The dimensionless riblet spacing is $s^+ = 24$ for $Re_\theta = 1200$ and $s^+ = 45$ for 2080 which are consistent with the ones in chapter 5. Note that the friction velocity u_τ above the non-actuated smooth surface is used to normalize the variables since it is the smooth flat-plate flow which defines the reference of the non-actuated and actuated riblet surface flows. In the measurement of $f = 54$ Hz, the friction velocity u_τ is slightly smaller comparing with the one at $f = 81$ Hz above the smooth surface.

Table 6.3: Experimental parameter of the spanwise traveling transversal wave motions, 3 amplitudes with a constant wavelength of $\lambda = 160$ mm and the wave frequency of $f = 81$Hz. The riblet spacing is $s = 1$ mm.

Re_Θ	A = 0.25 mm	A = 0.3 mm	A = 0.375 mm
1200 (M2) (x-y plane)	$f = 81$Hz	$f = 81$Hz	$f = 81$Hz
2080 (M2) (x-y plane)	$f = 81$ Hz	$f = 81$ Hz	$f = 81$ Hz
1200 (M2) (x-y plane)	$T^+ = 110$	$T^+ = 110$	$T^+ = 110$
2080 (M2) (x-y plane)	$T^+ = 380$	$T^+ = 380$	$T^+ = 380$

Table 6.4 Experimental parameter of the spanwise traveling transversal wave motions, 4 amplitudes with a constant wavelength of $\lambda = 160$ mm and the wave frequency of $f = 81$Hz. The riblet spacing is $s = 1$ mm.

Re_Θ	A = 0.26 mm	A = 0.315 mm	A = 0.375 mm	A = 0.5 mm
1200 (M2) (x-y plane)	$f = 54$ Hz	$f = 54$ Hz	$f = 54$ Hz	$f = 54$ Hz
1150 (M1) (x-z plane)	$f = 81$ Hz	$f = 81$ Hz	$f = 81$ Hz	-
1200 (M2) (x-y plane)	$T^+ = 131$	$T^+ = 131$	$T^+ = 131$	$T^+ = 131$
1150 (M1) (x-z plane)	$T^+ = 110$	$T^+ = 110$	$T^+ = 110$	-

6.2.1 Influence of wave amplitude

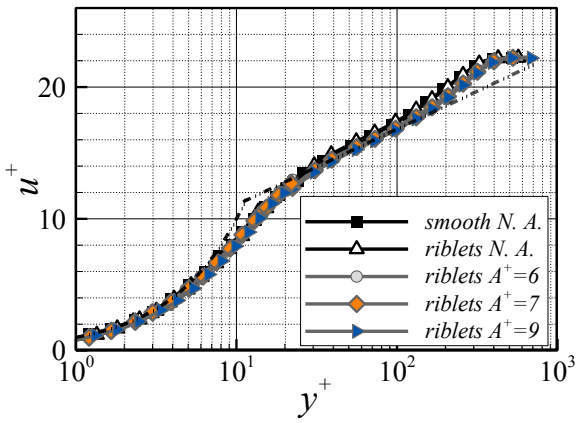

Figure 6.3: Mean streamwise velocity distributions 3 mm downstream of the actuated riblet surface at $Re_\theta = 1200$, $T^+ = 110$, $\lambda^+ = 3862$, and $A^+ = 6$, 7, and 9 compared with the non-actuated riblet and smooth configurations; inner wall units are defined by the nominal friction velocity u_τ above the non-actuated smooth surface; the log law defined by $U^+ = 1/0.41 \ln y^+ + 5.0$ is juxtaposed [100].

Figure 6.3 shows the mean streamwise velocity profiles of the TBL flows for the actuated and non-actuated riblet surface scaled by the nominal friction velocity u_τ of the smooth

configuration at Re_θ= 1200. The results are measured 3 mm downstream of the riblet valley. The riblet surface is actuated at a frequency of 81 Hz. In inner wall units the period T^+ = 110 and the wavelength λ^+ = 3862. The wave amplitudes in inner wall units are A^+ = 6, 7, and 9. The friction velocity u_τ = 0.352 m/s is determined over the smooth surface by a least square linear fitting in the viscous sublayer ($y^+ < 5$). Furthermore, the law of the wall $u^+ = 1/0.41 \ln y^+ + 5$ and the linear wall distribution for a flat plate TBL are shown. To analyze the influence of the riblet structure with and without the actuation on the entire TBL, PIV and µ-PTV data are juxtaposed. The overlap of the FOVs of both measurement techniques covers the region $9 < y^+ < 22$. The match of the curves evidences a convincing agreement of the results of both measurements.

The local velocity profiles of the smooth and riblet configurations show differences stretching from y^+ = 1 to y^+ = 20, where the velocity profiles merge and match the velocity distributions in the log region. The maximum deviation in this region reaches a value of about 10% at y^+ = 5 for A^+ = 9. However, it is hardly noticed in the semi-log plot. In the log region, the results show slightly lower velocity values for all moving riblet configurations compared with the non-actuated smooth and non-actuated riblet configuration. The velocity profiles of both non-actuated configurations match whereas the wave motion reduces the velocity values in the log region by up to 2.7 % for the highest amplitude of A^+ = 9.

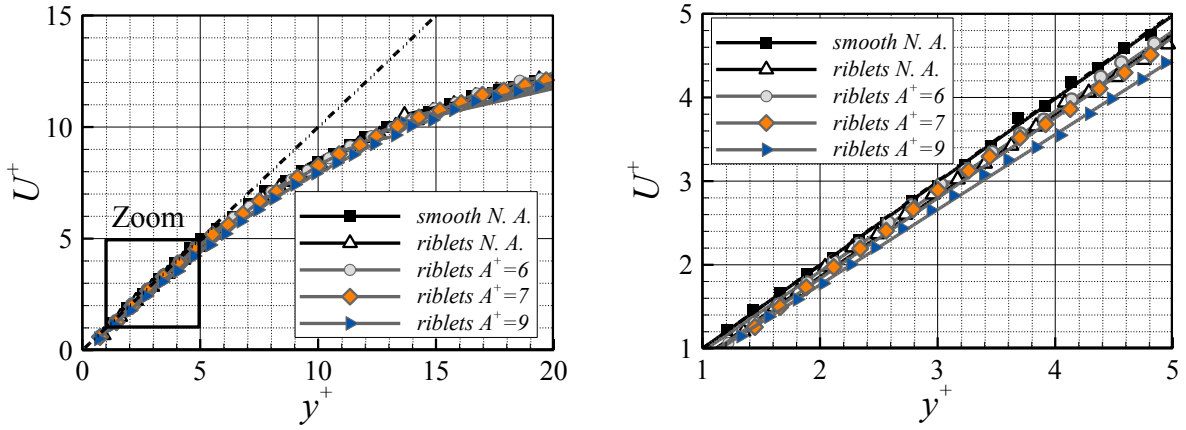

Figure 6.4: Comparison of the mean streamwise velocity in the viscous sublayer for the flat plate flow for the non-actuated and actuated riblet surface at Re_θ = 1200, T^+ = 110, λ^+ = 3862, and A^+ = 6, 7, and 9 with the smooth surface velocity distribution; for the non-actuated riblet surface the data are measured downstream of the riblet valley; inner wall units are defined by the nominal friction velocity u_τ of the non-actuated smooth surface.

To show the impact of the riblet structure and the wave motion with increasing amplitudes on the near-wall flow field, the mean velocity profiles of the A^+ = 6, 7, and 9 configurations are juxtaposed in figure 6.4 in linear scaling. The enlargement of the viscous sublayer ($y^+ < 5$) clearly shows lower gradients for the non-actuated and actuated riblet configurations compared with the non-actuated smooth surface configuration confirming a reduction of the local friction drag. The drag reduction ratios are 4.1%, 5.8%, and 9.4% for A^+ = 6, 7, and 9, respectively.

It has been reported in section 5.1 that the velocity distributions in the viscous sublayer yield a local friction reduction of 4.7 % caused by the semi-circular riblet structure. The additional drag reduction due to the wave motion on the riblet surface for all three actuation amplitudes ranges from -0.6 % for $A^+ = 6$ to the maximum drag reduction of 4.7 % for $A^+ = 9$. That is, the spanwise transversal wave at the lowest amplitude hardly changes the drag reduction effect of the riblet surface, i.e., even a slight increase in friction drag is observed. Whereas at the highest amplitude $A^+ = 9$ the wave motion generates an additional local drag reduction of 4.7% which doubles the drag reduction efficiency of a riblet surface.

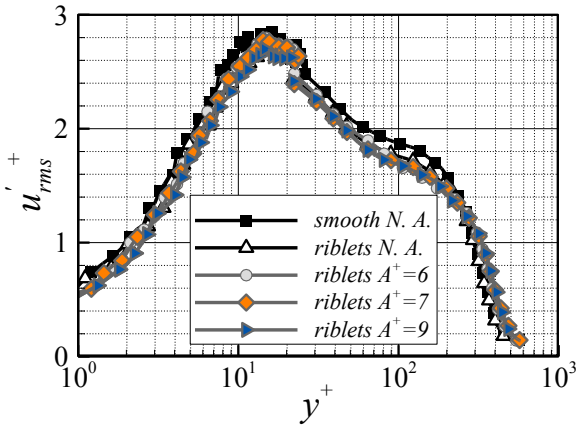

Figure 6.5: Comparison of the root-mean-square value of the streamwise velocity fluctuations scaled by the nominal friction velocity u_τ of the smooth wall downstream of the actuated wall for the non-actuated smooth surface, the non-actuated riblet wall, and the actuated riblet configuration; Re_θ= 1200, A^+ = 6, 7, 9, T^+ = 110, λ^+ = 3862; inner wall units are defined by the nominal friction velocity u_τ of the non-actuated smooth surface.

Figure 6.5 shows a comparison of the distributions of the root-mean-square value of the streamwise velocity fluctuations scaled by the nominal friction velocity u_τ of the non-actuated smooth surface. Again, the velocity fluctuations are composed by juxtaposing the PIV and µ-PTV results. It is noticed that the actuation decreases the peak values of the streamwise velocity fluctuations in the lower part of the TBL ($y^+ \approx 15$) for all actuated and non-actuated riblet configurations compared with smooth surface configuration. This reduction of streamwise fluctuations due to the riblet structure and the actuation is evident in the boundary layer up to $y^+ \leq 250$, where the fluctuation profile of the non-actuated riblet configuration merges with the fluctuation profile of the non-actuated smooth wall. In the outer boundary layer ($250 \leq y^+ \leq 500$) only the fluctuations for the moving riblet configurations are clearly increased which shows that the wave motion of the riblet-structured wall leads to a shift of the mixing region off the wall.

The distributions of the root-mean-square value of the wall-normal velocity fluctuations in figure 6.6 (a) show the same behavior. Note that these wall-normal velocity data are based on the PIV measurement only. Due to the actuation, the wall-normal velocity fluctuations decrease at $y^+ \leq 150$ and increase at $y^+ \geq 150$. This confirms a redistribution of the turbulence content away from the wall into the outer boundary layer. Figure 6.6 (b) shows distributions of the Reynolds shear stress scaled by the nominal friction velocity of the non-actuated

smooth wall $\overline{u'v'}/u_\tau^2$. A clear decrease of the Reynolds shear stress in the inner region of $y^+ \leq$ 150 for both non-actuated and actuated riblet configuration evidences the drag reducing impact. The Reynolds shear stress profiles of the non-actuated riblet and non-actuated smooth configurations match each other in the outer region of $150 < y^+ < 450$ and the Reynolds shear stress increases for the actuated riblet configurations. This agrees with the tendency of the distributions of the wall-normal velocity fluctuations in figure 6.6 (a).

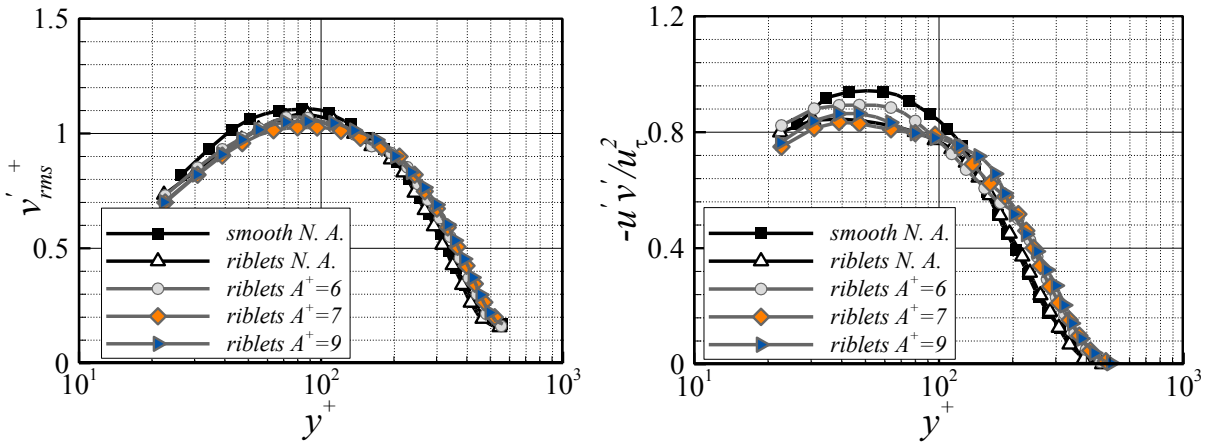

(a) (b)

Figure 6.6: Comparison of the distribution of the root-mean-square value of the wall-normal velocity fluctuation (a) and the Reynolds shear stress $\overline{u'v'}/u_\tau^2$ (b) for the non-actuated smooth surface, the non-actuated riblet wall, and the actuated riblet configurations; Re_θ = 1200, A^+ = 6, 7, 9; the dimensional frequency and wavelength match the Re_θ = 1200 values; inner wall units are defined by the nominal friction velocity u_τ of the non-actuated smooth surface [100].

6.2.2 Influence of Reynolds number

The results for the higher Reynolds numbers of Re_θ = 2080 are shown in figure 6.7. Due to the higher Reynolds number, the amplitude of the transversal wave in inner wall units increases to A^+ = 12, 14, and 16 with a wavelength of λ^+ = 7170 and a dimensionless wave period of T^+ = 380. Since the dimensional riblet spacing stays constant, the dimensionless riblet spacing is drastically increased to s^+ = 45. The velocity distributions of the non-actuated and actuated riblet configurations show nearly no deviation from that of the non-actuated smooth surface. Compared with the lower Reynolds number of Re_θ = 1200, the differences in the velocity distributions at Re_θ = 2080 are less observable in the log region and the viscous sublayer region. For a detailed analysis, the velocity distributions for Re_θ = 2080 in the near-wall region are also shown in linear scaling in figure 6.7 (b). The enlargement of the viscous sublayer is due to a slightly smaller velocity gradient at the highest amplitude A^+ = 17 compared with the smooth surface. For the other actuated riblet configurations the velocity profiles almost coincide with the smooth configuration indicating less or almost no drag reduction. The drag reducing effect of the non-actuated riblet structure reaches a value of DR = 0.7 % which is minute. This drag reduction effect of the s^+ = 45 riblet structure is enhanced by the transversal wave motion at the highest amplitude of A^+ = 17 to DR = 2.7%.

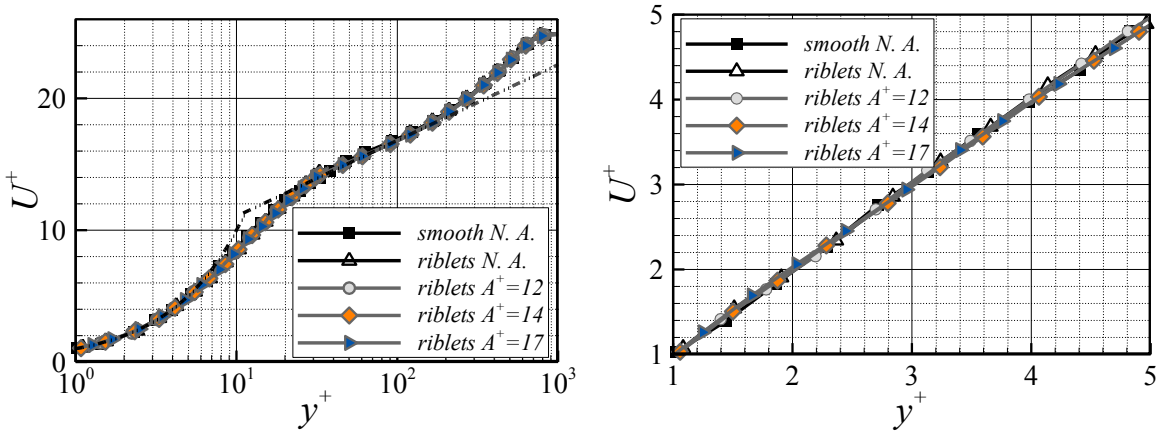

Figure 6.7: Comparison of the mean streamwise velocity distributions downstream of the actuated riblet surface for Re_θ= 2080, T^+ = 380, λ^+ = 7170, A^+ = 12, 14, and 17 with the non-actuated riblet and the smooth configurations; the dimensional amplitude, frequency, and wavelength match the Re_θ= 1200 values; inner wall units are defined by the nominal friction velocity u_τ of the non-actuated smooth surface.

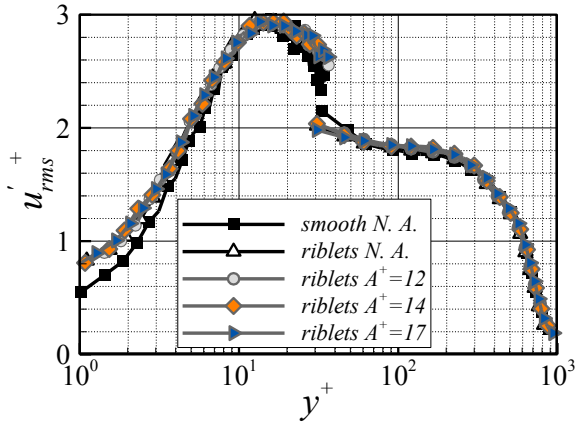

Figure 6.8: Comparison of the root-mean-square value of the streamwise velocity fluctuations scaled by the nominal friction velocity u_τ of the smooth wall downstream of the actuated wall for the non-actuated smooth surface, the non-actuated riblet wall, and the actuated riblet configuration, Re_θ= 2080, A^+ = 12, 14, 17; T^+ = 380, λ^+ = 7170; inner wall units are defined by the nominal friction velocity u_τ of the non-actuated smooth surface.

It has been shown that in the higher drag reducing case of Re_θ = 1200, the streamwise velocity fluctuations are decreased in the near-wall region due to riblets and the wave motion. Figure 6.8 shows a comparison of the streamwise velocity fluctuations scaled by the nominal friction velocity u_τ of the non-actuated smooth wall for Re_θ = 2080. Here, the impact on the streamwise velocity fluctuations is trivial since the momentum input from the wall motion to the flow is smaller compared to the freestream momentum. That is, the normal momentum input generated by the wall movement is not enough to influence the turbulence mixing occuring in the TBL.

The drag reduction ratios by the non-/actuated riblet configurations is plotted in figure 6.9 versus the riblet spacing in inner coordinates and versus the groove-area-based scaling [47], respectively. The maximum local drag reduction obtained at $T^+ = 110$ and $A^+ = 9$ is 9.4% at $Re_\theta = 1200$. It is twice of the drag reduction by the non-actuated riblet surface. That is, the transversal wave motion leads to an increase of the local drag reduction. While at a higher Reynolds number of $Re_\theta = 2080$, i.e., the streamwise velocity is increased, the efficiency of the passive riblet drops. The dimensions of the riblet geometry are no longer in the optimum range of $15 \leq s^+ \leq 25$. This explains why the local drag reduction of the non-actuated riblet surface is just 0.7 %. Interestingly, the actuation has a positive impact on the overall drag reduction in the sense that it increases the local drag reduction to 2.7 % at the highest amplitude. In other words, due to the wave actuation the susceptibility of the riblet geometry to the variation of the freestream velocity, i.e., a higher Reynolds number, is lowered. This is also visualized in figure 6.9, where the drag reduction values for the non-actuated and actuated surface are shown. Since the normal momentum input via the actuated surface at $Re_\theta = 2080$ is smaller compared with the streamwise momentum at $Re_\theta = 1200$, the drag reduction efficiency is decreased yielding 2.7% at $Re_\theta = 2080$ comparing to 9.4 % at $Re_\theta = 1200$.

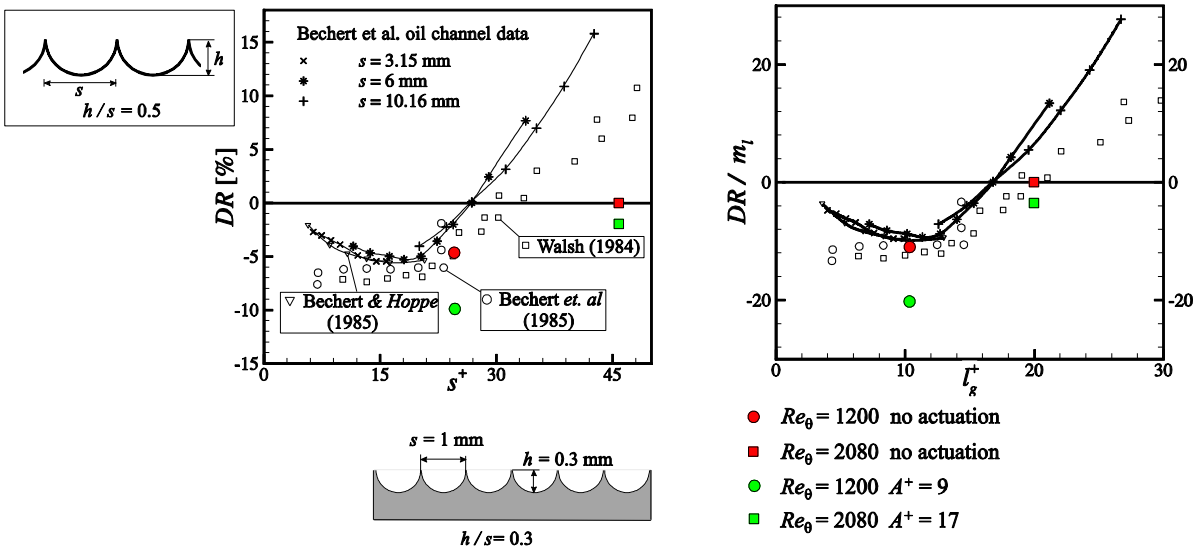

Figure 6.9: Drag reduction DR of a semi-circular riblet structure according to Bechert *et al.* [34] versus riblet width in inner coordinates s^+ (left) and versus groove-area-based scaling (right); the data of this study are given by full symbols.

6.2.3 Influence of wave frequency

According to the analysis in section 6.1, a larger drag reduction occurs at a higher wave frequency. On the one hand, the results have shown that the drag reduction potential increases as the wave period decreases in the current wave parameter range. This indicates that the drag reduction effect is frequency dependent in the smooth surface configuration. On the other hand, the measurements for the riblet configuration at $f = 81$ Hz and $Re_\theta = 1200$ show that the maximum drag reduction of 9.4% occurs at the highest amplitude of $A^+ = 9$. Thus, the question concerning the influence of frequency for the actuated riblet configuration arises

whether this effect still exist. To investigated the impact of the wave frequency on the drag reduction effect of the actuated riblet configuration, PIV and μ-PTV measurements are conducted at M2 at f = 54 Hz.

The drag reduction ratio of the actuated riblet configurations is plotted in figure 6.10 for f = 81 and 54 Hz at Re_θ = 1200. Note that the experiments at f = 54 Hz for the riblet configuration is conducted later. The friction velocity u_τ of the smooth surface is slightly changed comparing with the friction velocity u_τ of f = 81 Hz due to some variations of the environment condition. Thus, the dimensionless riblet spacing is s^+= 22 based on the friction velocity u_τ of the smooth surface. The wavelength is kept constant as λ = 160 mm and four amplitudes A = 0.26, 0.315, 0.375, and 0.5 mm are investigated. In inner units the wavelength is λ^+ = 3433, the amplitudes A^+ = 5.6, 6.8, 8.1, and 10.8 and the wave period T^+ = 131. The non-actuated riblet surface yields local drag reduction ratios of 4.7% and 5.8%. The riblet spacings are s^+ = 24 and 22 located in the drag reduction range when compared with the findings of Bechert *et al.* [34, 45, 149] and Walsh [141]. With the wave motion at f = 54 Hz, the local drag reduction is nearly constant when the amplitude is increased. Drag reduction is increased by around 2% for all these four amplitudes at f = 54 Hz whereas the local drag reduction increases as the wave amplitude rises in the case of f = 81 Hz. As a results, it is concluded that the frequency of 81 Hz, i.e., T^+ = 110 leads to a more significant drag reduction effect in the riblet configuration. This agrees with the analysis of the actuated smooth configuration.

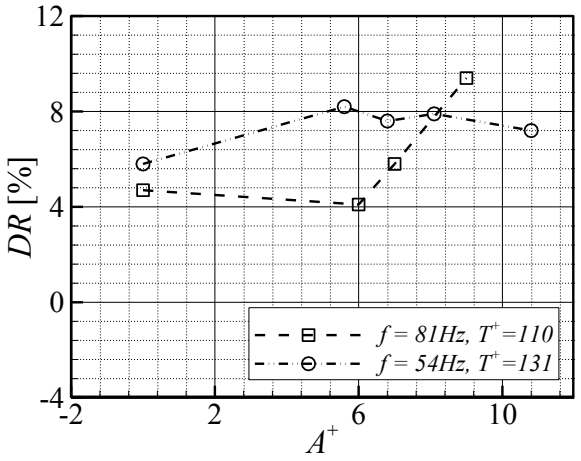

Figure 6.10: Local drag reduction ratio derived from the μ-PTV measurements at M2 as a function of amplitude and frequency; the dimensionless wave frequencies are f = 81 Hz (T^+ = 110, f^+ = 0.009) and 54 Hz (T^+ = 131, f^+ = 0.0076). Wave parameters are summarized in tables 6.3 and 6.4.

In table 6.5, the local drag reduction ratio of the non-actuated and actuated riblet configurations at f = 81 and 54 Hz are summarized. The results of the actuated smooth surface are also listed to quantitatively show the impact of the riblet comparing with the smooth surface. The analysis of the smooth configurations shows a drag reduction of 3.4 % at an actuation amplitude of A^+ = 9. For the riblet configuration at f = 81 Hz, the drag reduction by the riblets alone is 4.7% and it increases to 9.4% with the wave motion. That is, the total drag reduction is not simply the sum due to the nonlinearity in the near-wall turbulent mixing.

Table 6.5: Local drag reduction for the actuated surfaces at Reynolds numbers Re_θ = 1200, two wave frequencies of f = 81 and 54 Hz and different wave amplitudes A^+. The normalized parameters are defined by $T^+ = u_\tau^2/(f\nu)$, $\lambda^+ = \lambda u_\tau/\nu$, and $A^+ = Au_\tau/\nu$, where the nominal friction velocity u_τ is determined for the non-actuated smooth surface.

Re_θ	s^+	h^+	T^+	λ^+	A^+	DR (%)
1200	24	7	110	3862	0	4.7
1200	24	7	110	3862	6	4.1
1200	24	7	110	3862	7	5.8
1200	24	7	110	3862	9	9.4
1200	22	6.4	131	3433	0	5.8
1200	22	6.4	131	3433	5.6	8.2
1200	22	6.4	131	3433	6.8	7.6
1200	22	6.4	131	3433	8.1	7.9
1200	22	6.4	131	3433	10.8	7.2
1200	-	-	110	3862	6	2
1200	-	-	110	3862	7	2.7
1200	-	-	110	3862	9	3.4
1200	-	-	158	3862	6.1	1.0
1200	-	-	158	3862	7.4	1.9
1200	-	-	158	3862	8.9	2.3

6.2.4 Influence of pressure gradient

The impact of an adverse pressure gradient on the drag reduction mechanism of the non-actuated riblet surface has been discussed in section 5.2. On the one hand, the previous results show that an APG has a positive effect on the drag reduction, e.g., the drag reduction of the riblet surface is increased to 7% for Clauser parameter of β = 1.15. On the other hand, the investigation by Roggenkamp [85] on the smooth surface undergoing spanwise traveling wave motion showed that the drag reduction effect was notably weaker in an APG TBL than that in ZPG flows. To understand the influence of an APG on the drag reduction mechanism of the actuated riblet surface, PIV and μ-PTV measurements are conducted at the measurement position M2 in an APG TBL with the a Clauser parameter of β = 1.15. The riblet surface is excited by the actuator system at the same flow condition as that in section 5.2, i.e., U_∞ = 8.75 m/s, Re_θ = 1955, and β = 1.15. The dimensional amplitude, wavelength, and frequency remain unchanged as those in section 6.2.1. With the friction velocity of u_τ = 0.336 m/s determined above the smooth surface in the APG TBL, the riblet spacing s^+ =

21.7 and the dimensionless amplitude, wavelength, and period are A^+ = 5.6, 6.8, and 8.1, λ^+ =3472, and T^+ = 90, respectively.

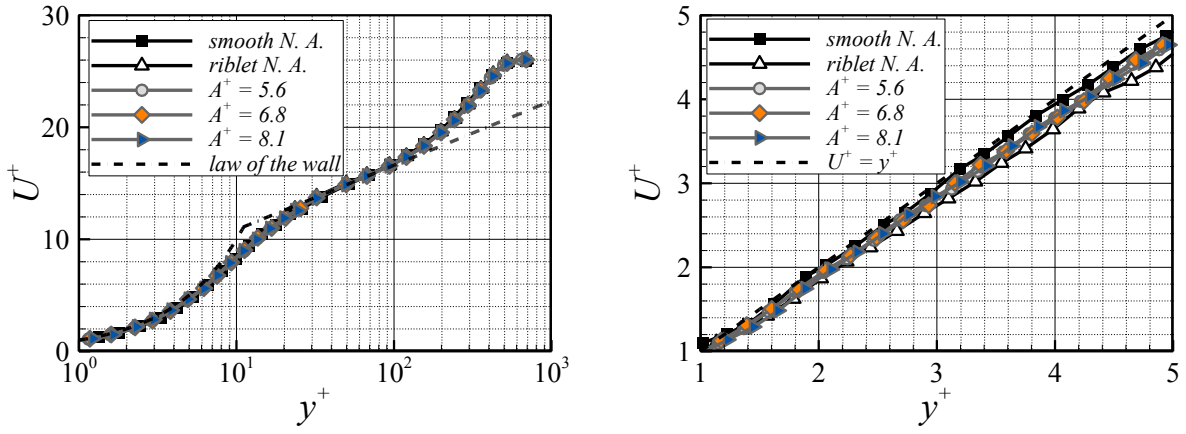

(a) (b)

Figure 6.11: Comparison of the mean streamwise velocity in the viscous sublayer for the flat plate flow for the non-actuated and actuated riblet surface at Re_θ = 1955, β = 1.15, T^+ = 90, λ^+ = 3471, and A^+ = 5.6, 6.8 and 8.1 with the smooth surface velocity distribution; (a), the whole boundary layer measured by the PIV and μ-PTV; (b), the enlargement of the viscous sublayer.

The mean streamwise velocity profiles of the APG flows are shown in figure 6.11 for the non-actuated smooth and the riblet configurations. For comparison, the velocity distribution in the viscous sublayer is enlarged in figure 6.11 (b). With the excitation of the spanwise traveling transversal wave motion, the velocity gradient of the actuated configurations is in between of the non-actuated riblet and smooth cases. The linear fitting of the velocity distribution in the viscous sublayer shows that the drag reduction of the actuated riblet surface is decreased to 3.9%, 4%, and 4.3% for A^+ = 5.6, 6.8, and 8.1. Due to the small deviation of the drag reduction ratio at different amplitude, it seems that there is no strong correlation between the drag reduction and the wave amplitude.

Figure 6.12 shows the comparison of the streamwise velocity fluctuations of the non-actuated smooth surface, the non-actuated and actuated riblet configurations scaled by the nominal friction velocity u_τ of the smooth surface. In the near-wall region, the peak values of the streamwise velocity fluctuations of the riblet configurations are decreased by 4-5% compared with the non-actuated smooth configuration at around y^+ = 15. The occurrence of the second peak of the streamwise velocity fluctuation indicates that the flow is more energetic in the outer region. In comparison to ZPG TBL flows, the outer vertical structures are enhanced while the near-wall streamwise vorticity is weakened in APG. The wall-normal momentum which is induced by the surface wave motion is not sufficient to affect the turbulence regeneration cycle. Thus, in the outer region, the streamwise velocity fluctuations are almost identical for all the non-/actuated riblet configurations.

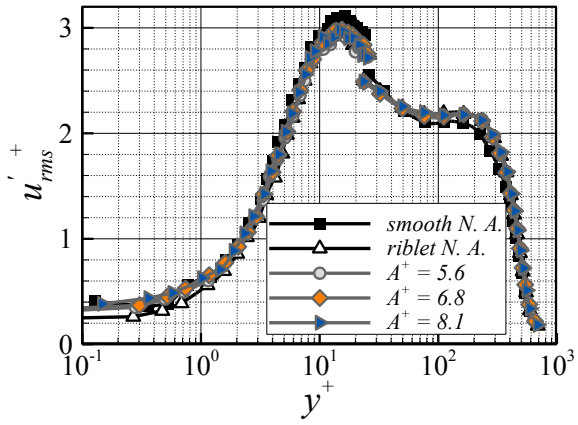

Figure 6.12: Comparison of the root-mean-square value of the streamwise velocity fluctuations scaled by the nominal friction velocity u_τ of the smooth wall downstream of the actuated wall for the non-actuated smooth surface, the non-actuated riblet wall, and the actuated riblet configuration; $Re_\theta = 1955$, $\beta = 1.15$, $T^+ = 90$, $\lambda^+ = 3471$, and $A^+ = 5.6$, 6.8 and 8.1, inner wall units are defined by the nominal friction velocity u_τ of the non-actuated smooth surface.

6.2.5 Analysis of near-wall flow structures

To analyze the near-wall turbulent structures, the flow field above the actuated riblet surface in the *x-z* plane is investigated via phase-locked 2D-3C stereo-PIV. The flow statistics above a complete wavelength is determined by varying the wave phase instead of moving the cameras in spanwise direction. The measurement is conducted above the riblet surface with the wave motion at three wave amplitudes of $A^+ = 6$, 7 and 9 and a wave period of $T^+ = 110$ ($f^+ = 0.009$) whereas the wavelength remains $\lambda = 160$ mm. With this parameter combination, the previous results show a significant drag reduction ratio of maximum 9.4% at $A^+ = 9$.

Above the riblet surface, the laser light sheet tends to produce a strong scattering on the surface due to the tips of riblet structure. These scattering spots located on the tips of the riblet cause inaccurate vectors in the PIV. Thus, the measurement plane of the 2D-3C stereo-PIV is placed at $y = 2$ mm above the actuated riblet surface to reduce the measurement error caused by the surface scattering. The wall distance corresponds to $y^+ = 50$ in inner wall units.

Secondary flow

The impact of the wave motion on the streamwise, spanwise, and wall-normal velocity distributions in the streamwise and spanwise plane are shown in figure 6.13 - 6.15. To make a direct comparison with the non-actuated riblet configuration, the velocity distributions above the non-actuated riblet surface are subtracted from the ones above the actuated riblet surface. The velocity distributions are color-coded with the variations of the three velocity components, $u_A^+ - u_{N.A}^+$, $v_A^+ - v_{N.A}^+$, $w_A^+ - w_{N.A}^+$. Here, N.A. indicates the non-actuated riblet surface. In the streamwise direction, the TBL flow develops slowly and the extension of the measurement area is small. Thus, all the data points possessing a same spanwise position can be used to analyze the flow statistics of the whole flow field. In figure 6.16, the distributions of the three velocity components in figure 6.13 - 6.15 are illustrated by being averaged in the

streamwise direction. Note that the distance between the laser light sheet and the surface are not identical in the spanwise direction due to the transversal surface deformation.

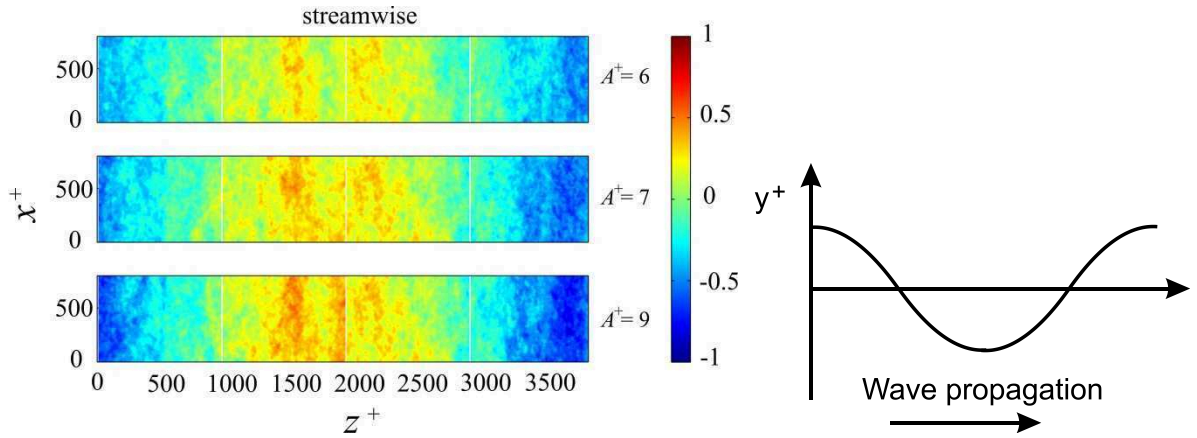

Figure 6.13: Comparison of the phase-averaged streamwise velocity variations u_A^+- $u_{N.A}^+$ above an entire wavelength in the *x*-*z* plane, $y^+ = 50$, $T^+ = 110$, $f^+ = 0.009$.

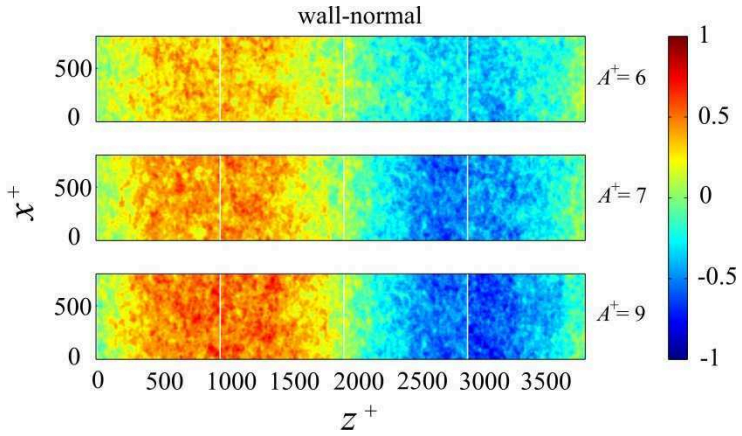

Figure 6.14: Comparison of the phase-averaged wall-normal velocity variations v_A^+- $v_{N.A}^+$ above an entire wavelength in the *x*-*z* plane, $y^+ = 50$, $T^+ = 110$, $f^+ = 0.009$.

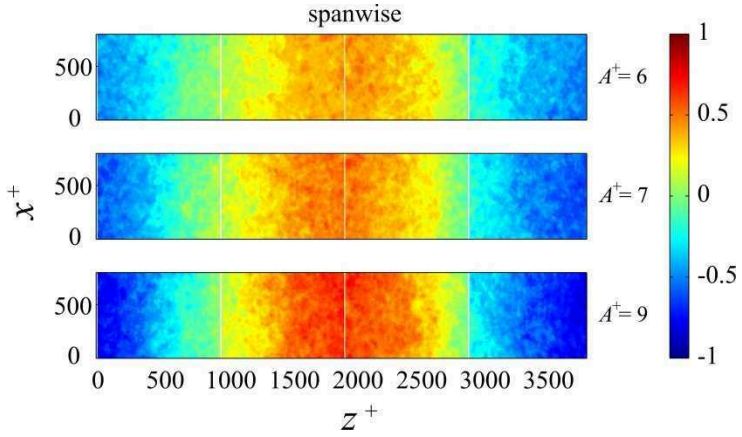

Figure 6.15: Comparison of the phase-averaged spanwise velocity variations w_A^+- $w_{N.A}^+$ above an entire wavelength in the *x*-*z* plane, $y^+ = 50$, $T^+ = 110$, $f^+ = 0.009$.

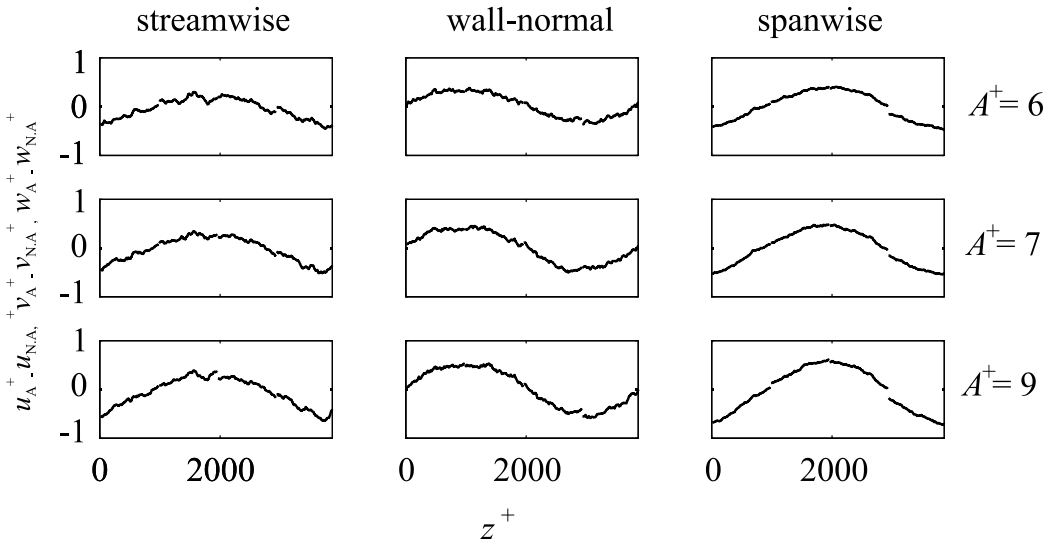

Figure 6.16: Comparison of the phase-averaged velocity distributions above the actuated riblet surface in the *x*-*z* plane, $y^+ = 50$, $T^+ = 110$, $f^+ = 0.009$.

Figure 6.13 shows the variations of the streamwise velocity above the actuated riblet surface at different wave amplitudes. The variations of the phase-locked streamwise velocity possess positive values above the wave trough and negative values above the wave crest. This indicates that a gradient of the streamwise velocity is induced by the surface deformation in the spanwise direction. In figure 6.16, the streamwise velocity distribution is further averaged in the streamwise direction. It is noticed that the phase-locked streamwise velocity variations in the spanwise direction follow a sinusoidal distribution. They possess a phase shift of 0.5 period (0.5*T*) compared with the surface wave motion. This is due to the different distance between the actuated surface and the laser light sheet in the spanwise direction. Above the wave crest, the streamwise variations $(u_A^+ - u_{N.A}^+) / U_\infty^+$ = -1.4%, -1.7%, and -2.1% whereas above the wave trough the variations $(u_A^+ - u_{N.A}^+) / U_\infty^+$ = 1.0%, 1.2%, and 1.4% for A^+ = 6, 7, and 9. The changes in the streamwise velocity are smaller above the wave trough.

In figure 6.14, the out-of-plane velocity, i.e., the wall-normal velocity is measured by stereo-PIV. It is induced by the wave motion and follows the movement of the wall, i.e., a positive velocity exists above the region where the wall moves upwards, and a negative velocity above the region where the wall moves downwards. Above the wave crest and trough, the phase-locked wall-normal velocity reaches zero. The distribution of the wall-normal velocity shows a phase shift of 0.25*T* compared with the displacement of the wall. Furthermore, the intensity of the induced wall-normal velocity increases with the increasing wave amplitude.

The spanwise velocity distributions in figure 6.15 apparently show that a secondary spanwise flow is induced by the wave motion. The spanwise velocity distributions above the wave trough follow the propagation direction of the surface wave whereas it is in the opposite direction above the wave crest. In addition, the maximum spanwise velocity w_{max}^+ increases from 0.4 to 0.7 when the amplitude A^+ increases from 6 to 9, indicating that the intensity of the spanwise secondary flow is enhanced by increasing the actuation amplitude. The findings of the spanwise secondary flow agree well with the results by Tomiyama and Fukagata [82] in channel flows. By performing DNS simulations, they investigated turbulent channel flows

undergoing a spanwise traveling wave-like wall deformation. The induced spanwise flow was considered as the key factor of the drag reduction effect. Above the wave trough, the induced flow prevents OSVs to interact with the wall, i.e., the QSVs are shifted off the wall and the connection between the coherent structures and the wall is weakened due to the enlarged wall distance. This further reduces the random Reynolds shear stress and results in the friction drag reduction.

Two-point correlation

To observe the overall turbulent structure of the flow, two-point spatial correlations of the streamwise fluctuating velocity are analyzed based on the stereo-PIV results. Figure 6.17 shows the two-point spatial correlation functions *Ruu* of the streamwise fluctuating velocities above the non-actuated smooth surface, the non-actuated riblet wall, and the actuated riblet configurations with $A^+ = 9$ at the wave trough and crest. The distributions of *Ruu* above the smooth surface and the riblet configurations show similar elliptical shapes, which is due to the strong anisotropy between the streamwise and spanwise directions.

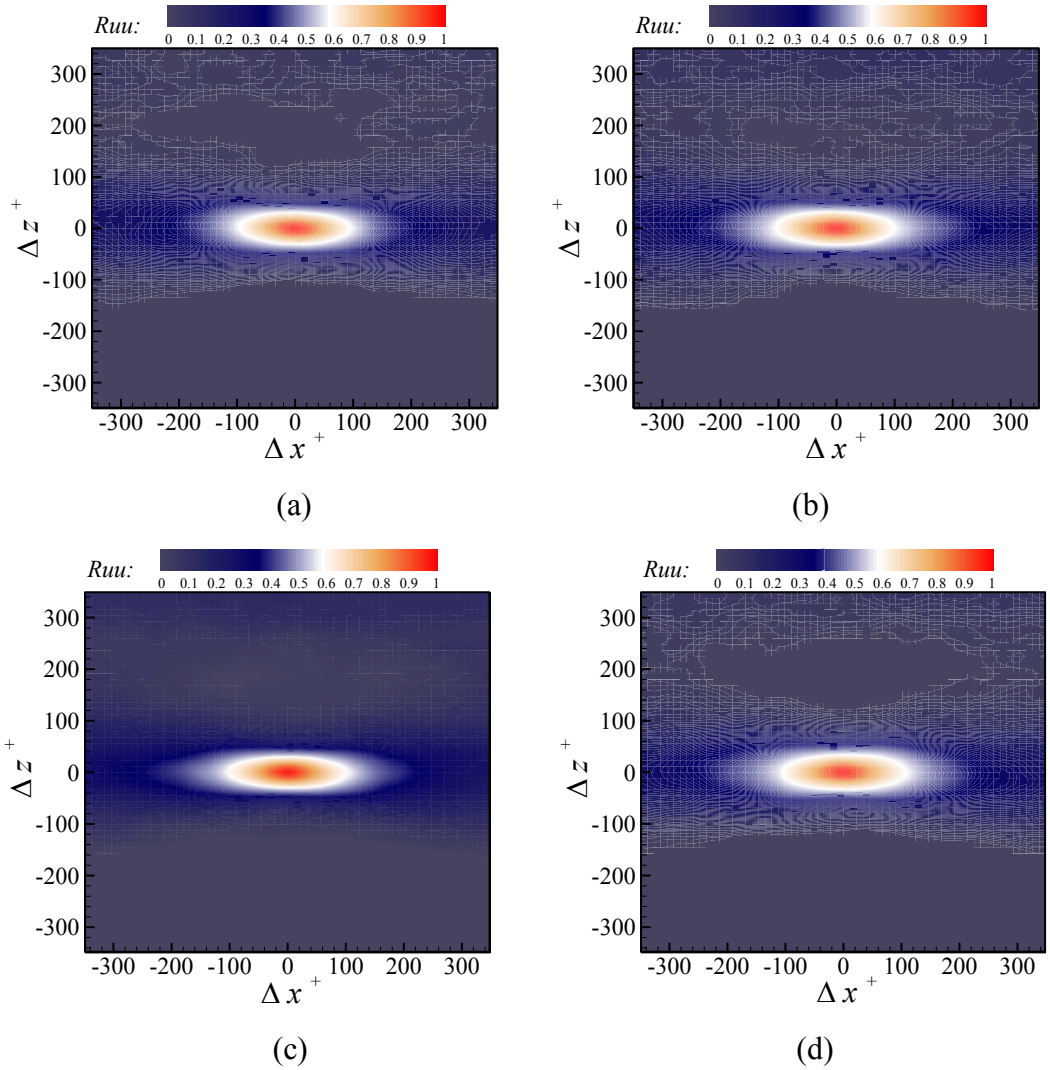

Figure 6.17: Spatial correlation function of the streamwise velocity *Ruu* in the *x*-*z* plane with the wall distance of $y^+ = 50$ at $Re_\theta = 1150$ for the non-actuated smooth surface, the non-

actuated riblet wall, and the actuated riblet configuration with $A^+ = 9$; (a) the smooth wall, (b) non-actuated riblet surface, (c) above the wave crest at $A^+ = 9$, (d) above the wave trough at $A^+ = 9$.

For a closer examination, the quantitative distributions of *Ruu* in the streamwise directions are illustrated in figure 6.18. It is evident that a stronger spatial correlation exists above the non-actuated riblet surface comparing with the smooth one, which suggests that the turbulent structure possesses a larger integral scale in the streamwise. For the actuated riblet configurations, the two-point spatial correlation *Ruu* is decreased above the wave crest in the streamwise direction compared with the non-actuated riblet surface. This is due to the distance between the riblet surface and the laser light sheet is decreased by the upwards displacement above the wave crest. Above the wave trough, the distance between the light sheet and the riblet surface is increased. However, the *Ruu* distribution is nearly unchanged. This suggests that the overall turbulent structure does not follow the movement of the surface and remains at the same wall-normal position.

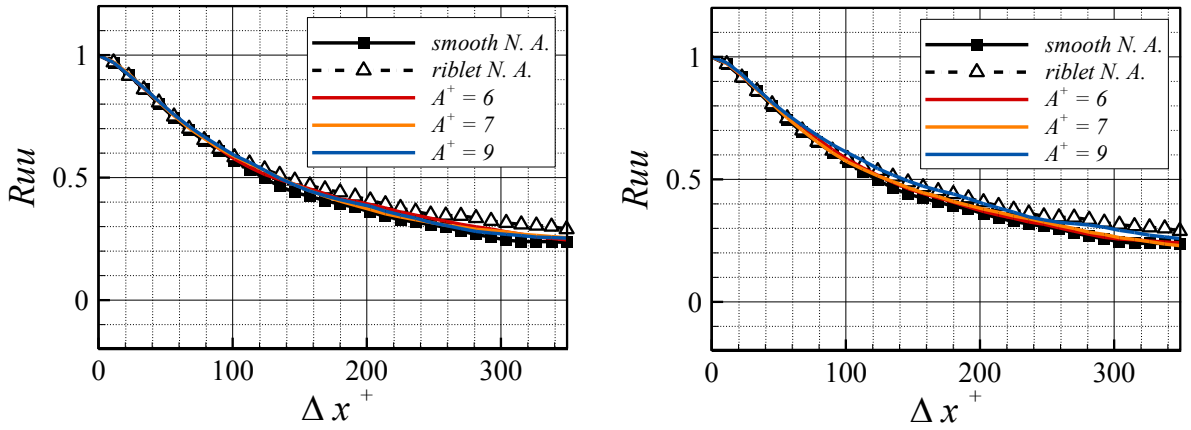

Figure 6.18: Distributions of the spatial correlation function of the streamwise velocity *Ruu* with the wall distance of $y^+ = 50$ at $Re_\theta = 1150$ for the non-actuated smooth surface, the non-actuated riblet wall, and the actuated riblet configuration with $A^+ = 6$, 7, and 9; (a) streamwise, above the wave crest, $\Delta z^+ = 0$, (b) streamwise, above the wave trough, $\Delta z^+ = 0$.

Streaky structures

The streaky structures in TBLs are formed with the quasi-streamwise longitudinal vortices, which are either singularly or in pairs and are brought up by the low-momentum flow from below [66]. Swearingen and Blackwelder [151] reported that the instability of the low-speed streaks in the near-wall region of the turbulent boundary layer is the major source of turbulence productions and played an essential role in the regeneration of the near-wall coherent structures. This indicates that the behavior of the low-speed streaks in the near-wall region of a TBL is closely related to the wall-shear stress.

Figure 6.19 shows a snapshot of the instantaneous velocity field at $y^+ = 50$ in a natural TBL above the smooth surface. The flow comes from the top to the bottom. The FOV of the PIV snapshot covers 700 × 700 wall units. Since the length of the streamwise flow structure is in

the range of 100 - 2000 wall units [150], the extent of the measurement FOV in the streamwise direction is not sufficient for the streak length analysis. Thus, only the influence on the spacing of the low-speed streaks by the riblet structure and the wave motion is discussed.

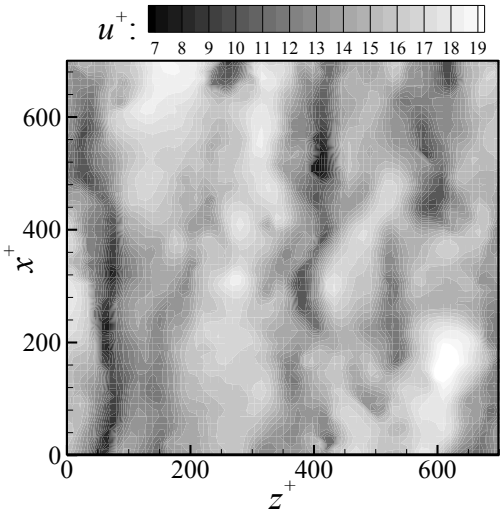

Figure 6.19: Instantaneous distribution of the low-speed streaks in a natural turbulent boundary layer above a smooth surface, $y^+ = 50$ at $Re_\theta = 1150$.

Table 6.6: Averaged low-speed streak spacing in wall units above the wave crest and trough in the x-z plane of $y^+ = 50$ at $Re_\theta = 1150$ for the actuated riblet configurations with $A^+ = 6$, 7, and 9.

Amplitude	crest	trough
$A^+ = 6$	131	137.5
$A^+ = 7$	130.1	138.5
$A^+ = 9$	129.4	137.9

The low-speed streaky flow structure is identified by an in-house Matlab code with 4800 independent flow fields based on the identification procedure in Schoppa and Hussain [27]. For the smooth configuration, the averaged spacing of the low-speed streaks is 135 wall units which agrees with the experimental results of Iuso *et al.* [152]. The averaged spacing of the low-speed streak for the non-actuated riblet configuration decreases to 132.5 wall units compared with the smooth configuration. In Table 6.6, the averaged spacings of the low-speed streaks above the actuated riblet surface are listed. It is noticed that the spacing of the low-speed streaks is decreased above the wave crest for the actuated configurations, i.e., the spacings of the low-speed streaks are decreased by 1.1%, 1.8%, and 2.3% comparing with the non-actuated riblet configuration with the wave amplitudes of $A^+ = 6$, 7, and 9. In contrast, above the wave trough the averaged spacing of the low-speed streaks is increased by around 4%. Above the wave trough with the lowest amplitude of $A^+ = 6$, the distance between the wall and the measurement plane is increased by 6 wall unit leading to an increase of 4% of

the measured steaks spacing. Meanwhile, at higher amplitudes, the spacing of the low-speed streaks above the wave trough is unchanged, indicating the turbulent structures do not completely follow the movement of the riblet surface.

The probability density functions (PDFs) of the low-speed streak spacing above the non-actuated smooth surface, the non-actuated riblet wall, and actuated riblet configurations are depicted in figure 6.20. The non-actuated riblet configuration shows a higher probability density comparing with the smooth one for $\Delta z^+ < 120$. This leads to a reduction of the averaged spacing of the low-speed streaks. With the surface wave motion, the result shows a similar picture above the wave crest comparing with Roggenkamp [85], in which the PDFs are analyzed for the actuated smooth surface configuration. The current results show that the PDFs of the low-speed streaks spacing are skewed to the left side above the wave crest as well as above the trough, i.e., the probability density increases for the low-speed streaks with smaller spacing. Above the wave trough, the probability density increases for the low-speed streaks with large spacing, resulting in an increase of the low-speed streaks spacing.

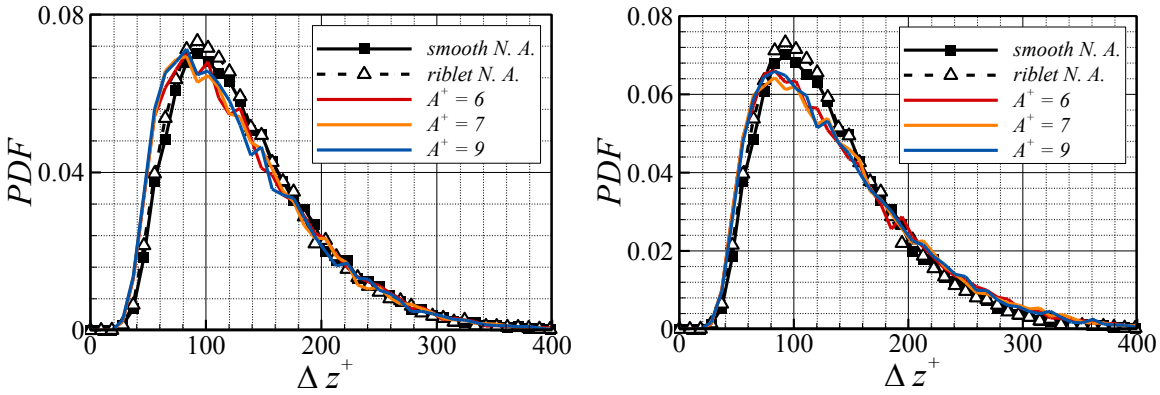

Figure 6.20: Probability density function (PDF) of the low-speed streak spacing in wall units above the non-actuated smooth surface, the non-actuated riblet wall, and the actuated riblet configuration in the *x*-*z* plane of $y^+ = 50$ at $Re_\theta = 1150$; (a) above the wave crest, (b) above the wave trough.

According to Choi *et al.* [54] and Boomsma and Sotiropoulos [145], the riblet induces counter-rotating streamwise vortices near the riblet tip and these vortices possess diameter approximately equal to half of the riblet width. The projections of the counter-rotating vortices are featured in the PDFs of the spacing of the low-speed streaks, which suggests that the global organization of the streaky flow structure is qualitatively affected by the non-actuated riblet structure. In the actuated riblet cases, the distance between the wall and the measurement plane changes depending on the phase of the wave motion, i.e., a smaller distance above the wave crest and a large one above the wave trough. The near-wall turbulence structures that contain counter-rotating vortices with smaller spacing are pushed off the wall by the upwards motion. Thus, the PDFs of the narrow low-speed streaks show a significant increase above the wave crest. During the downwards motion, the probability density of the low-speed streaks with larger spacing is increased due to the enlarged distance between the measurement plane and the wall. However, the narrow low-speed streaks remain

a higher probability density than that of the non-actuated configuration suggesting that the low-speed streaks do not entirely follow the movement of the wall above the wave trough. Thus, low-speed streaks are rearranged away from the wall above the wave trough and the near-wall turbulence productions are shifted off from the wall resulting in a lower friction drag.

6.3 Summary

The combination of passive, riblet structures and active drag reduction means, transversal surface waves, has been investigated in TBL flows. The wave motion is generated by an electromagnetic actuator system that is connected to the lower side of the riblet-structured aluminum surface. PIV and μ-PTV measurements are conducted downstream as well as above the riblet-structured surface to analyze the impact on the wall-shear stress distribution and the flow field of TBLs. A parametric investigation regarding the impact of wave parameters, i.e., wave amplitude, frequency, and the flow conditions, i.e., Reynolds numbers and the adverse pressure gradient is conducted.

The active friction drag reduction by spanwise transversal traveling surface waves with wall deformation is firstly analyzed for a smooth surface configuration. Within the range of the parameters investigated, a drag reduction ratio of 3.4% is achieved for an amplitude of $A^+ = 9$ and a wave period of $T^+ = 110$. The results show that the drag reduction increases with the rising wave amplitude and frequency. Furthermore, with a higher Reynolds number and an APG, no significant drag reduction has been detected.

Detailed measurements have been conducted for the passive riblet configuration undergoing spanwise transversal traveling surface waves. The results show the passive and active means, i.e., the riblet surface and the transversal surface motion, complement each other with respect to drag reduction in ZPG TBL. In comparison with the standard non-actuated smooth surface the non-actuated riblet surface yields a local drag reduction of 4.7 % and the spanwise transversal motion of the riblet surface increases the local drag reduction to 9.4 %. The findings of ribbed wall motion confirm the results for smooth actuated surfaces that the drag reducing impact is improved by increasing the amplitude of the surface motion. This higher drag reduction is due to the normal momentum that is inserted into the flow system such that the turbulent mixing is shifted further off the wall compared with the non-actuated smooth surface. On the other hand, the drag reduction is lowered when the Reynolds number is increased compared with the normal momentum inserted via the wall motion. Nevertheless, also at the higher Reynolds number the combination of the passive and active flow control means lead to a higher local drag reduction DR = 2.7% than the non-actuated riblet surface which possesses a local drag reduction of DR = 0.7 %. In other words, since the drop in drag reduction effect for the non-actuated riblet surface at increasing Reynolds number from DR = 4.7 % at $Re_\theta = 1200$ to DR = 0.7 % at $Re_\theta = 2080$ is due to the link between the turbulent structures and the riblet dimensions, this geometric sensitivity is lowered by the spanwise transversal wall motion. In addition, the results with a different excitation frequencies show a frequency dependence effect. This also agrees with the influence of the wave frequency on the drag reduction effect of the smooth configuration. In the APG TBL, the second peak of

the streamwise velocity fluctuation indicates that the flow is more energetic in the outer region. The induced wall-normal momentum is not enough to influence the regeneration cycles of turbulence structure.

The modification of the flow structures by the wave motion has been investigated by the phase-locked 2D-3C stereo-PIV above the moving surface in the *x-z* plane. It has been found that a spanwise secondary flow is induced by the spanwise transversal traveling surface waves. The secondary flow shields the vortical structure from the wave trough preventing the downwash of high-momentum fluid to the near-wall region. Furthermore, the analysis of the PDFs of the spacing of the low-speed streaks shows that the induced secondary flow rearranges the near-wall turbulence structures above the riblet surface. During the downward motion, the low-speed streaks do not entirely follow the movement of the wall above the wave trough. Thus, the low-speed streaks are rearranged in the outer region and near-wall turbulence productions are shift away from the wall resulting in the drag reduction.

7 Summary and conclusions

This work aims at contributing to the development of friction drag reduction in wall-bounded flows via passive and active flow control means. First, the capability of the riblet structure in reducing the friction drag has been examined experimentally in various flow conditions, e.g., ZPG, APG, and unsteady inflows. Then, the riblets as a passive method in conjunction with the spanwise traveling transversal surface wave motion as the active flow control means have been investigated to seek whether the passive and active control means can complement each other regarding to the drag reduction effect.

The experimental investigation has been conducted in a low-speed wind tunnel via PIV and μ-PTV. The riblet-structured domain is located in the center of a flat plate. With an electromagnetic actuator system beneath the riblet surface, a spanwise traveling surface wave can be generated. The open test section of the wind tunnel has been constructed such that ZPG, APG, and unsteady flows can be analyzed. The friction drag has been determined in the viscous sublayer from the velocity distribution obtained by the high-spatial resolution μ-PTV. The corresponding turbulence characteristics and flow phenomena have been analyzed by 2D-2C and 2D-3C stereo-PIV.

Prior to the investigation of the skin-friciton drag reduction effect in TBLs, high-spatial resolution μ-PTV, standard 2C-2D PIV, and near-wall hot-wire measurements are conducted to examine and quantify the measurement techniques. The streamwise velocity and fluctuations measured by hot-wire are used to examine the accuracy and performance of the μ-PTV and PIV techniques. Furthermore, μ-PTV and PIV are conducted in TBLs with Reynolds numbers Re_θ ranges from 1009 to 4070 to determine the impact of Reynolds number on the distributions of the streamwise turbulence intensity and the wall-shear stress fluctuations. The results show that μ-PTV enables a high-spatial resolution measurement of TBL flows up to 5 μm corresponding to 0.06 ~ 0.26 wall units such that the near-wall velocity gradient which defines the wall-shear stress is determined. The results have shown that the μ-PTV and PIV are able to measure TBL flows as well as the wall-shear stress accurately and efficiently. The μ-PTV measurement technique overcomes the common spatial-resolution issues in standard measurement techniques and provides suitable tools for a quantitative investigation concerning the drag reduction.

In chapter 5, the local drag reduction ratio downstream of the passive riblets has been determined from the velocity gradient in the viscous sublayer. The measurements in ZPG flows show a local drag reduction of 4.7% at $Re_\theta = 1200$ with $s^+ = 24$ and a drag reduction of

0.7% at Re_θ = 2080 with s^+ = 45. These results show a convincing agreement with the friction force measurements in oil channel flows by Bechert *et al.* [34].

For the more realistic flow conditions, i.e., APG and unsteady flows, the local drag reduction has been found to increase to 6 - 7% for a smaller riblet spacing of s^+ = 22. Furthermore, by conducting the measurements above the riblet surface via PIV and μ-PTV at a local Reynolds number of Re_θ = 1150, the protrusion height h_{lp}^+ of the riblet surface is found to be around 19% of the lateral riblet spacing. The quadrant decomposition of the turbulence production indicates that the sweep events are suppressed due to the riblet structure, leading to a reduction of the Reynolds shear stress. A suppression of the ejection and sweep events has been observed in the joint probability density functions. The results have shown a convincing drag reduction effect by the riblet structure.

In chapter 6, the active friction drag reduction effect of spanwise transversal traveling surface waves with wall deformation is analyzed for a smooth surface configuration. Within the range of the parameters investigated, a drag reduction ratio of about 3.4% is achieved for an amplitude of A^+ = 9 and a wave period of T^+ =110. The drag reduction has been found to increase with raising the wave amplitude and the wave frequency. For a higher Reynolds number and an adverse-pressure gradient, no significant drag reduction has been detected. Then, the combination of the passive riblets and the active means has been investigated by imposing spanwise traveling transversal surface waves on the riblet-structured surface. A parametric investigation regarding the impact of wave parameters, i.e., wave amplitude, frequency, and the flow conditions, i.e., Reynolds numbers and the pressure gradient has been conducted.

The results have shown that the passive and active means, i.e., the riblet surface and the transversal surface motion, complement each other with respect to the drag reduction effect in ZPG TBLs. The passive riblet surface has been found to reduce the local friction drag by 4.7% at Re_θ = 1200 whereas the surface wave motion of the riblte surface reduces the local drag reduction by 9.4%. At a higher Reynolds number of Re_θ = 2080, the combination of the passive and active flow control means has demonstrated a higher local drag reduction of 2% than the non-actuated riblet surface, indicating a lower geometric sensitivity due to the spanwise transversal wave motion. With a lower wave frequency of f = 54 Hz, the local drag reduction has been found to be increased by around 2% compared with the non-actuated riblets for all the four wave amplitudes, demonstrating a frequency dependent behavior. In the APG flows, the second peak of the streamwise velocity fluctuation indicates that the TBL flow is more energetic in the outer region. The induced wall-normal momentum is not enough to influence the regeneration cycles of turbulence structure.

The modification of the flow structures by the wave motion has been investigated by the phase-locked 2D-3C stereo-PIV above the moving surface in the *x-z* plane. A spanwise secondary flow is induced by the spanwise transversal traveling surface waves. The maximum spanwise velocity w_{max}^+ increases from 0.4 to 0.7 as the amplitude A^+ increases from 6 to 9, indicating that the intensity of the spanwise secondary flow is enhanced by increasing the actuation amplitude. The secondary flow shields the vortical structure from the wave trough preventing the downwash of high-monument fluid to the near-wall region. The

PDFs of the spacing of the low-speed streaks shows that the induced secondary flow rearranges the near-wall turbulence structures above the riblet surface. The near-wall turbulence structures that contain counter-rotating vortices are pushed away from the wall above the wave crest. During the downward motion, the low-speed streaks do not entirely follow the movement of the wall above the wave trough. Thus, the low-speed streaks are rearranged in the outer region and near-wall turbulence productions are shift away from the wall resulting in the drag reduction.

The presented study is a fundamental research that has addressed different open questions in the field of flow control. For future implementation, the understanding of the flow phenomena behind the friction drag reduction effect needs to be extended and many other new open issues need to be addressed.

In addition, the investigation has been conducted in low Reynolds number and incompressible flows. The impacts of the large turbulent structures in high Reynolds number flows are still unclear. Further research of the actuated riblets in large Reynolds number and high-speed flows still needs to be conducted. On the other hand, the real flows are usually characterized with unsteady gusts. The non-actuated riblets in an unsteady inflow condition have been investigated and this unsteady flow needs to be applied to the actuated riblet configuration. The wave parameters of the more adaptive active flow control means in unsteady gust flows have to be optimized by feedback control strategy. Furthermore, dimensional analysis shows that the excitation frequency of the transversal wave needs to reach up to several thousand Hz in real flight. This is translated to several hundred million excitation cycles in a long-distance flight. Thus, the fatigue property of the actuated riblet surface needs to be considered.

References

[1] G. Schrauf, N. Wood, and B. Gölling. Key aerodynamic technologies for aircraft performance improvement. In *5th Community Aeronautics Days*, Vienna, Austria, 19-21 June, 2006.

[2] M. Gad-el-Hak, Flow control: Passive, active, and reactive flow management. 2007, Cambridge University Press.

[3] G. Karniadakis and K.-S. Choi. Mechanisms on transverse motions in turbulent wall flows. *Annual Review of Fluid Mechanics*, 35: 45-62, 2003.

[4] M. Walsh. Turbulent boundary layer drag reduction using riblets. In *20th Aerospace Sciences Meeting* Orlando, Florida, 11-14 January, 1982.

[5] M. Walsh. Riblets as a viscous drag reduction technique. *AIAA journal*, 21: 485-486, 1983.

[6] M. Walsh. Viscous drag reduction in boundary layers. *Progress in astronautics and aeronautics*: 203–261, 1990.

[7] P.R. Spalart and J.D. McLean. Drag reduction: Enticing turbulence, and then an industry. *Philosophical Transactions of the Royal Society of London A: Mathematical, Physical and Engineering Sciences*, 369: 1556-1569, 2011.

[8] G. Hirt and M. Thome. Rolling of functional metallic surface structures. *CIRP Annals-Manufacturing Technology*, 57: 317-320, 2008.

[9] Y. Du and G.E. Karniadakis. Suppressing wall turbulence by means of a transverse traveling wave. *Science*, 288: 1230-1234, 2000.

[10] D. Gatti and M. Quadrio. Performance losses of drag-reducing spanwise forcing at moderate values of the reynolds number. *Physics of Fluids (1994-present)*, 25: 125109, 2013.

[11] M. Quadrio and P. Ricco. Critical assessment of turbulent drag reduction through spanwise wall oscillations. *Journal of Fluid Mechanics*, 521: 251-271, 2004.

[12] M. Quadrio, P. Ricco, and C. Viotti. Streamwise-travelling waves of spanwise wall velocity for turbulent drag reduction. *Journal of Fluid Mechanics*, 627: 161-178, 2009.

[13] W. Jung, N. Mangiavacchi, and R. Akhavan. Suppression of turbulence in wall-bounded flows by high-frequency spanwise oscillations. *Physics of Fluids A: Fluid Dynamics (1989-1993)*, 4: 1605-1607, 1992.

[14] Y. Du, V. Symeonidis, and G. Karniadakis. Drag reduction in wall-bounded turbulence via a transverse travelling wave. *Journal of Fluid Mechanics*, 457: 1-34, 2002.

[15] D. Roggenkamp *et al.* Experimental investigation of turbulent boundary layers over transversal moving surfaces. *CEAS Aeronautical Journal*, 6: 471-484, 2015.

[16] H. Schlichting and K. Gersten, Boundary-layer theory. 2000, Springer.

[17] S.B. Pope, Turbulent flows. 2000, Cambridge university press.

[18] S. Kline, W. Reynolds, F. Schraub, and P. Runstadler. The structure of turbulent boundary layers. *Journal of Fluid Mechanics*, 30: 741-773, 1967.

[19] E.R. Corino and R.S. Brodkey. A visual investigation of the wall region in turbulent flow. *Journal of Fluid Mechanics*, 37: 1-30, 1969.

[20] R. Adrian, C. Meinhart, and C. Tomkins. Vortex organization in the outer region of the turbulent boundary layer. *Journal of Fluid Mechanics*, 422: 1-54, 2000.

[21] J.M. Wallace. Quadrant analysis in turbulence research: History and evolution. *Annual Review of Fluid Mechanics*, 48: 131-158, 2016.

[22] P. Moin and J. Kim. The structure of the vorticity field in turbulent channel flow. Part 1. Analysis of instantaneous fields and statistical correlations. *Journal of Fluid Mechanics*, 155: 441-464, 1985.

[23] P.R. Spalart. Direct simulation of a turbulent boundary layer up to $Re_\theta = 1410$. *Journal of Fluid Mechanics*, 187: 61-98, 1988.

[24] J.M. Hamilton, J. Kim, and F. Waleffe. Regeneration mechanisms of near-wall turbulence structures. *Journal of Fluid Mechanics*, 287: 317-348, 1995.

[25] S.K. Robinson. Coherent motions in the turbulent boundary layer. *Annual Review of Fluid Mechanics*, 23: 601-639, 1991.

[26] J. Zhou, R.J. Adrian, and S. Balachandar. Autogeneration of near wall vortical structures in channel flow. *Physics of Fluids (1994-present)*, 8: 288-290, 1996.

[27] W. Schoppa and F. Hussain. Coherent structure generation in near-wall turbulence. *Journal of Fluid Mechanics*, 453: 57-108, 2002.

[28] B. Balakumar and R. Adrian. Large-and very-large-scale motions in channel and boundary-layer flows. *Philosophical Transactions of the Royal Society of London A: Mathematical, Physical and Engineering Sciences*, 365: 665-681, 2007.

[29] N. Hutchins and I. Marusic. Evidence of very long meandering features in the logarithmic region of turbulent boundary layers. *Journal of Fluid Mechanics*, 579: 1-28, 2007.

[30] M. Guala, S. Hommema, and R. Adrian. Large-scale and very-large-scale motions in turbulent pipe flow. *Journal of Fluid Mechanics*, 554: 521-542, 2006.

[31] K. Kim and R. Adrian. Very large-scale motion in the outer layer. *Physics of Fluids (1994-present)*, 11: 417-422, 1999.

[32] A.J. Smits, B.J. McKeon, and I. Marusic. High reynolds number wall turbulence. *Annual Review of Fluid Mechanics*, 43: 353-375, 2011.

[33] A. Baron and M. Quadrio. Some preliminary results on the influence of riblets on the structure of a turbulent boundary layer. *International Journal of Heat and Fluid Flow*, 14: 223-230, 1993.

[34] D. Bechert *et al.* Experiments on drag-reducing surfaces and their optimization with an adjustable geometry. *Journal of Fluid Mechanics*, 338: 59-87, 1997.

[35] K.-S. Choi. Near-wall structure of a turbulent boundary layer with riblets. *Journal of Fluid Mechanics*, 208: 417-458, 1989.

[36] R. García-Mayoral and J. Jiménez. Drag reduction by riblets. *Philosophical Transactions of the Royal Society of London A: Mathematical, Physical and Engineering Sciences*, 369: 1412-1427, 2011.

[37] F. Nieuwstadt *et al.* The reduction of skin friction by riblets under the influence of an adverse pressure gradient. *Experiments in Fluids*, 15: 17-26, 1993.

[38] R. Akhavan, W. Jung, and N. Mangiavacchi, "*Turbulence control in wall-bounded flows by spanwise oscillations"*, in *Advances in turbulence iv*. 1993, Springer. p. 299-303.

[39] K.-S. Choi, J.-R. DeBisschop, and B.R. Clayton. Turbulent boundary-layer control by means of spanwise-wall oscillation. *AIAA journal*, 36: 1157-1163, 1998.

[40] K.-S. Choi, T. Jukes, and R. Whalley. Turbulent boundary-layer control with plasma actuators. *Philosophical Transactions of the Royal Society of London A: Mathematical, Physical and Engineering Sciences*, 369: 1443-1458, 2011.

[41] S.W. Klumpp, Variation of friction drag in wall-bounded flows. 2010, Shaker.

[42] S.R. Koh *et al.* Dependence of turbulent wall-shear stress on the amplitude of spanwise transversal surface waves. *Computers & Fluids*, 119: 261-275, 2015.

[43] P. Ricco and S. Hahn. Turbulent drag reduction through rotating discs. *Journal of Fluid Mechanics*, 722: 267-290, 2013.

[44] D. Bechert *et al.* Biological surfaces and their technological application-laboratory and flight experiments on drag reduction and separation control. *AIAA paper*, 97-1960: 1960, 1997.

[45] D. Bechert, G. Hoppe, and W. Reif. On the drag reduction of the shark skin. *AIAA paper*, 85: 0546, 1985.

[46] B. Dean and B. Bhushan. Shark-skin surfaces for fluid-drag reduction in turbulent flow: A review. *Philosophical Transactions of the Royal Society A: Mathematical, Physical and Engineering Sciences*, 368: 4775-4806, 2010.

[47] R. Garcia-Mayoral and J. Jimenez. Hydrodynamic stability and breakdown of the viscous regime over riblets. *Journal of Fluid Mechanics*, 678: 317-347, 2011.

[48] S. Klumpp, T. Guldner, M. Meinke, and W. Schröder. Riblets in a turbulent adverse-pressure gradient boundary layer. In *5th Flow Control Conference*, Chicago, Illinois, 28 June - 01 July, 2010.

[49] S.-J. Lee and Y.-S. Choi. Decrement of spanwise vortices by a drag-reducing riblet surface. *Journal of Turbulence*, 9: 2008.

[50] S.R. Park and J.M. Wallace. Flow alteration and drag reduction by riblets in a turbulent boundary layer. *AIAA journal*, 32: 31-38, 1994.

[51] J. Eitner. *Pro-environmental and economically airborne*. 2011 [cited 2017 26 May]; Available from: https://www.ibp.fraunhofer.de/en/Press/Press_releases/Aerodays2011.html.

[52] M.J. Walsh and L. Weinstein. Drag and heat transfer on surfaces with small longitudinal fins. In *11th Fluid and PlasmaDynamics Conference*, Seattle, Washington, 10-12 July, 1978.

[53] D. Bechert and M. Bartenwerfer. The viscous flow on surfaces with longitudinal ribs. *Journal of Fluid Mechanics*, 206: 105-129, 1989.

[54] H. Choi, P. Moin, and J. Kim. Direct numerical simulation of turbulent flow over riblets. *Journal of Fluid Mechanics*, 255: 503-539, 1993.

[55] D. Goldstein, R. Handler, and L. Sirovich. Direct numerical simulation of turbulent flow over a modeled riblet covered surface. *Journal of Fluid Mechanics*, 302: 333-376, 1995.

[56] Y. Suzuki and N. Kasagi. Turbulent drag reduction mechanism above a riblet surface. *AIAA journal*, 32: 1781-1790, 1994.

[57] A.J. Greidanus, R. Delfos, S. Tokgoz, and J. Westerweel. Turbulent taylor–couette flow over riblets: Drag reduction and the effect of bulk fluid rotation. *Experiments in Fluids*, 56: 1-13, 2015.

[58] S.-J. Lee and S.-H. Lee. Flow field analysis of a turbulent boundary layer over a riblet surface. *Experiments in Fluids*, 30: 153-166, 2001.

[59] D. Goldstein and T.-C. Tuan. Secondary flow induced by riblets. *Journal of Fluid Mechanics*, 363: 115-151, 1998.

[60] C. Fang, T. Yan-Ping, and C. Mao-Zhang. An experimental investigation of loss reduction with riblets on cascade blade surfaces and isolated airfoils. In *ASME 1990 International Gas Turbine and Aeroengine Congress and Exposition*, Bussels, Belgium, 11-14 June, 1990.

[61] M. Boese and L. Fottner. Effects of riblets on the loss behavior of a highly loaded compressor cascade. In *ASME Turbo Expo 2002: Power for Land, Sea, and Air*, Amsterdam, The Netherlands, 3-6 June, 2002.

[62] J. Szodruch. Viscous drag reduction on transport aircraft. In *29th Aerospace Sciences Meeting*, Reno, Nevada, 7-10 January, 1991.

[63] S.-J. Lee and Y.-G. Jang. Control of flow around a NACA 0012 airfoil with a micro-riblet film. *Journal of Fluids and Structures*, 20: 659-672, 2005.

[64] A. Sareen, R.W. Deters, S.P. Henry, and M.S. Selig. Drag reduction using riblet film applied to airfoils for wind turbines. *Journal of Solar Energy Engineering*, 136: 021007, 2014.

[65] F. Laadhari, L. Skandaji, and R. Morel. Turbulence reduction in a boundary layer by a local spanwise oscillating surface. *Physics of Fluids (1994-present)*, 6: 3218-3220, 1994.

[66] K.-S. Choi. Near-wall structure of turbulent boundary layer with spanwise-wall oscillation. *Physics of Fluids (1994-present)*, 14: 2530-2542, 2002.

[67] G.M. Di Cicca, G. Iuso, P.G. Spazzini, and M. Onorato. Particle image velocimetry investigation of a turbulent boundary layer manipulated by spanwise wall oscillations. *Journal of Fluid Mechanics*, 467: 41-56, 2002.

[68] K. Gouder, M. Potter, and J.F. Morrison. Turbulent friction drag reduction using electroactive polymer and electromagnetically driven surfaces. *Experiments in Fluids*, 54: 1-12, 2013.

[69] D. Gatti, A. Güttler, B. Frohnapfel, and C. Tropea. Experimental assessment of spanwise-oscillating dielectric electroactive surfaces for turbulent drag reduction in an air channel flow. *Experiments in Fluids*, 56: 1-15, 2015.

[70] A. Baron and M. Quadrio. Turbulent drag reduction by spanwise wall oscillations. *Applied Scientific Research*, 55: 311-326, 1995.

[71] E. Touber and M.A. Leschziner. Near-wall streak modification by spanwise oscillatory wall motion and drag-reduction mechanisms. *Journal of Fluid Mechanics*, 693: 150-200, 2012.

[72] L. Huang, B. Fan, and G. Dong. Turbulent drag reduction via a transverse wave traveling along streamwise direction induced by lorentz force. *Physics of Fluids (1994-present)*, 22: 015103, 2010.

[73] R.D. Whalley and K.-S. Choi. Turbulent boundary-layer control with plasma spanwise travelling waves. *Experiments in Fluids*, 55: 1-16, 2014.

[74] E. Hurst, Q. Yang, and Y.M. Chung. The effect of reynolds number on turbulent drag reduction by streamwise travelling waves. *Journal of Fluid Mechanics*, 759: 28-55, 2014.

[75] D.J. Wise and P. Ricco. Turbulent drag reduction through oscillating discs. *Journal of Fluid Mechanics*, 746: 536-564, 2014.

[76] K. Fukagata, K. Iwamoto, and N. Kasagi. Contribution of reynolds stress distribution to the skin friction in wall-bounded flows. *Physics of Fluids (1994-present)*, 14: 73-76, 2002.

[77] L. Shen, X. Zhang, D.K. Yue, and M.S. Triantafyllou. Turbulent flow over a flexible wall undergoing a streamwise travelling wave motion. *Journal of Fluid Mechanics*, 484: 197-221, 2003.

[78] R. Nakanishi, H. Mamori, and K. Fukagata. Relaminarization of turbulent channel flow using traveling wave-like wall deformation. *International Journal of Heat and Fluid Flow*, 35: 152-159, 2012.

[79] M. Itoh, S. Tamano, K. Yokota, and S. Taniguchi. Drag reduction in a turbulent boundary layer on a flexible sheet undergoing a spanwise traveling wave motion. *Journal of Turbulence*, 7: 1-17, 2006.

[80] S. Tamano and M. Itoh. Drag reduction in turbulent boundary layers by spanwise traveling waves with wall deformation. *Journal of Turbulence*, 13: 1-26, 2012.

[81] S. Klumpp, M. Meinke, and W. Schröder. Drag reduction by spanwise transversal surface waves. *Journal of Turbulence*, 11: 1-13, 2010.

[82] N. Tomiyama and K. Fukagata. Direct numerical simulation of drag reduction in a turbulent channel flow using spanwise traveling wave-like wall deformation. *Physics of Fluids (1994-present)*, 25: 105-115, 2013.

[83] P.S. Meysonnat, S.R. Koh, B. Roidl, and W. Schröder. Impact of transversal traveling surface waves in a non-zero pressure gradient turbulent boundary layer flow. *Applied Mathematics and Computation*, 272: 498-507, 2016.

[84] J. Pöplau *et al.* The influence of process parameters on forming of riblets during riblet rolling. *Key Engineering materials*, 5: 1-18, 2014.

[85] D. Roggenkamp, Turbulent friction drag reduction by spanwise traveling surface waves. 2017, RWTH Aachen, PhD thesis.

[86] C. Kähler, U. Scholz, and J. Ortmanns. Wall-shear-stress and near-wall turbulence measurements up to single pixel resolution by means of long-distance micro-piv. *Experiments in Fluids*, 41: 327-341, 2006.

[87] M. Raffel, C.E. Willert, and J. Kompenhans, Particle image velocimetry: A practical guide. 2007, Springer Science & Business Media.

[88] N. Hutchins and K.-S. Choi. Accurate measurements of local skin friction coefficient using hot-wire anemometry. *Progress in Aerospace Sciences*, 38: 421-446, 2002.

[89] P. Ligrani and P. Bradshaw. Spatial resolution and measurement of turbulence in the viscous sublayer using subminiature hot-wire probes. *Experiments in Fluids*, 5: 407-417, 1987.

[90] N. Hutchins, T.B. Nickels, I. Marusic, and M. Chong. Hot-wire spatial resolution issues in wall-bounded turbulence. *Journal of Fluid Mechanics*, 635: 103-136, 2009.

[91] H.H. Bruun, *Hot-wire anemometry-principles and signal analysis*. 1995, IOPscience.

[92] B. Nottebrock, Advancements in the measurement regime of the micro-pillar shear-stress sensor. 2015, Shaker.

[93] J. Westerweel and F. Scarano. Universal outlier detection for piv data. *Experiments in Fluids*, 39: 1096-1100, 2005.

[94] J.C. Crocker and D.G. Grier. Methods of digital video microscopy for colloidal studies. *Journal of Colloid and Interface Science*, 179: 298-310, 1996.

[95] N. Malik, T. Dracos, and D. Papantoniou. Particle tracking velocimetry in three-dimensional flows. *Experiments in Fluids*, 15: 279-294, 1993.

[96] P.H. Alfredsson and R. Örlü. The diagnostic plot - a litmus test for wall bounded turbulence data. *European Journal of Mechanics-B/Fluids*, 29: 403-406, 2010.

[97] A. Melling. Tracer particles and seeding for particle image velocimetry. *Measurement Science and Technology*, 8: 1406, 1997.

[98] L. Benedict and R. Gould. Towards better uncertainty estimates for turbulence statistics. *Experiments in Fluids*, 22: 129-136, 1996.

[99] F. Durst, J. Jovanovic, and J. Sender. Lda measurements in the near-wall region of a turbulent pipe flow. *Journal of Fluid Mechanics*, 295: 305-335, 1995.

[100] W. Li *et al.* Turbulent drag reduction by spanwise traveling ribbed surface waves. *European Journal of Mechanics-B/Fluids*, 53: 101-112, 2015.

[101] A. Cenedese, G. Romano, and R. Antonia. A comment on the "linear" law of the wall for fully developed turbulent channel flow. *Experiments in Fluids*, 25: 165-170, 1998.

[102] G.E. Box, W.G. Hunter, and J.S. Hunter, Statistics for experimenters: An introduction to design, data analysis, and model building. Vol. 1. 1978, JSTOR.

[103] K. Fukagata and N. Kasagi. Drag reduction in turbulent pipe flow with feedback control applied partially to wall. *International Journal of Heat and Fluid Flow*, 24: 480-490, 2003.

[104] I. Marusic *et al.* Wall-bounded turbulent flows at high reynolds numbers: Recent advances and key issues. *Physics of Fluids (1994-present)*, 22: 065103, 2010.

[105] R. Örlü and P.H. Alfredsson. On spatial resolution issues related to time-averaged quantities using hot-wire anemometry. *Experiments in Fluids*, 49: 101-110, 2010.

[106] S.C. Bailey *et al.* Turbulence measurements using a nanoscale thermal anemometry probe. *Journal of Fluid Mechanics*, 663: 160-179, 2010.

[107] Y. Fan *et al.* Nanoscale sensing devices for turbulence measurements. *Experiments in Fluids*, 56: 1-13, 2015.

[108] M. Hultmark, M. Vallikivi, S. Bailey, and A. Smits. Turbulent pipe flow at extreme reynolds numbers. *Physical Review Letters*, 108: 094501, 2012.

[109] C.J. Kähler, S. Scharnowski, and C. Cierpka. On the resolution limit of digital particle image velocimetry. *Experiments in Fluids*, 52: 1629-1639, 2012.

[110] C. de Silva *et al.* High spatial range velocity measurements in a high reynolds number turbulent boundary layer. *Physics of Fluids (1994-present)*, 26: 025117, 2014.

[111] T. Knopp *et al.* Investigation of scaling laws in a turbulent boundary layer flow with adverse pressure gradient using piv. *Journal of Turbulence*, 16: 250-272, 2015.

[112] C.J. Kähler, S. Scharnowski, and C. Cierpka. On the uncertainty of digital PIV and PTV near walls. *Experiments in Fluids*, 52: 1641-1656, 2012.

[113] C. Tropea. Laser doppler anemometry: Recent developments and future challenges. *Measurement Science and technology*, 6: 605, 1995.

[114] C. Cierpka, S. Scharnowski, and C.J. Kähler. Parallax correction for precise near-wall flow investigations using particle imaging. *Applied Optics*, 52: 2923-2931, 2013.

[115] P. Drude, The theory of optics. 1925, Courier Corporation.

[116] P. Schlatter and R. Örlü. Assessment of direct numerical simulation data of turbulent boundary layers. *Journal of Fluid Mechanics*, 659: 116-126, 2010.

[117] J. Jimenez, S. Hoyas, M.P. Simens, and Y. Mizuno. Turbulent boundary layers and channels at moderate reynolds numbers. *Journal of Fluid Mechanics*, 657: 335-360, 2010.

[118] A. Kendall and M. Koochesfahani. A method for estimating wall friction in turbulent wall-bounded flows. *Experiments in Fluids*, 44: 773-780, 2008.

[119] K.A. Chauhan, P.A. Monkewitz, and H.M. Nagib. Criteria for assessing experiments in zero pressure gradient boundary layers. *Fluid Dynamics Research*, 41: 021404, 2009.

[120] R. Örlü and P. Schlatter. Comparison of experiments and simulations for zero pressure gradient turbulent boundary layers at moderate reynolds numbers. *Experiments in Fluids*, 54: 1-21, 2013.

[121] H. Fernholz and P. Finleyt. The incompressible zero-pressure-gradient turbulent boundary layer: An assessment of the data. *Progress in Aerospace Sciences*, 32: 245-311, 1996.

[122] C. Atkinson, N.A. Buchmann, O. Amili, and J. Soria. On the appropriate filtering of piv measurements of turbulent shear flows. *Experiments in Fluids*, 55: 1-15, 2014.

[123] D.B. De Graaff and J.K. Eaton. Reynolds-number scaling of the flat-plate turbulent boundary layer. *Journal of Fluid Mechanics*, 422: 319-346, 2000.

[124] I. Marusic and G.J. Kunkel. Streamwise turbulence intensity formulation for flat-plate boundary layers. *Physics of Fluids (1994-present)*, 15: 2461-2464, 2003.

[125] A.A. Townsend, The structure of turbulent shear flow. 1980, Cambridge university press.

[126] P.H. Alfredsson, A.V. Johansson, J.H. Haritonidis, and H. Eckelmann. The fluctuating wall-shear stress and the velocity field in the viscous sublayer. *Physics of Fluids (1958-1988)*, 31: 1026-1033, 1988.

[127] S. Große and W. Schröder. Dynamic wall-shear stress measurements in turbulent pipe flow using the micro-pillar sensor mps 3. *International Journal of Heat and Fluid Flow*, 29: 830-840, 2008.

[128] J.M. Österlund, Experimental studies of zero pressure-gradient turbulent boundary layer flow. 1999, Royal Institute of Technology, Department of Mechanics.

[129] J. Komminaho and M. Skote. Reynolds stress budgets in couette and boundary layer flows. *Flow, Turbulence and Combustion*, 68: 167-192, 2002.

[130] X. Wu and P. Moin. Transitional and turbulent boundary layer with heat transfer. *Physics of Fluids (1994-present)*, 22: 085105, 2010.

[131] K. Iwamoto, Y. Suzuki, and N. Kasagi. Reynolds number effect on wall turbulence: Toward effective feedback control. *International Journal of Heat and Fluid Flow*, 23: 678-689, 2002.

[132] Z. Hu, C.L. Morfey, and N.D. Sandham. Wall pressure and shear stress spectra from direct simulations of channel flow. *AIAA journal*, 44: 1541-1549, 2006.

[133] H. Abe, H. Kawamura, and Y. Matsuo. Surface heat-flux fluctuations in a turbulent channel flow up to $Re_\tau = 1020$ with $Pr = 0.025$ and 0.71. *International Journal of Heat and Fluid Flow*, 25: 404-419, 2004.

[134] J.C. Del Alamo, J. Jiménez, P. Zandonade, and R.D. Moser. Scaling of the energy spectra of turbulent channels. *Journal of Fluid Mechanics*, 500: 135-144, 2004.

[135] R. Örlü and P. Schlatter. On the fluctuating wall-shear stress in zero pressure-gradient turbulent boundary layer flows. *Physics of Fluids (1994-present)*, 23: 021704, 2011.

[136] A.J. Smits. Canonical wall-bounded flows: How do they differ? *Journal of Fluid Mechanics*, 774: 1-4, 2015.

[137] M. Fischer, J. Jovanović, and F. Durst. Reynolds number effects in the near-wall region of turbulent channel flows. *Physics of Fluids (1994-present)*, 13: 1755-1767, 2001.

[138] L. Keirsbulck, L. Labraga, and M. Gad-el-Hak. Statistical properties of wall shear stress fluctuations in turbulent channel flows. *International Journal of Heat and Fluid Flow*, 37: 1-8, 2012.

[139] K.J. Colella and W.L. Keith. Measurements and scaling of wall shear stress fluctuations. *Experiments in Fluids*, 34: 253-260, 2003.

[140] R. Örlü and P.H. Alfredsson. Comment on the scaling of the near-wall streamwise variance peak in turbulent pipe flows. *Experiments in Fluids*, 54: 1-5, 2013.

[141] M. Walsh and A. Lindemann *Optimization and application of riblets for turbulent drag reduction*. AlAA 22nd Aerospace Sciences Meeting 1984.

[142] H. Bai *et al.* Active control of a turbulent boundary layer based on local surface perturbation. *Journal of Fluid Mechanics*, 750: 316-354, 2014.

[143] M. Sasamori, H. Mamori, K. Iwamoto, and A. Murata. Experimental study on drag-reduction effect due to sinusoidal riblets in turbulent channel flow. *Experiments in Fluids*, 55: 1-14, 2014.

[144] J. Debisschop and F. Nieuwstadt. Turbulent boundary layer in an adverse pressure gradient-effectiveness of riblets. *AIAA journal*, 34: 932-937, 1996.

[145] A. Boomsma and F. Sotiropoulos. Riblet drag reduction in mild adverse pressure gradients: A numerical investigation. *International Journal of Heat and Fluid Flow*, 56: 251-260, 2015.

[146] A. Bobke, R. Vinuesa, R. Örlü, and P. Schlatter, *Large-eddy simulations of adverse pressure gradient turbulent boundary layers*, in *Journal of Physics: Conference Series*. 2016, IOP Publishing. p. 012012.

[147] L. Djenidi and R. Antonia. Laser doppler anemometer measurements of turbulent boundary layer over a riblet surface. *AIAA journal*, 34: 1007-1012, 1996.

[148] S. Klumpp, M. Meinke, and W. Schröder. Friction drag variation via spanwise transversal surface waves. *Flow, Turbulence and Combustion*, 87: 33-53, 2011.

[149] D. Bechert and G. Hoppe. Oberflächen zur widerstandsverminderung. In *3rd European Turbulent Drag Reduction Working Party*, ONERA Chatillon, Paris, 29-30 September, 1988.

[150] B.J. Cantwell. Organized motion in turbulent flow. *Annual Review of Fluid Mechanics*, 13: 457-515, 1981.

[151] J.D. Swearingen and R.F. Blackwelder. The growth and breakdown of streamwise vortices in the presence of a wall. *Journal of Fluid Mechanics*, 182: 255-290, 1987.

[152] G. Iuso *et al.* Velocity streak structure modifications induced by flow manipulation. *Physics of Fluids (1994-present)*, 15: 2602-2612, 2003.

Author-related prepublished manuscripts and supervised student theses

The following scientific works have been published in peer-reviewed journals, books, and conference proceedings.

- W. Li, D. Roggenkamp, W. Jessen, and M. Klaas. PIV and μ-PTV investigations of turbulent flow over a flexible wall undergoing traveling surface wave motions. In *18th International Symposia on Applications of Laser Techniques to Fluid Mechanics*, Lisbon, Portugal, 4 -7 July, 2016.
- W. Li, D. Roggenkamp, W. Jessen, M. Klaas, and W. Schröder, "*Turbulent drag reduction by spanwise traveling ribbed surface waves"*, in *Fluid-structure-sound interactions and control*, Y. Zhou, et al., Editors. 2016, Springer Berlin Heidelberg. p. 363-368.
- W. Li, D. Roggenkamp, W. Jessen, M. Klaas, and W. Schröder. Reynolds number effects on the fluctuating velocity distribution in wall-bounded shear layers. *Measurement Science and Technology*, 28: 015302, 2016.
- P.S. Meysonnat, D. Roggenkamp, W. Li, B. Roidl, and W. Schröder. Experimental and numerical investigation of transversal traveling surface waves for drag reduction. *European Journal of Mechanics-B/Fluids*, 55: 313-323, 2016.
- D. Roggenkamp, W. Jessen, W. Li, M. Klaas, and W. Schröder. Experimental investigation of turbulent boundary layers over transversal moving surfaces. *CEAS Aeronautical Journal*, 6: 471-484, 2015.
- D. Roggenkamp, W. Li, P. Meysonnat, M. Klaas, and W. Schröder, Experimental analysis of turbulent friction drag reduction due to spanwise transversal surface waves, in *9th Symposium on Turbulence and Shear Flow Phenomena*. 2015: Melbourne, Australia.
- W. Li, W. Jessen, D. Roggenkamp, M. Klaas, W. Silex, M. Schiek, and W. Schröder. Turbulent drag reduction by spanwise traveling ribbed surface waves. *European Journal of Mechanics-B/Fluids*, 53: 101-112, 2015.
- W. Jessen, W. Li, D. Roggenkamp, M. Klaas, & W. Schröder. Experimental analysis of the near-wall flow structure over moving surfaces. In *4th International Conference on Experimental Fluid Mechanics* Beijing, China, 12-15 August, 2015.

The following student theses have been supervised by the author.

- T. Hecken. Parametric investigation of active friction drag reduction by spanwise traveling surface wave with wall-deformation. Master thesis, RWTH Aachen University, 2016.
- Z. Lei. Turbulent drag reduction by spanwise traveling wave motion on riblet surface. Bachelor thesis, RWTH Aachen University, 2014.
- T. Pan. and C. vor der Bruck. Long-distance Micro-PIV/PTV wind tunnel investigations on smooth and riblet surfaces. Project thesis, RWTH Aachen University, 2014.